WASHINGTON UNIVERSITY

Department of Physics

Dissertation Committee:

James G. Miller, Chairman
Dan I. Bolef
Peter A. Fedders

ULTRASONIC COUPLING TO OPTICALLY GENERATED CHARGE CARRIERS IN CdS: PHYSICAL PHENOMENA AND APPLICATIONS

by

Joseph Saul Heyman

A dissertation presented to the
Graduate School of Arts and Sciences
of Washington University
in partial fulfillment of the
requirements for the degree of
Doctor of Philosophy

May 1975
Saint Louis, Missouri

TABLE OF CONTENTS

LIST OF FIGURES

PREFACE

Much of the research described in this dissertation has been performed at NASA-Langley Research Center, Hampton, Virginia. However, many of the experimental techniques and theoretical ideas are the result of close collaboration with J. G. Miller. Some of the material in Section I-2 has been published (J. Appl. Phys., 44, #8, Aug. 1973, pp. 3398) by Joseph S. Heyman and J. G. Miller under the title "Verification of Sensitivity Enhancement Factors for CW Ultrasonic Resonators" and by Joseph S. Heyman (NASA TN D-7417, December 1973) under the title "Ultrasonic Signal Enhancement by Resonator Techniques". Part of the work in Section II-2 was published (Rev. Sci. Instr., 45, #3, March 1974, pp. 358) by Mark S. Conradi, J. G. Miller, and Joseph S. Heyman under the title "A Transmission Oscillator Ultrasonic Spectrometer". Some of the initial concept development of the device in Section II-2 was done with Mark Conradi.

Part of the research described in Sections II-3 and II-4 was done with Dennis Dietz and F. Dale Stone. Much of the medical information and expertise necessary for the development of the microemboli monitor was provided by Richard M. Clark who also supervised the operation during which the data of figures 25 and 26 was obtained. Part of Section II-4 has been presented (Proceedings of the Annual Conference on Engineering in Medicine and Biology, Philadelphia, Pennsylvania Oct. 1974) by Dennis Dietz, Joseph S. Heyman, J. G. Miller, and Richard E. Clark in a talk titled "Continuous Wave Ultrasonic Microemboli Monitor for Use in Extracorporeal Perfusion." In addition, a patent has been filed for the work of Sections II-3 and II-4.

Some of the material in Section III-2 has been published (NASA-Tech Brief, B73-10420, December 1973) by Joseph S. Heyman and J. G. Miller

titled "Ultrasonic Calibration Device" and a patent has been filed covering the same work. Some of the research in Section III-3 was developed with D. E. Yuhas and the medical advice of A. N. Weiss and has been presented (Proc. of the Am. Institute of Ultrasound in Medicine, Seattle, Wash., Oct. 1974) by J. G. Miller, Joseph S. Heyman, D. E. Yuhas, and Alan N. Weiss.

ACKNOWLEDGEMENTS

There are many people who affect ones professional career and provide the necessary environment for the development of the individual and his research. I have worked under the supervision of two scientists who have had a profound impact on my research programs and scientific development.

Professor J. G. Miller at Washington University introduced me to ultrasonics and has collaborated with me, frequently suggesting research topics which have always proven valuable. He has my highest respect; his inventive research and brilliant teaching have provided me with a background rich in inspiration and motivation. I am looking forward to continued association with him as a colleague and a personal and warmly regarded friend.

Herbert D. Hendricks, head of the Instrument Techniques Section at NASA-Langley Research Center, has been my supervisor and close friend since 1964 when I came to NASA as a Co-op student. His encouragement and research experience have played an important role in the successful outcome of my experimental research. Equally important, he has maintained a stable and stimulating environment, supported our programs, and helped us keep abreast of complementary research.

My association with Professor D. I. Bolef has been very rewarding and I appreciate his support of my research endeavors.

I am indebted to Professor Peter A. Fedders for his assistance in my graduate education and research. We have shared many stimulating and congenial conversations.

The author is indebted to Dr. Richard E. Clark for his advice and active participation on the TOUS medical experiment and to Dr. Alan N. Weiss for his advice on the medical applications of the power detector.

F. Dale Stone deserves credit for his inventive and dedicated help with both electronics and many measurements described in this dissertation.

I am grateful to Dr. James A. Hutchby for much information on CdS and for becoming involved in my ultrasonic research efforts.

I thank physicist William E. Miller for his assistance with several computer programs and for many enlightening conversations.

I thank Dr. D. E. Yuhas for his insight on the anomalous sign reversal of the acoustoelectric voltage and am looking forward to working closely with him in the future.

I am grateful to Dr. K. V. Vaidyanathan for our many conversations on solid state plasmas.

The author is grateful to his co-workers both at NASA and at Washington University. In particular, I wish to thank Dennis Dietz, Mark Conradi, Virgil Stubblefield, Rosa Webster, Tommy Steele, Allen Milton, John Burgess, Tucker Clark, Jack Tarrh, and George Walker for their advice and help.

L. Lilie played an important role in the design and construction of the first Sampled Continuous Wave Spectrometer.

A special word of thanks is due to my dear wife, Berna. She shared the sacrifices, joys, and hard work of this research and never lost her perspective nor failed in her encouragement. We are one. And to the newest member of our family, Laura Dawn, special thanks for introducing me to a happy and new experience in acoustics.

I thank my parents who gave me every opportunity to think, to expand my horizons, and to enjoy and love life.

"WE HAVE TO CURE OURSELVES OF THE ITCH FOR ABSOLUTE KNOWLEDGE AND POWER. WE HAVE TO CLOSE THE DISTANCE BETWEEN THE PUSHBUTTON ORDER AND THE HUMAN ACT. WE HAVE TO TOUCH PEOPLE."

Jacob Bronowski, Ascent of Man

LIST OF SYMBOLS

$a/2$	resonator length
A	Re $\tilde{A}$
A	cross sectional area
$\tilde{A}$	complex particle velocity
A_1	inphase component of the particle velocity (absorption term)
A_2	quadrature component of the particle velocity (dispersion term)
AE	acoustoelectric
c	elastic constant
C	capacitance
Co	constant
CW	continuous wave
e	charge on the electron
E_{AE}	acoustoelectric field
f	fraction of mobile space charge
$F = \frac{\omega_c}{\omega}$	conductivity frequency divided by ultrasonic frequency
G	electronic gain
I	photon flux
j	integer
k	Boltzman constant
k	wave number
k_m	wave number at the peak of the m^{th} mechanical resonance

K	electromechanical coupling coefficient
L_D	diffusion length
m	integer
n	electron density
n_o	effective surface electron density
p	electronic loss
PE	pulse echo
R	resistance
SCW	sampled continuous wave
t	time
T	temperature
v	acoustic phase velocity
V	voltage
V_{AE}	acoustoelectric voltage
x	position along resonator
α	acoustic attenuation per unit length
$\bar{\alpha}$	effective optical absorption coefficient
ϵ	dielectric permittivity
$\kappa = e^2/c\epsilon$	coupling strength parameter
λ	wave length
μ	mobility
ρ	density
σ	conductivity
τ	time
τ	lifetime

Φ	acoustic flux
ω	ultrasonic frequency
ω_m	frequency at the peak of the m^{th} mechanical resonance
ω_c	conductivity frequency
ω_D	diffusion frequency

I-1. INTRODUCTION

A study of ultrasonic waves in materials must of necessity include phonon interactions with solids. In certain materials, the strongest interaction affecting ultrasonic properties is lattice-charge carrier coupling. This, for example, occurs in piezoelectric non-insulating solids such as CdS and GaAs. Since these materials are also photoconductive, the magnitude of the lattice-charge carrier interaction may be modulated with external illumination. This provides an effective means of varying the ultrasonic properties of a sample. In this study, these effects have been utilized to investigate both phonon-charge carrier interactions as well as ultrasonic resonators themselves. Results of this research have verified sensitivity enhancement factors predicted by one-dimensional resonator theory and have led to the development of several sensitive ultrasonic experimental techniques, one of which was selected by Industrial Research magazine for the IR-100 award[1] in 1974. In addition, measurements are reported of an anomalous sign reversal of the acoustoelectric voltage in a CdS resonator. Applications of CdS as an ultrasonic power detector are described.

In section I-2 ultrasonic resonators are analyzed using one-dimensional theory[2]. The results of this analysis predict conditions for optimum sensitivity to changes in ultrasonic parameters. Sensitivity enhancement factors[3,4] are derived and related to changes in absorption and dispersion for several experimental techniques. A technique is described for obtaining pure absorption or dispersion signals by using zero crossings in the sensitivity enhancement factors. The one-dimensional resonator theory can be verified[4] by producing pure absorption or pure dispersion physical changes in the resonator. These

conditions are nearly achieved with the ultrasonic calibrator (section III-2) which makes use of phonon-charge carrier interactions in CdS. Experimental measurements obtained with the calibrator verify sensitivity enhancement factors predicted by theory.

Section II describes in detail two new experimental instruments. One of these is a refinement of a spectrometer described in reference 5, while the other is a new system co-developed by this author and other researchers at Washington University[6]. The first instrument is a hybrid of pulse echo (PE) and continuous wave (CW) systems and is called a sampled CW spectrometer (SCW). It not only combines attributes of PE and CW spectrometers, but also eliminates some of their disadvantages. By its very nature, PE systems cannot produce monochromatic phonons and therefore measurements using such a system can lead to inhomogeneous broadening[7] of narrow resonant phenomena. CW spectrometers suffer from "crosstalk" (electrical leakage around the sample) which can be serious for thin lossy materials. The SCW, however, produces as monochromatic a phonon as desired and without "crosstalk" interference.

The second instrument described is a transmission oscillator ultrasonic spectrometer (TOUS)[6]. This device exhibits high sensitivity because it utilizes maximum sensitivity enhancement as well as marginal oscillation. In spite of its high sensitivity, the TOUS system is relatively simple, compact, and inexpensive. A concept is examined using this technique for the detection of particulate and gaseous aglomerations present in flowing fluids. This concept led to the development of an ultrasonic device which monitors microemboli in blood during heart-lung bypass surgery. One component of this system is an amplitude regulator[8] used to maintain stable marginal oscillations.

Tests of the regulator demonstrate that it also can be used with RF signal generators to reduce spurious amplitude modulations by two orders of magnitude (to less than 10 microvolts AM).

Section III presents details of the phonon-charge carrier interaction in CdS with applications for ultrasonic calibration and ultrasonic power (nonphase sensitive) detection. In III-1 the theory of Hutson and White[9] is examined and relationships between absorption, dispersion, and conductivity presented. The effects of sensitizing centers is discussed and shown to produce an effective error in absorption and dispersion measurements.

Section III-2 describes an ultrasonic calibration device[10,11] based on photogenerated charge carriers in piezoelectric crystals. Unlike previous calibration techniques, this system utilizes real physical changes in absorption and dispersion. Therefore, this system produces not only typical insertion loss calibrations but also time domain decay and frequency domain linewidth calibrations. In addition, the sensitivity enhancement factors and background attenuation are adjustable to those of the sample being calibrated. Thus, an ultrasonic experiment can be evaluated and optimized for a particular sample. Figures are presented of absorption changes down to 10^{-5} cm.$^{-1}$ and phase velocity changes to less than 10^{-1} cm/sec.

In section III-3, the thoery of the acoustoelectric effect is applied to a CdS resonator. The effect photogenerated carriers play in the acoustoelectric voltage is examined. Non-uniform charge-carrier density is experimentally shown to produce an anomolous sign reversal in an acoustoelectric resonator. A model is developed using non-uniform charge carrier density to optimize the amplitude of the acoustoelectric

voltage. Since the generated voltage is proportional to the incident acoustic flux, the effect can be used as a sensor of ultrasonic power[12]. This concept is examined for parallel and nonparallel quartz samples using PE and SCW spectrometers. The benefit of non-phase sensitive detectors such as this power detector is the absence of phase modulation effects. Experimental data demonstrate superior signal characteristics for the power detector when compared to conventional piezoelectric systems.

I-2. RESONATOR THEORY, SENSITIVITY ENHANCEMENT FACTORS

I-2-1. BACKGROUND

The field of Ultrasonics is taking a prominent role in applied technology measurements. What were state of the art material physics laboratory measurements of thirty years ago can be carried out today with off the shelf equipment. For example, the pulse echo techniques developed in the 1940's[13,14,15] for the study of solids and organic liquids are in use today in rural communities for measuring fat on livestock[16]. The rapid introduction of sophisticated laboratory equipment into the public sector has led to the development of many types of ultrasonic measurement systems.

One class of Ultrasonic measurements is the Continuous Wave (CW) resonant technique[17,18,19]. This method has the distinction of being able to generate monochromatic phonons. In addition, both in-phase (absorption) and quadrative (dispersion) measurements are possible at the same time[20]. One critical part of the CW resonant technique is the resonator itself. Specifically, resonators are widely used to improve the sensitivity of measurements to changes in absorption and dispersion in acoustic material.[2] This is especially true in the field of solid state physics where changes in parameters of one part in 10^6 can be significant. These changes are due to many different interactions in a specimen, for example nuclear acoustic resonance (NAR), Alpher-Rubin effect, phonon coupling to the charge carrier system, acoustic paramagnetic resonance (APR), and many others.[17] Even though there exists a variety of physical interactions producing these changes,

the role of the resonator in each case is the same. It is therefore important to have a theoretical understanding and experimental verification on the role resonators play in ultrasonic signal enhancement.

In this section are presented experimental curves of the sensitivity enhancement line shapes. These line shapes are predicted from a theoretical analysis following a model described in references 2, 3, 4 and 17. The experimental procedure used in obtaining these measurements involves ultrasonic coupling to light-induced charge carriers in CdS (See section III). In this procedure, light incident on the CdS changes its conductivity which leads to changes in the material's ultrasonic properties. These effects are used to separate the absorptive and dispersive effects.

I-2-2. THEORY FOR ONE-DIMENSIONAL ULTRASONIC RESONATOR

The model used for this study is an idealized one-dimensional acoustic resonator, shown in figure 1. This model consists of a cylindrical resonator of length $a/2$ with flat and parallel faces, one of which ($x = 0$) is driven by a $\cos\omega t$ disturbance. This disturbance results in a damped traveling acoustic wave $\exp(-\alpha x)\cos(\omega t - kx)$ propagating in the material. In this equation, the characteristic attenuation per unit length is expressed by α, and the acoustic wave number is expressed by $k = \frac{2\pi}{\lambda} = \frac{\omega}{v}$ where v is the acoustic phase velocity.

By assuming perfect reflection at the $x = 0$ and $x = a/2$ face, the particle velocity amplitude A at $x = 0$ is found by the superposition of all the partial waves present at $x = 0$. As shown in reference 2, the complex particle velocity amplitude at $x = 0$ is:

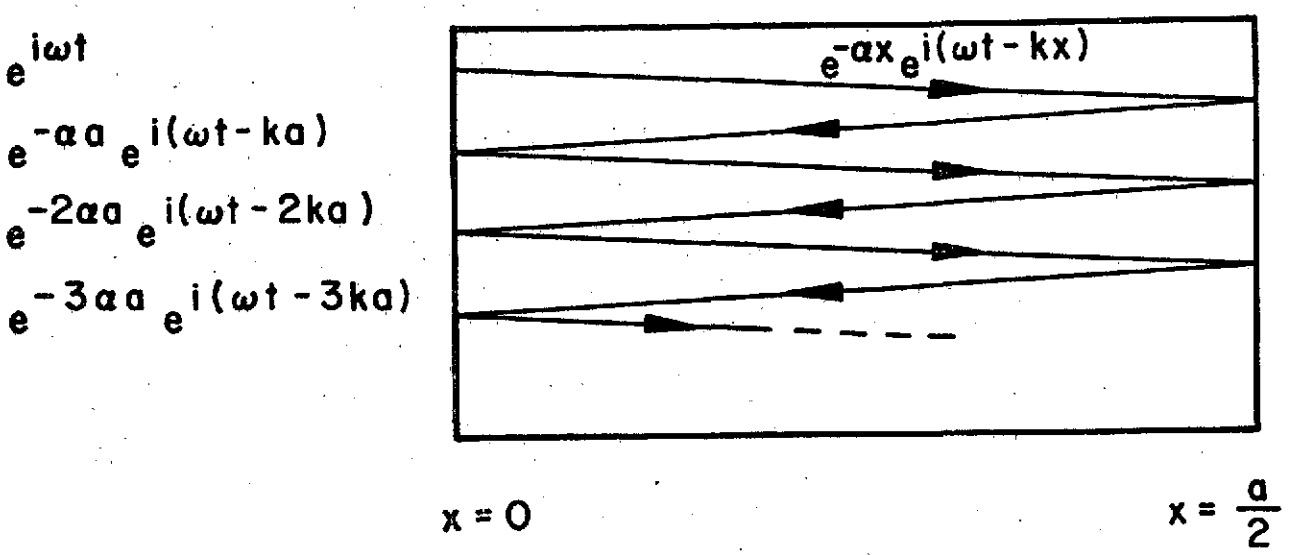

Figure 1) One dimensional isolated resonator showing several partial waves. Waves are actually parallel to resonator axis but displayed non-parallel for clarity.

$$\tilde{A}(\tau) = e^{i\omega\tau}\{1 + [\exp(-\alpha a + ika)] + \exp[-2(\alpha a + ika)] + \ldots\} \quad \text{(I-1)}$$

For the case of $\alpha > 0$ this becomes

$$\tilde{A}(\tau) = e^{i\omega\tau}/[1 - \exp - (\alpha a + ika)] \quad \text{(I-2)}$$

and the real particle velocity becomes:

$$A = \mathrm{Re}\,\tilde{A} = A_1 \cos\omega\tau + A_2 \sin\omega\tau \quad \text{(I-3)}$$

where

$$A_1 = (e^{\alpha a} - \cos ka)/2(\cosh\alpha a - \cos ka) \quad \text{(I-4)}$$

$$A_2 = \mathrm{Sin}ka/2(\cosh\alpha a - \cos ka) \quad \text{(I-5)}$$

Note in equation I-3 that the A_1 term is in-phase with the $\cos\omega\tau$ driving disturbance while the A_2 term is advanced by 90°. The particle velocity response as a function of frequency consists of a series of standing wave or mechanical resonances whose frequencies correspond to the condition that the length $1/2a$ of the crystal be equal to an integral number of half-wavelengths of ultrasound.

Using a phase-sensitive or bridge-type detection scheme one may measure either the in-phase (A_1) or out-of-phase (A_2) component of the response. With linear diode detection, one obtains only the magnitude $|A| = (A_1^2 + A_2^2)^{1/2}$, where

$$|A| = \exp(\alpha a/2)/\sqrt{2}(\cosh\alpha a - \cos ka)^{1/2} \quad \text{(I-6)}$$

If one uses a bolometer or some other power-sensitive detector (e.g., a diode operated in the square-law region), the appropriate quantity is $|A|^2$ as shown in reference 21.

If the normal assumption is made that $\alpha a \ll 1$ and that measurements are made near a mechanical resonance, equations I-3, I-4, and I-5 take the simplified form:

$$|A| = (A_1^2 + A_2^2)^{1/2} = \frac{1}{[(\alpha a)^2 + a^2(k - k_m)^2]^{1/2}} \qquad \text{(I-7)}$$

$$A_1 = \frac{\alpha a}{(\alpha a)^2 + (k - k_m)^2 a^2} \qquad \text{(I-8)}$$

$$A_2 = \frac{(k - k_m)a}{(\alpha a)^2 + (k - k_m)^2 a^2} \qquad \text{(I-9)}$$

where $k_m = \frac{\omega_m}{v}$ and $\omega_m = \frac{2\pi m v}{a}$ related to the mth mechanical resonance.[7] Although these simplified equations are valid for many situations, for completeness, we continue with the more exact form as well as the simplified form.

Experimentally, one frequently selects a particular mechanical resonance and monitors the response at a fixed frequency on that resonance as a function of small changes in acoustic attenuation (absorption) and phase velocity (dispersion). Under these conditions, and for sufficiently small changes Δa and Δk in the acoustic properties, the corresponding changes in the response are given approximately by:

$$\Delta A_1 \approx \frac{\partial A_1}{\partial \alpha} \Delta\alpha + \frac{\partial A_1}{\partial k} \Delta k, \qquad \text{(I-10)}$$

$$\Delta A_2 \simeq \frac{\partial A_2}{\partial \alpha} \Delta\alpha + \frac{\partial A_2}{\partial k} \Delta k, \qquad \text{(I-11)}$$

where

$$\frac{\partial A_1}{\partial \alpha} = - \frac{\partial A_2}{\partial k} = \frac{a}{2} \frac{1 - \cosh\alpha a \cos ka}{(\cosh\alpha a - \cos ka)^2}, \qquad \text{(I-12)}$$

$$\frac{\partial A_1}{\partial k} = \frac{\partial A_2}{\partial \alpha} = - \frac{a}{2} \frac{\sinh\alpha a \sin ka}{(\cosh\alpha a - \cos ka)^2} \qquad \text{(I-13)}$$

and

$$\Delta|A| = \frac{\partial |A|}{\partial \alpha} \Delta\alpha + \frac{\partial |A|}{\partial k} \Delta k \qquad \text{(I-14)}$$

where

$$\frac{\partial |A|}{\partial \alpha} = \frac{a\exp(-\alpha a/2) - \exp(\alpha a/2)\cos ka}{2/\sqrt{2}(\cosh\alpha a - \cos ka)^{3/2}} \qquad \text{(I-15)}$$

$$\frac{\partial |A|}{\partial k} = \frac{a\exp(\alpha a/2)\sin ka}{2/\sqrt{2}(\cosh\alpha a - \cos ka)^{3/2}} \qquad \text{(I-16)}$$

The simplified equations for these partial derivatives becomes:

$$\frac{\partial A_1}{\partial \alpha} = - \frac{\partial A_2}{\partial k} = \frac{a[a^2(k - k_m)^2 - (\alpha a)^2]}{[(\alpha a)^2 + (k - k_m)^2 a^2]^2} \qquad \text{(I-17)}$$

$$\frac{\partial A_1}{\partial k} = \frac{\partial A_2}{\partial \alpha} = \frac{-a[2\alpha a^2(k - k_m)]}{[(\alpha a)^2 + (k - k_m)^2 a^2]^2} \qquad \text{(I-18)}$$

$$\frac{\partial |A|}{\partial \alpha} = \frac{-a^2 \alpha}{[(\alpha a)^2 + (k - k_m)^2 a^2]^{3/2}} \qquad \text{(I-19)}$$

$$\frac{\partial |A|}{\partial \alpha} = \frac{-a^2 (k - k_m)}{[(\alpha a)^2 + (k - k_m)^2 a^2]^{3/2}} \qquad \text{(I-20)}$$

I-2-3. VERIFICATION OF SENSITIVITY ENHANCEMENT FACTORS

The ultrasonic resonator used to verify the sensitivity enhancement factors consists of a flat and parallel single-crystal specimen of photoconductive CdS to which was bonded a 10-MHz x-cut quartz transducer so that longitudinal ultrasonic waves could be propagated along the direction of the C axis. (The effects produced by the presence of the transducer, which are unimportant to the discussion here, are considered in references 2, 17, 22). Ultrasonic waves interact with the charge carrier system of the CdS by the piezoelectric coupling mechanism.[9] Since the CdS specimen is photoconductive, small changes in the light intensity incident upon the specimen result in changes in the charge carrier system, which in turn change the acoustic properties of the resonator. The phonon-charge carrier coupling and the photoconductivity of CdS has been used to develop a quantitative ultrasonic calibrator,[10,11] the details of which are reported in section III-2. The small changes $\Delta\alpha$ and Δk needed to experimentally verify the sensitivity enhancement factors of equations I-12, I-13, I-15, and I-16 were produced with the aid of this calibrator.

The experimental arrangement used to obtain the line-shapes is shown in figure 2. The ultrasonic response is generated and detected by means

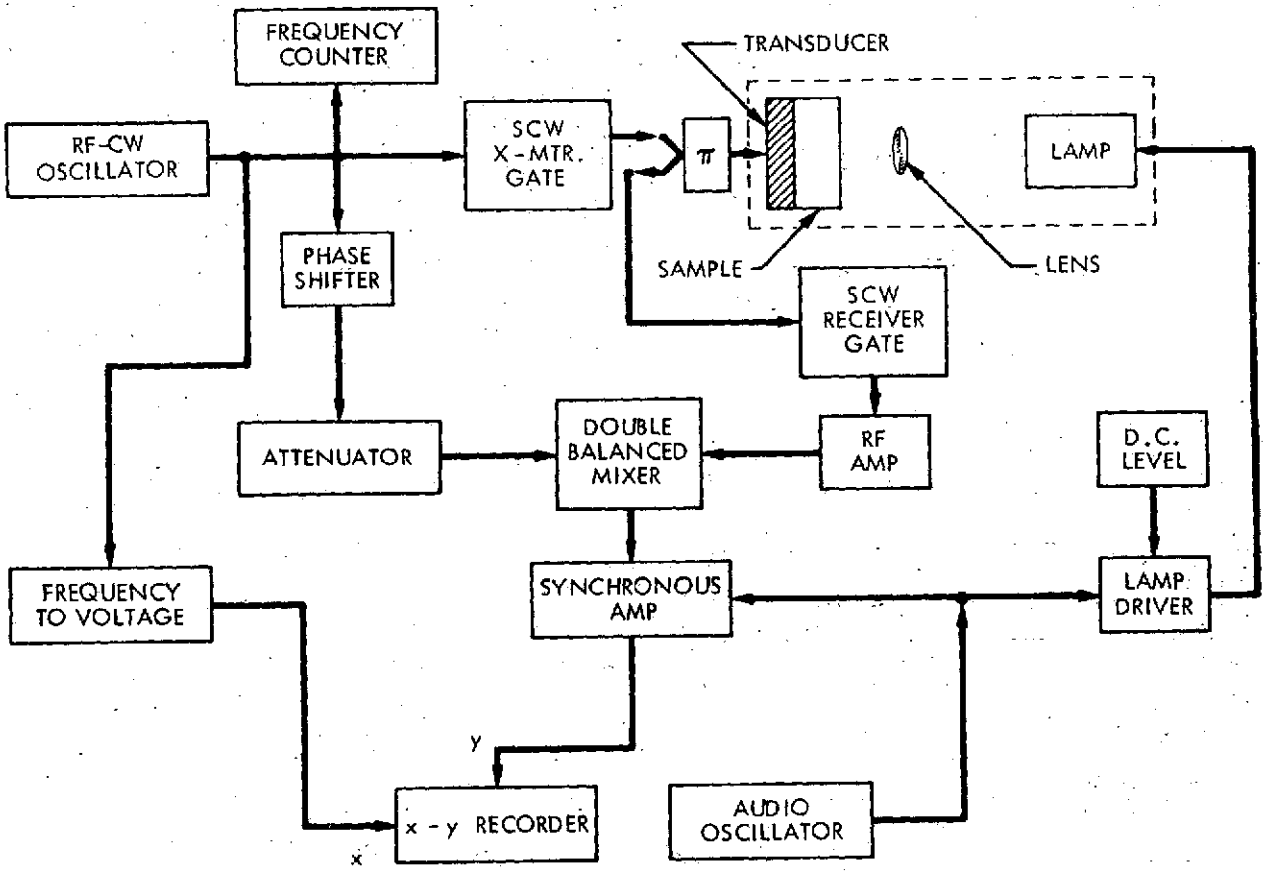

Figure 2) Block diagram of experimental arrangement used to verify resonator sensitivity enhancement factors.

of a sampled cw ultrasonic spectrometer[5]. Either A_1 or A_2 may be selected by the appropriate adjustment of the phase shifter in the reference arm of the double balanced mixer. The magnitude $|A|$ of the acoustic response is obtained by substituting a simple diode detector after the RF amplifier in place of the double balanced mixer.

The background ultrasonic properties of the resonator are determined in part by the setting of the dc level control (See figure 2) which fixes the average light intensity incident upon the CdS specimen. Small sinusoidal variations in light level are superimposed on this average value by the action of an audio oscillator which also serves as the reference signal for a synchronous amplifier. Depending upon the setting of the dc level control, these sinusoidal variations in light level produce corresponding variations in either the ultrasonic attenuation or the phase velocity, or in both of these. The corresponding changes in the acoustic response ΔA_1, ΔA_2, or $\Delta|A|$ are amplified and detected with the aid of the synchronous amplifier and displayed as a function of ultrasonic frequency on an x-y recorder.

The absorption and dispersion sensitivity enhancement factors $\partial|A|/\partial\alpha$ and $\partial|A|/\partial k$ predicted by equations I-15 and I-16 are presented in figure 3, for a range of frequencies near a particular mechanical resonance. A plot of $|A|$ over the same range is superimposed in the figure. The greatest sensitivity to absorption is seen to occur at the frequency corresponding to the peak of the mechanical response. (We note that $\partial|A|/\partial\alpha$ is negative for all frequencies since an increase $\Delta\alpha$ in attenuation results in a decrease in $|A|$.) Further, the dispersion sensitivity factor $\partial|A|/\partial k$ vanishes at the point where $\partial|A|/\partial\alpha$ gives the maximum absorption signal. Thus a pure absorption signal is obtained

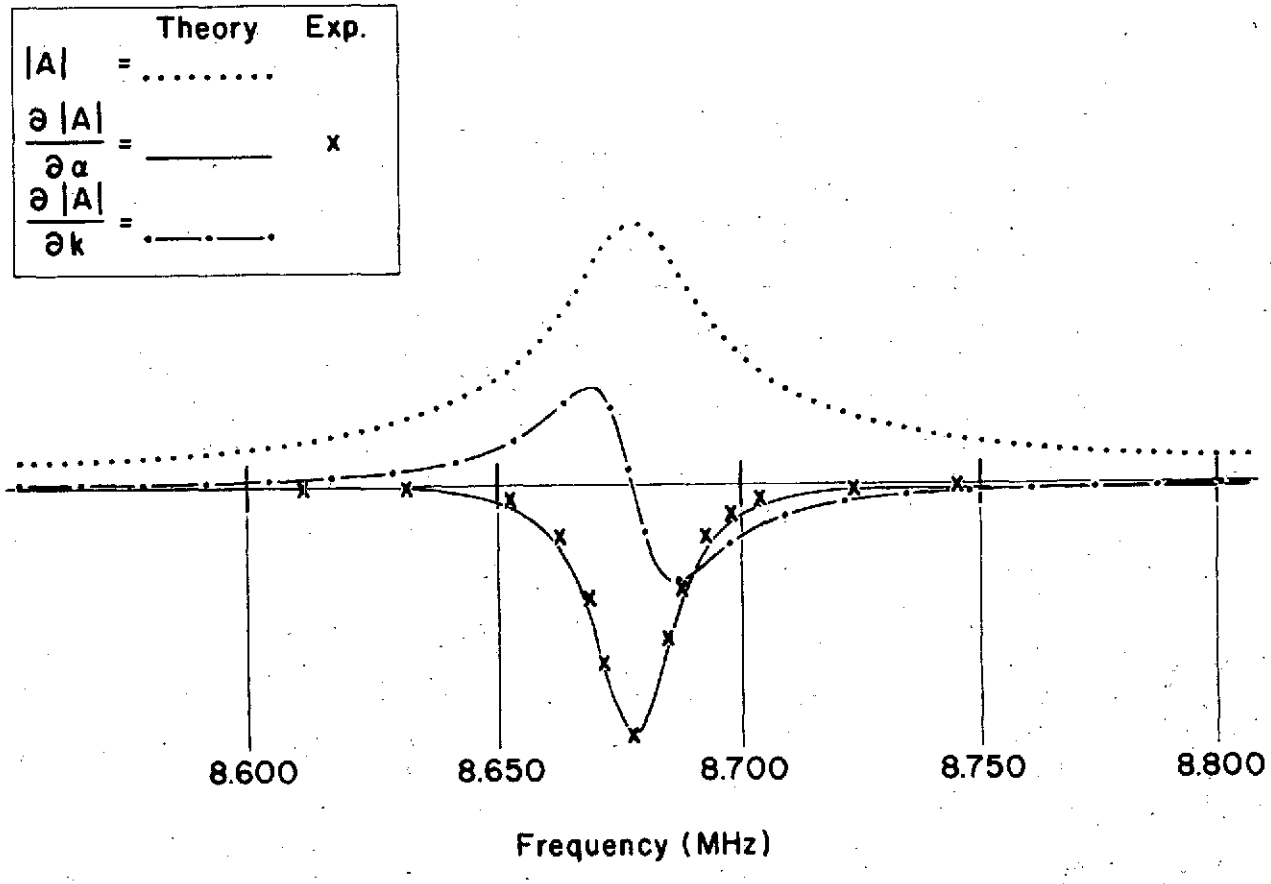

Figure 3) Absorption $\frac{\partial |A|}{\partial \alpha}$ and dispersion $\frac{\partial |A|}{\partial k}$ sensitivity enhancement factors superimposed on a plot of $|A|$.

when the spectrometer is tuned to the center of a mechanical resonance monitored via $|A|$. Examination of figure 3, however, indicates that there is no point on the $|A|$ response where one can obtain a pure dispersion signal.

The predicted lineshapes for both the absorptive $(\partial|A|/\partial\alpha)$ and dispersive $(\partial|A|/\partial k)$ sensitivity enhancement factors were experimentally verified. The theoretical curves are plotted using experimentally determined parameters for background attenuation, sample length, and velocity of sound, all known to better than $\pm 1\%$. The data for $\partial|A|/\partial\alpha$ are shown in figure 3. Agreement between theory and experiment is seen to be good. Because of details related to the operation of the CdS ultrasonic calibrator, the data for the $\partial|A|/\partial k$ had to be obtained using a value of background attenuation different from that used in figure 3 and thus could not be displayed on the same horizontal scale.

In figure 4, the agreement between theory and experiment for $\partial|A|/\partial k$ is also seen to be good.

The predicted absorption and dispersion sensitivity enhancement factors $\partial A_1/\partial\alpha$ and $\partial A_1/\partial k$ are shown along with the corresponding experimental data in figure 5. The data are in good agreement with the predictions of equations I-12 and I-13. The greatest sensitivity to absorption again occurs at the center of the mechanical resonance. Since $\partial A_1/\partial k$ is zero at that frequency, a pure absorption signal is obtained.

Of particular interest here is the existence of zeros of absorption sensitivity. These occur at frequencies such that the observed amplitude of A_1 is approximately one-half of its maximum amplitude. Physically, the zero-crossing of $\partial A_1/\partial\alpha$ can be interpreted in the following way: A small increase in attenuation produces both a

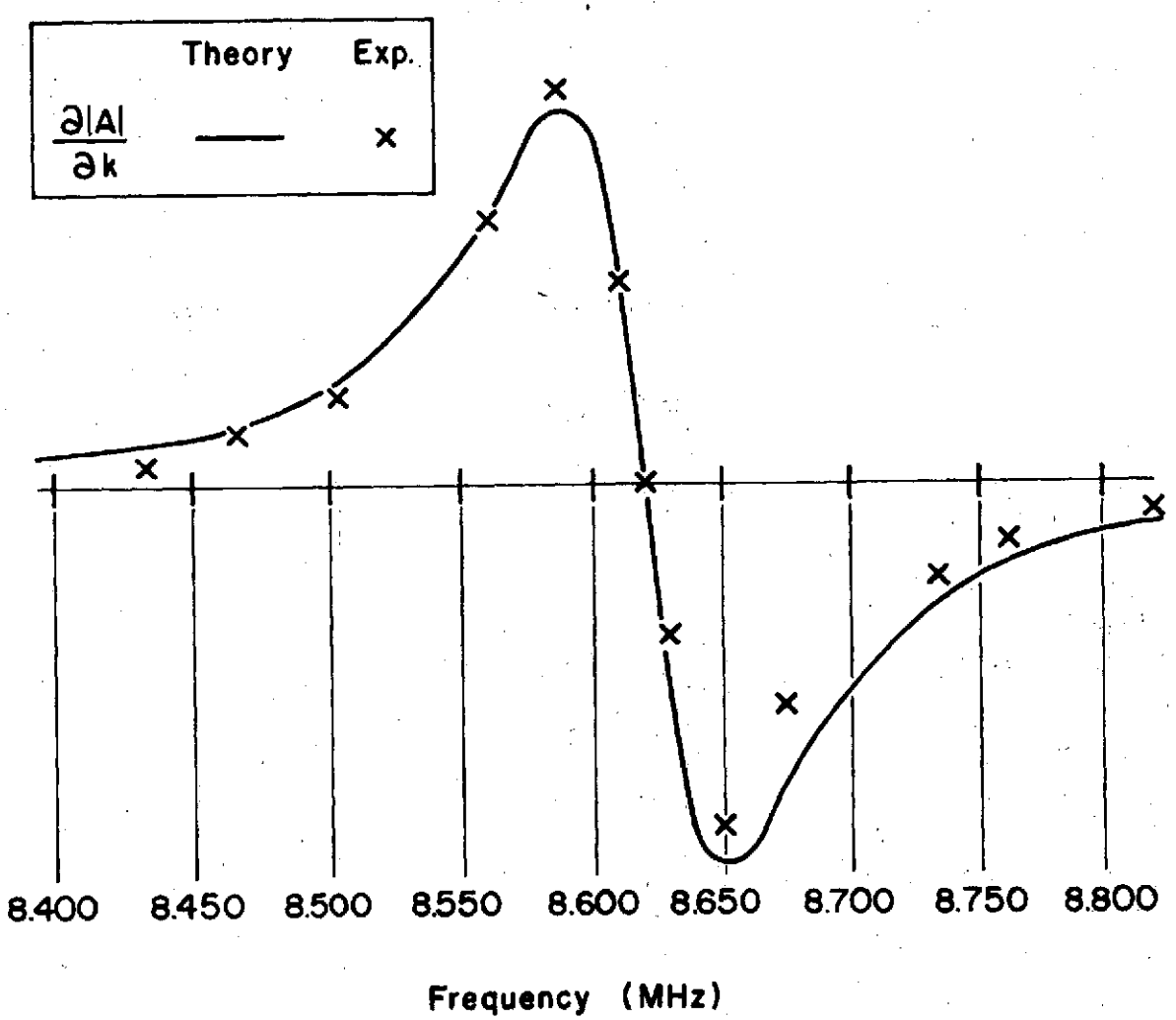

Figure 4) Dispersion $\frac{\partial |A|}{\partial k}$ sensitivity enhancement factor obtained at maximum α at 8.6 MHz. Note the zero crossover shift and frequency scale as compared to figure 3 or 5.

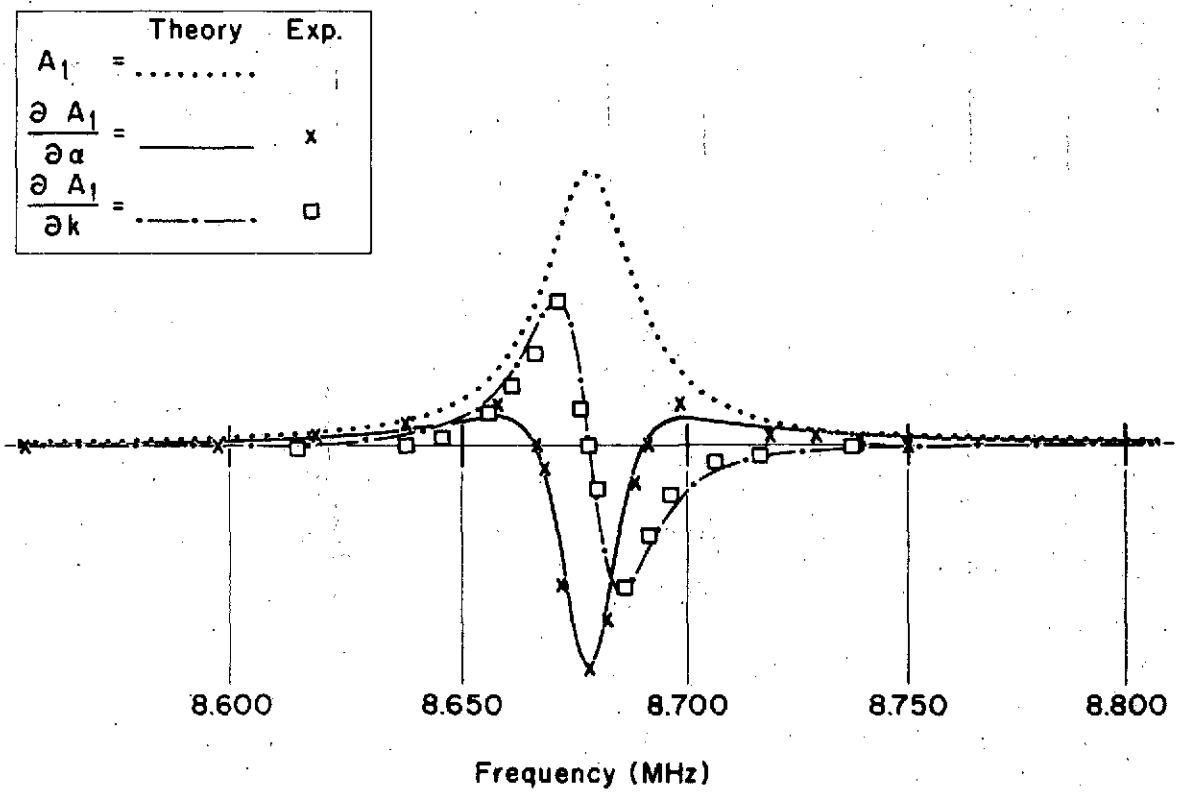

Figure 5) Theoretical and experimental absorption ($\partial A_1/\partial \alpha$) and dispersion ($\partial A_1/\partial k$) sensitivity factors superimposed on a plot of A_1. Pure absorption signals are obtained for the frequency corresponding to $\partial A_1/\partial k=0$, while pure dispersion signals are observed for $\partial A_1/\partial \alpha=0$.

decrease in peak height and a broadening of the curve. This broadening results in an increased amplitude for the wings of the curve A_1, even though the central portion of the curve is reduced. The zeros of the absorption sensitivity occur at those points in frequency where the decrease in amplitude resulting from the decrease in peak height is exactly canceled by the increase in amplitude due to the broadening.

A comparison of the results presented in figures 3, 4, and 5 indicates that one may obtain dispersion and absorption data separately by monitoring A_1, while this is not the case if one monitors $|A|$. The dispersion sensitivity $\partial A_1/\partial k$ is slightly less (~25%) than its greatest value when the frequency is adjusted to a point of zero absorption sensitivity (see figure 5), but this slight decrease is warranted in order to obtain pure dispersion data.

In practice, a scheme is used which obtains simultaneously pure absorption and pure dispersion data, both at their maximum theoretical sensitivity. Moreover, this arrangement includes a feedback loop which serves to lock the frequency of the oscillator to the desired point on the mechanical resonance. This scheme uses both the in-phase signal A_1 as well as the out-of-phase signal A_2 described in equations I-8 and I-9. The experimental arrangement is as follows: Two independent phase-sensitive detectors of the type shown in figure 2 are utilized. The reference arm of one is adjusted to produce an A_1 response, while the reference arm of the other is adjusted to yield A_2. The frequency is tuned to coincide with that of the center of the mechanical resonance. As shown previously, $\partial A_1/\partial \alpha$ provides its greatest sensitivity while $\partial A_1/\partial k$ is zero under these conditions. Thus one obtains a pure absorption signal at maximum theoretical sensitivity from the A_1

monitoring unit. Referring to equations I-12 and I-13, however, we notice that $\partial A_2/\partial k$ is at its greatest sensitivity while $\partial A_2/\partial \alpha = 0$ at this same frequency. Thus the A_2 monitoring unit simultaneously provides a pure dispersion signal, this also at its maximum theoretical sensitivity. The A_2 monitoring unit also provides the correction voltage for a frequency locking scheme which has been discussed elsewhere.[23]

II. ULTRASONIC TECHNIQUES AND APPLICATIONS

II-1. SAMPLED CONTINUOUS WAVE ULTRASONIC SPECTROMETER

In this section, two new ultrasonic measurement systems are described in detail. One of these is a refinement of the SCW[5,17] system while the other is a new system[6] based on marginal oscillation techniques with maximum sensitivity enhancement[2] (see section I-2). An RF amplitude regulation system[8] is presented and its application to the new spectrometer is described. Finally, applications of the new spectrometer in the medical sector are demonstrated along with a discussion of current research applications of the new spectrometer for NASA.

The two major catagories of ultrasonic spectrometers are pulse-echo (PE) and continuous wave (CW). Sophisticated systems of each type have been used extensively for physics research. However, there are drawbacks to each basic system. By its very nature, pulse-echo systems cannot produce monochromatic phonons thus direct measurement of narrow resonant phenomona (e.g. Nuclear Acoustic Resonance) are difficult since the narrow pulse leads to inhomogeneous broadening[7] of the response. Most CW techniques do not have the same drawbacks as pulse-echo systems. However, since these systems are typically used for transmission resonance, they have the problem of "crosstalk", which is electromagnetic leakage around the sample. "Crosstalk" is especially serious for thin or very high loss specimens. The problems associated with "crosstalk" are presented in references 19 and 24 and are shown to be a limiting factor in the use of CW systems. A recently developed ultrasonic technique[5,17]

has combined some of the attributes of pulse-echo with CW in a system called a Sampled Continuous Wave Ultrasonic Spectrometer (SCW). This system is capable of producing a monochromatic phonon without the problem of "crosstalk".

The SCW is a stimulus response type of measurement system but does not use the very narrow RF pulse used in PE systems. Simply, the SCW uses a wide stimulus pulse and then measures the decay of the resulting acoustic wave. This can be related to the CW system described in section I-2 by looking at equation I-1. The infinite summation shown in this equation is the superposition of all the waves in the resonator (see figure 1). In contrast, in an SCW system, the series is terminated at the instant τ_d when the transmitter gate (see figure 6) is closed. At the instant τ_d the first term in the series vanishes. At a time $t = \tau + \tau_d$ (where $\tau = \frac{a}{v}$ or one "round trip" reflection time in the resonator) the second term vanishes, and so on.[25] Therefore, the decay of energy in the ultrasonic wave appears as a series of steps corresponding to terms vanishing in the infinite series of equation I-1. The resulting signal may be compared with CW signal by sampling the decaying signal. In fact, it is possible to obtain good agreement with the superposition theory by sampling an interval in the decay as close as possible to τ_d and by making the interval wider than several τ. The early sampling does not permit too many terms in the series to "turn off" whereas the interval width averages the acoustic information during the interval. Therefore, the SCW is a system capable of measuring the acoustic response of a resonator without the problems of "crosstalk" or non-monochromaticity.

The SCW system requires a precise sequence of gating pulses to control the oscillators, amplifiers and signal samplers. Referring to

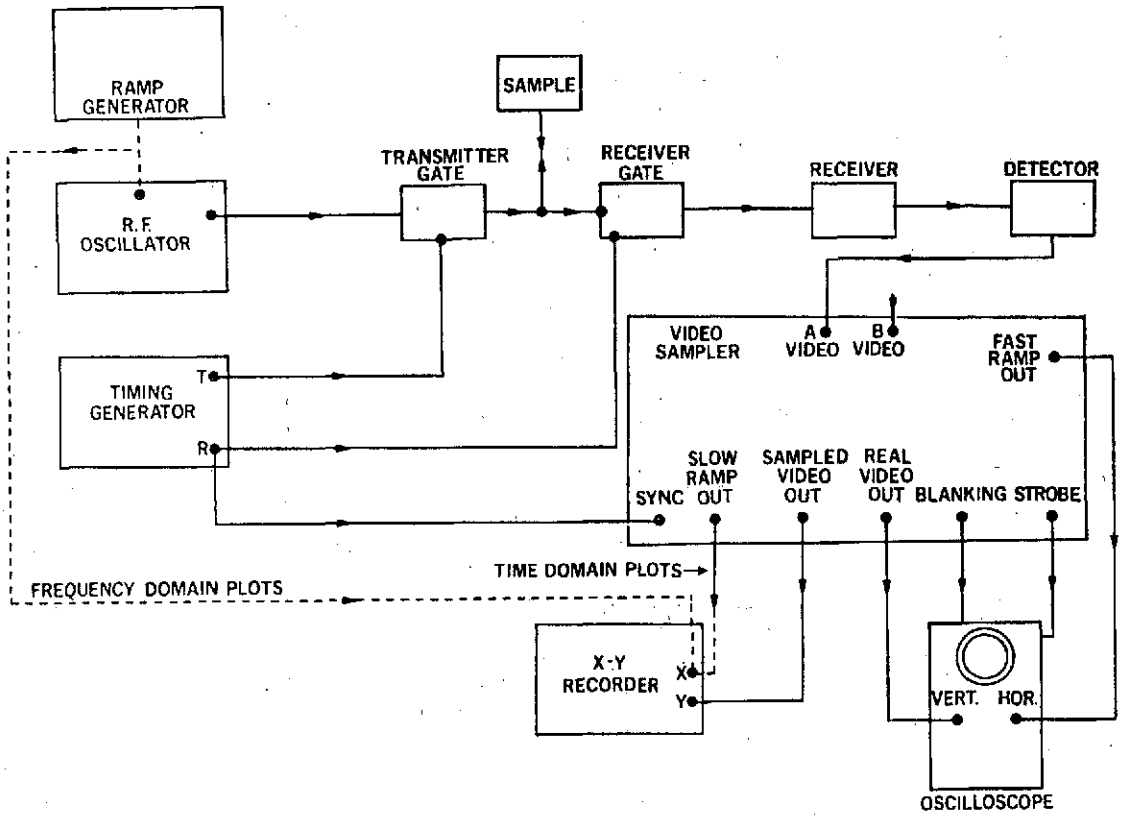

Figure 6) Block diagram of a sampled continuous wave ultrasonic spectrometer (SCW) for measuring absorption or dispersion. For figures of time domain decays, the slow ramp drives the X axis of the X-Y recorder. For frequency domain figures, the ramp generator sweeps both the RF oscillator frequency as well as the X axis.

figure 6 again, a repetitive pulse train must first turn on the RF (open the transmitter gate), turn off the RF and delay a short time for the electronics to stop ringing, and open the receiver gate so that the RF ultrasonic decay can be amplified and detected. Finally, the detected signal must be sampled so that a voltage corresponding to a time in the ultrasonic decay may be recorded. The two basic components of this system are the timing generator and the video sampler as shown in figure 6. In addition, a signal processing system is often useful to band pass the sampled signal, to provide a ramp generator to sweep the frequency of the RF oscillator, and to generate an exponential decay electronic signal which may be compared with the ultrasonic decay signal. Therefore, a schematic of the signal processing system is included for completeness along with a complete description of the basic components.

The timing generator shown in figure 7, provides the various sync pulses and gate pulses which control the SCW. We follow a pulse through the system to understand how it works. A (+) pulse into the schmidt trigger produces a bypolar pulse, which is differentiated and the leading (+) edge triggers a fast NOR gate (380). The 380 output is a fast (-) spike which starts the first "one shot" monostable multivibrator (362). The output of the 362 is a square pulse whose length is determined by external resistors and capacitors. In addition to the normal X output of the 362, a complement $\bar{X}$ output is provided which both fires a 356 line driver for a master sync pulse as well as firing the next 362 - the transmitter logic. The fall of the transmitter square pulse triggers a delay logic 362, the fall of which triggers the receiver logic. Both the transmitter and receiver use current limited line

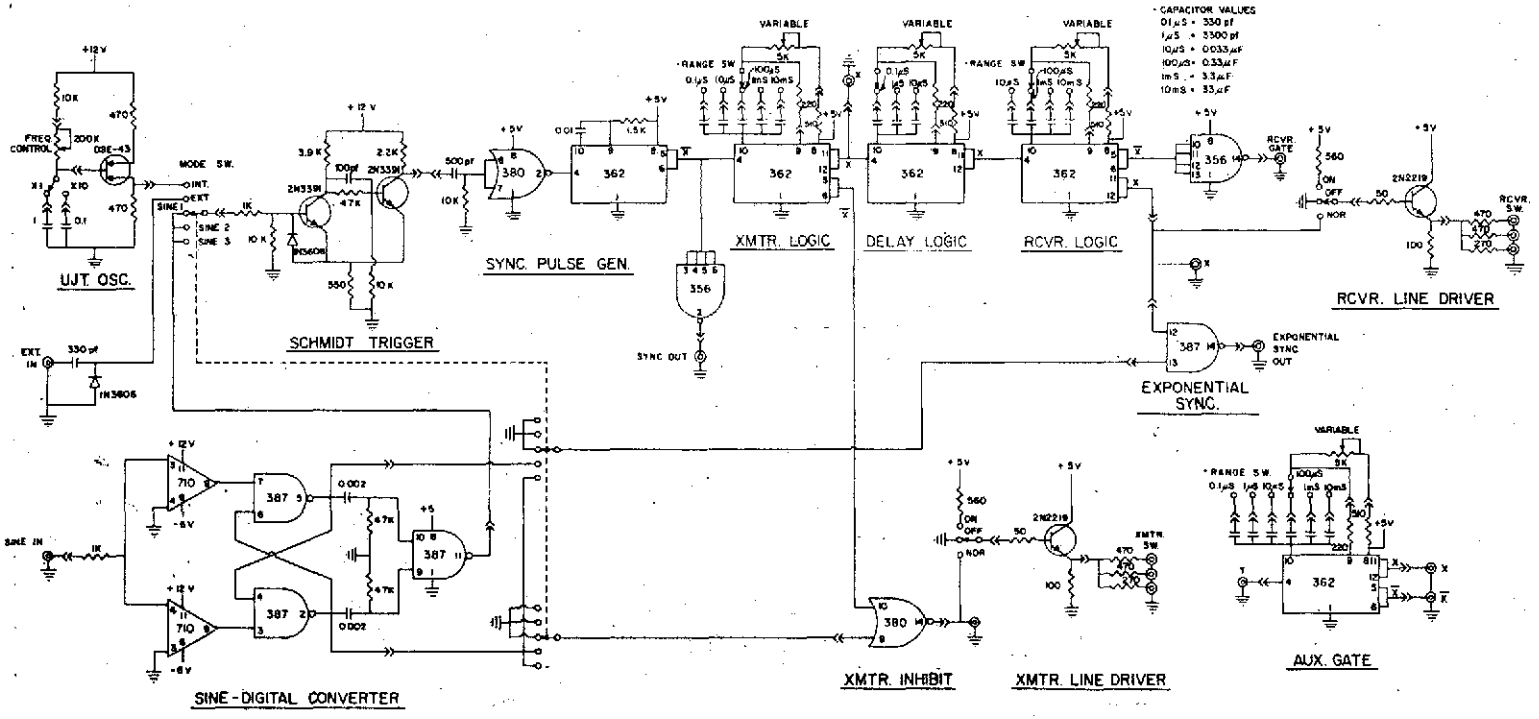

Figure 7) Schematic diagram of the timing generator section of the Sampled Continuous Wave Ultrasonic Spectrometer. Component values shown in ohms and microfarads.

drivers (2N2219) to protect the RF electronic gates (double balanced mixer modulators) from burn-out currents. An auxiliary 362 gate is available for controlling some other part of the experiment - i.e. a strobe lamp, a magnet, or some other stimulus.

The other logic function of the timing generator is related to its input mode. An input mode switch selects either internal, external or 3 sine input modes. The internal mode uses the unijunction transistor oscillator (UJT) as a master clock to run the rest of the circuitry. The external mode requires a periodic external 6 volt (+) pulse to act as the master clock. In any of the sine input modes, an external sine wave acts as the master clock. The zero crossings of the sine wave produce sharp (+) spikes out of the sine-digital converter for the schmidt trigger input. In the sine 1 position, the transmitter fires with each zero crossing so that an electronically generated exponential can be produced every receiver pulse. In the sine 2 position, the transmitter fires every other zero crossing with an exponential generated only at the time of the receiver pulse following the transmitter pulse. In the sine 3 position, the transmitter fires every other zero crossing with an exponential generated only at the time of the receiver prior to the transmitter pulse.

The three sine inputs are designed to facilitate data processing. In sine 1, the electronically generated exponential may be compared with the ultrasonic decay or may be subtracted from it for the measurement of small changes in signal. In sine 2 position, measurement of the signal is followed by one of the noise so that synchronous detection may be used to enhance weak signals. With the electronic exponential, sine 2 position is used to sample changes in signal and then noise by

subtracting the electronic from the ultrasonic exponential. In effect, this transforms the signal back to a zero voltage signal reference. Sine 3 differs from sine 2 in that the noise is transformed up to the signal level rather than the signal being transformed to the noise level. The sine 3 position is useful for recording the signal level as well as changes in the signal level.

The second major component of the SCW is a high speed sampling system similar in nature to a sampling oscilloscope. The sampler, shown in figure 8, is interconnected to the timing generator so that a measurement of the input signal (a detected ultrasonic decay) is made at a chosen time after the receiver gate opens. The logic of the sampler can be described by following its reaction to a repetitive pulse at the sync input. The trigger level and polarity are adjusted at the input of a 710 voltage comparator. When triggered, the output pulse of the 710 is differentiated and the (+) part sets a control flip-flop, lights a sync indicator lamp, and starts the fast ramp generator.

The generator produces a fast ramp (5×10^{-2} to 1×10^{-5} seconds) which is compared to a slow ramp (0.5 - 4 minutes) started by a switch on the front panel. When the 2 ramps have the same output voltage, the ramp comparator 710 initiates the measurement of the input signal (video A or B). As the slow ramp increases in voltage, the measurement is taken later in the fast ramp sweep so that eventually measurements are taken from the beginning of the fast ramp to the end of the fast ramp. If the fast ramp output is used to sweep the horizontal axis of an oscilloscope with the video A or B used to drive the vertical axis, use of the slow ramp as described above corresponds to measuring the entire input signal displayed on the scope. When used in this fashion, a

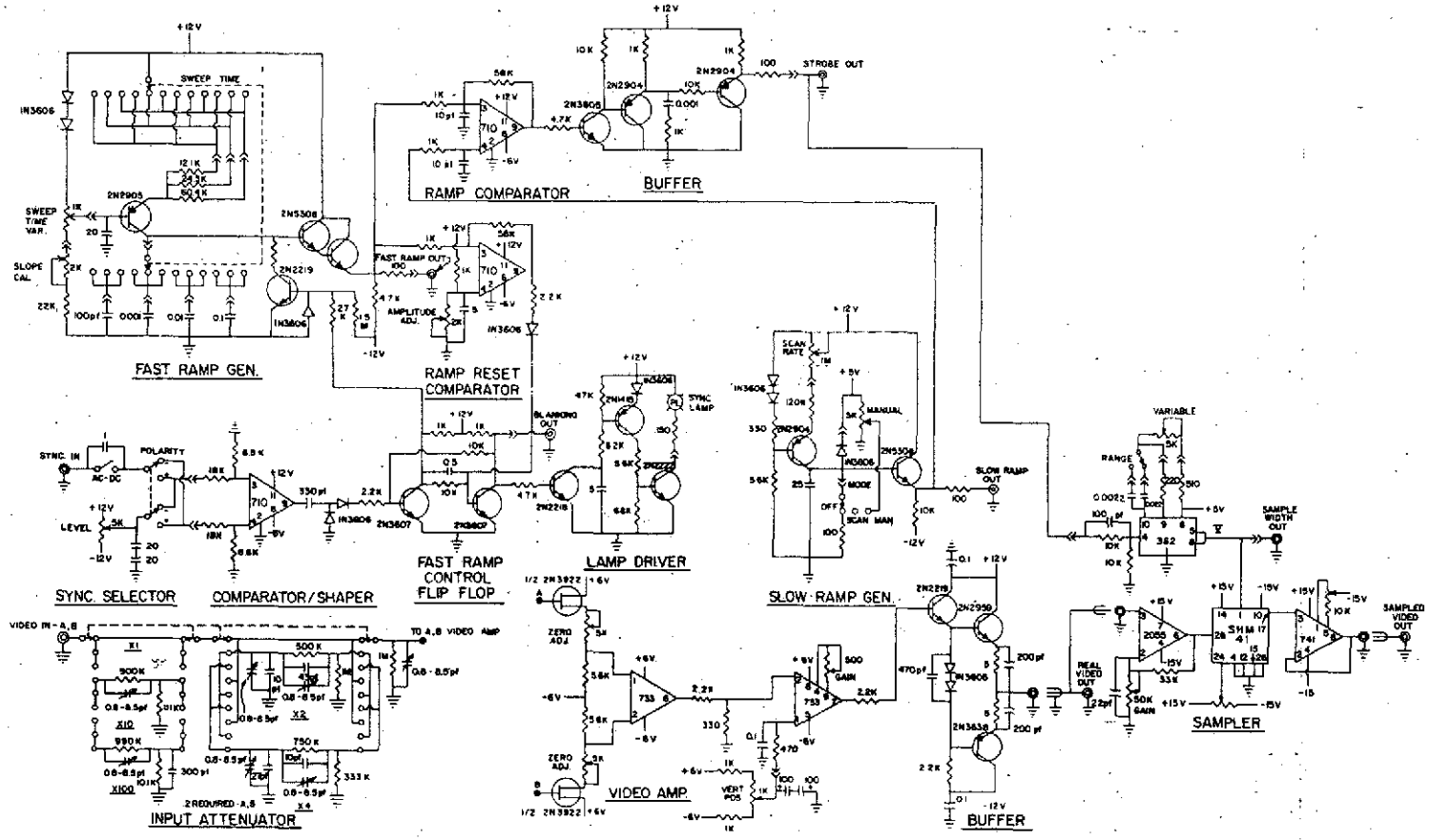

Figure 8) Schematic diagram of the signal sampling system of the Sampled Continuous Wave Ultrasonic Spectrometer. Component values shown in ohms and microfarads.

blanking pulse is provided to turn off the scope trace during the reset of the fast ramp.

In addition to the blanking pulse, a strobe pulse is available for use with a scope. The strobe signal intensifies the area of the display after the sampled measurement is taken. The strobe pulse starts a monostable multivibrator (362) whose output width is adjustable and controls the sampler's measurement window. The sampler is a Burr Brown sample and hold module which tracks the input signal during the duration of the strobe pulse and holds the last sampled value thereafter. An integrator is inserted at pin 28 of the sampler for measurements which require time averaging of the input signal. The time constant of the integrator is chosen to correspond to the measurement window width. The remainder of the sampler system consists of two identical input attenuators (A and B) in steps of 1, 2, 4 up to 400. These two inputs are connected to a differential MOSFET high input impedance device and amplified by a two stage 733 video amp. The signal is buffered to drive an output and the sampler module.

The sampler system can be operated in 3 modes which control the slow ramp generator. The modes are "off", "scan", and "manual". In the "off" mode a sample is taken at the same time as the sync input pulse (neglecting any propagation delay). In the "manual" mode, a sample is taken at any set time during the fast ramp. In "scan" mode, a sample is taken from the beginning to the end of the fast ramp by consecutively sampling later with each sync pulse. By connecting the slow ramp out to the X axis of a chart recorder and the sampled video out to the y axis, a complete plot of the input signal can be obtained (for the duration of the fast ramp).

The signal processing section shown in figure 9 of the SCW system consists of a band pass filter (an integrator), a ramp generator and an exponential generator. These circuits are straight-forward and require no additional explanation.

Figure 10, is a photograph of an SCW system complete with a stepwise ultrasonic decay displayed on the scope.

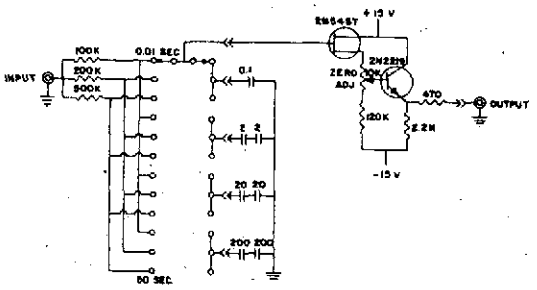

TIME CONSTANT

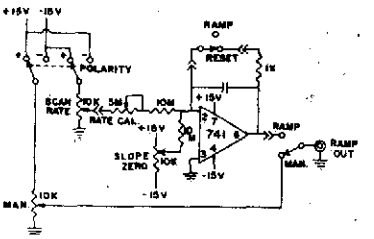

RAMP GENERATOR

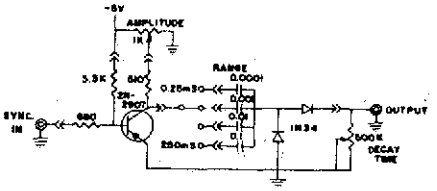

EXPONENTIAL GENERATOR

Figure 9) Schematic diagram of the signal processing section of the Sampled Continuous Wave Ultrasonic Spectrometer. Component values shown in ohms and microfarads.

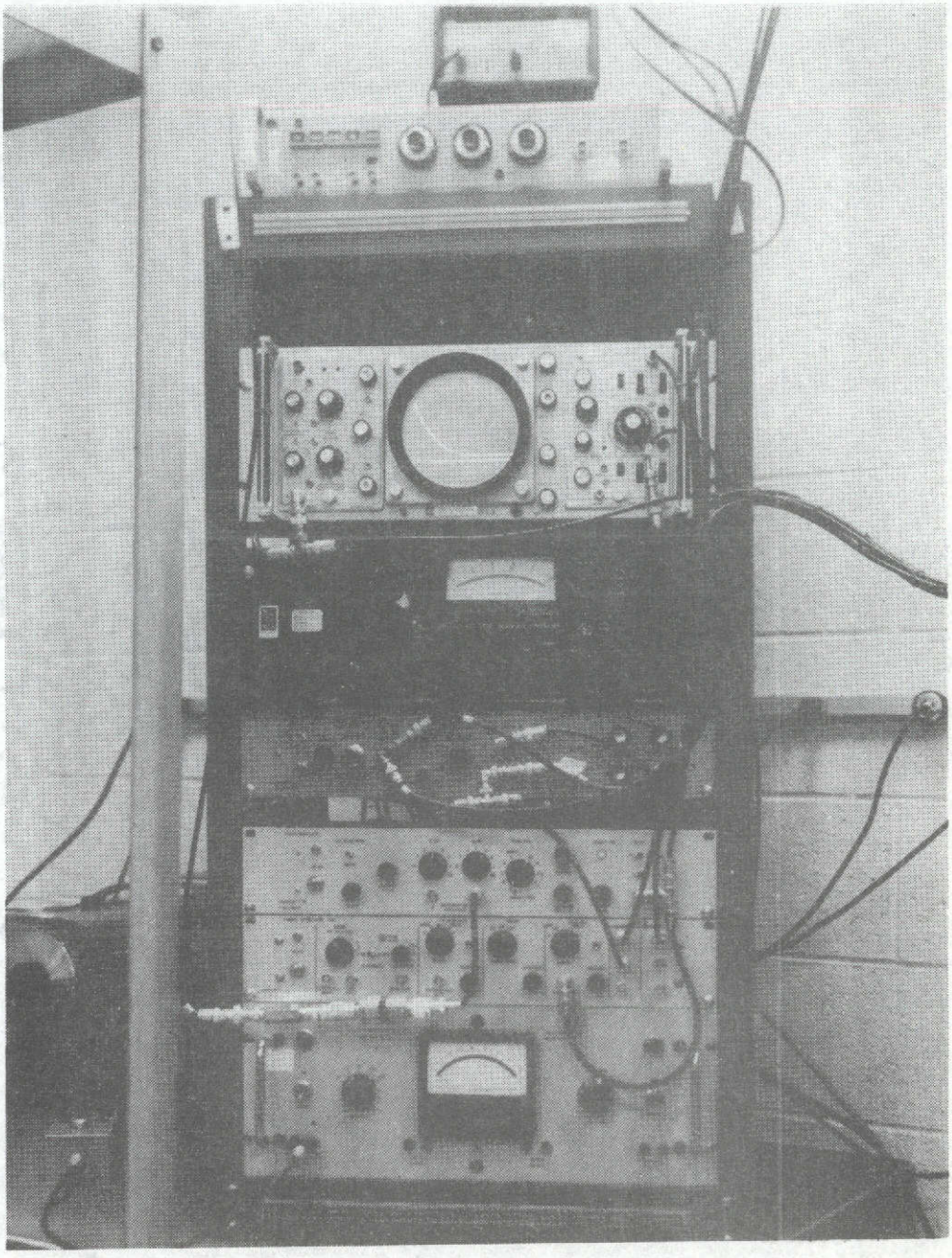

Figure 10) Photograph of a Sampled Continuous Wave Ultrasonic Spectrometer (oscillator not shown). A resonator exponential step-wise decay obtained with this system is shown on the oscilloscope.

II-2. TRANSMISSION OSCILLATOR ULTRASONIC SPECTROMETER

The second ultrasonic measurement system to be described is a Transmission Oscillator Ultrasonic Spectrometer (TOUS)[6]. This CW device exhibits high sensitivity because it utilizes maximum sensitivity enhancement as well as marginal oscillation. In spite of its high sensitivity, the TOUS system is relatively simple, compact, and inexpensive. These features suggest that the TOUS is suitable not only for precise laboratory measurements of the physical properties of materials, but also for applications in many fields (e.g. medical monitoring, lubricant monitoring).

An important aspect of the design of the TOUS is its marginal oscillation. A previous device, the Marginal Oscillator Ultrasonic Spectrometer (MOUS) seemed to exhibit the highest sensitivity to measuring small changes in ultrasonic absorption[17,18]. Nuclear magnetic resonance workers have long exploited the sensitivity of oscillators which are operated on the verge of dropping out of oscillation (and thus are "marginal"). The marginal oscillator concept was adapted to ultrasonic use for the study of nuclear acoustic resonance.[26] Although the MOUS system has been utilized for nuclear acoustic resonance studies and for other applications,[17,27] the inherent complexity of the MOUS has severely limited its usefulness. The TOUS appears to have the same high sensitivity characteristics as the MOUS without the inherent problems.

DESCRIPTION

A block diagram of the TOUS is shown in figure 11. Central to any continuous (i.e., standing) wave ultrasonic system is the acoustic

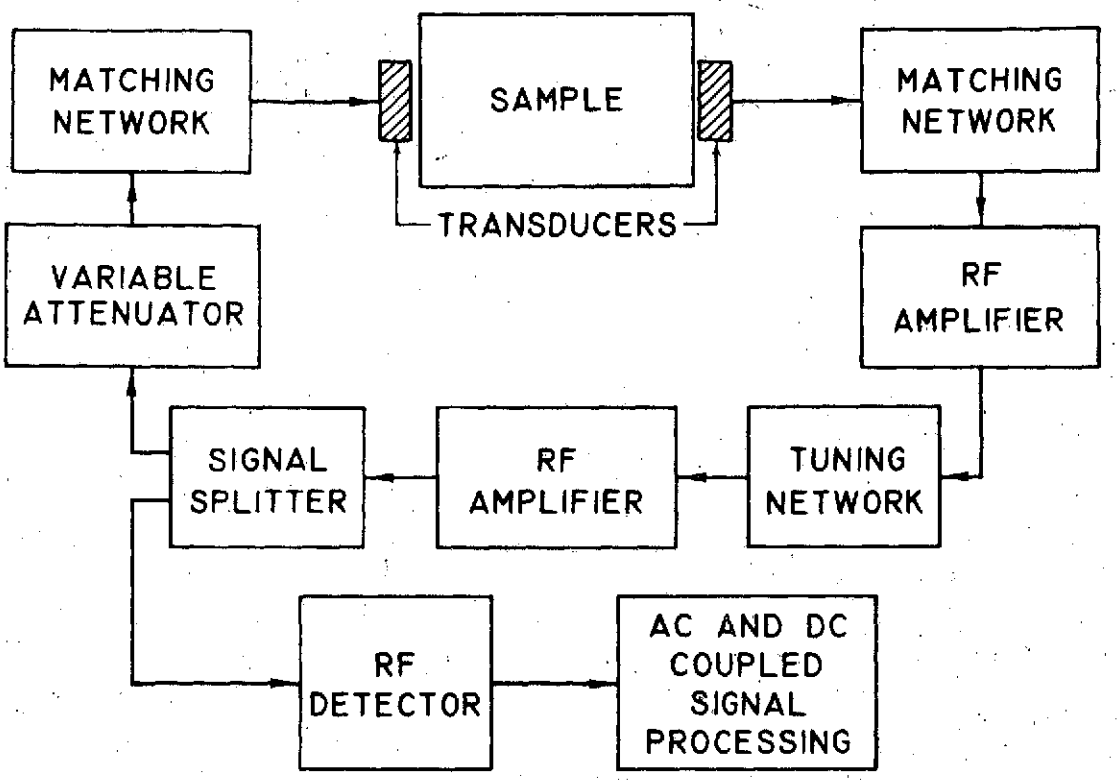

Figure 11) Block diagram of a Transmission Oscillator Ultrasonic Spectrometer (TOUS).

resonator, in this case consisting of the sample plus two transducers arranged in a transmission assembly. The response as a function of frequency of the acoustic resonator consists of a series of standing wave (mechanical) resonances. Operating the spectrometer at a point (often chosen to be the peak) on one such mechanical resonance results in enhanced sensitivity to small changes in the acoustic phase velocity and attenuation of the sample.[3,17]

As indicated in figure 11, the TOUS consists of an amplifier system which is caused to oscillate by providing it with a feedback path through the acoustic resonator. Pi matching networks provide impedance matching between the acoustic resonator and the electrical system. A tuning network selects the particular mechanical resonance and the point on that resonance at which the oscillator operates. The tuning network is a passive bandpass filter having a frequency response which is broad compared to the width of a mechanical resonance but sharp enough to discriminate between adjacent mechanical resonances. In practice, an inductor and a variable capacitor in parallel are used as a tank circuit. With loosely coupled input and output coils, the desired frequency response is achieved, the insertion loss being 10-20 dB at frequencies of the order of 10 MHz.

The loop contains two lossy elements, the tuning network and the acoustic resonator, both of which act as narrow bandwidth filters. This arrangement permits the distribution of the gain around the loop as shown in Figure 11, with the result that lower noise is achieved. Only that fraction of the output noise of one amplifier which lies within the passband of the intervening narrow band element is seen by the input of the other amplifier. A signal splitter removes a portion of the signal

at the highest RF level in the system for detection and signal processing. The variable attenuator, as discussed later, is adjusted to achieve marginal oscillation

THEORY

Stable oscillations of the TOUS occur at a level at which the phase shift around the loop is zero and the product of the gain G and the loss p is one. In the discussion which follows, it is assumed that the condition on the phase shift is satisfied and that the fact that the gains and losses are distributed around the loop can be ignored.

The enhanced sensitivity obtained by operating the TOUS under conditions of marginal oscillation can be understood on the basis of the following argument. If the output voltage V_{out} is plotted as a function of the input voltage V_{in} for a typical RF amplifier, a response curve similar to that shown in figure 12(a) is obtained. For sufficiently small input voltages, the response is nearly linear and thus the gain $G = V_{out}/V_{in}$ (also shown in figure 12(a)) is nearly independent of V_{in}. Departure from linearity at higher RF levels is accompanied by a decrease in gain, i.e., the amplifier approaches saturation.

To be utilized for the TOUS, the small signal gain of the amplifier must exceed the attenuation, i.e., the product of the linear region gain and the loss must be greater than 1.0. Under these conditions, oscillations, when initiated, grow in amplitude. The gain of the amplifier decreases with this increase in oscillation level. Stable oscillations occur when the amplitude has increased sufficiently, and

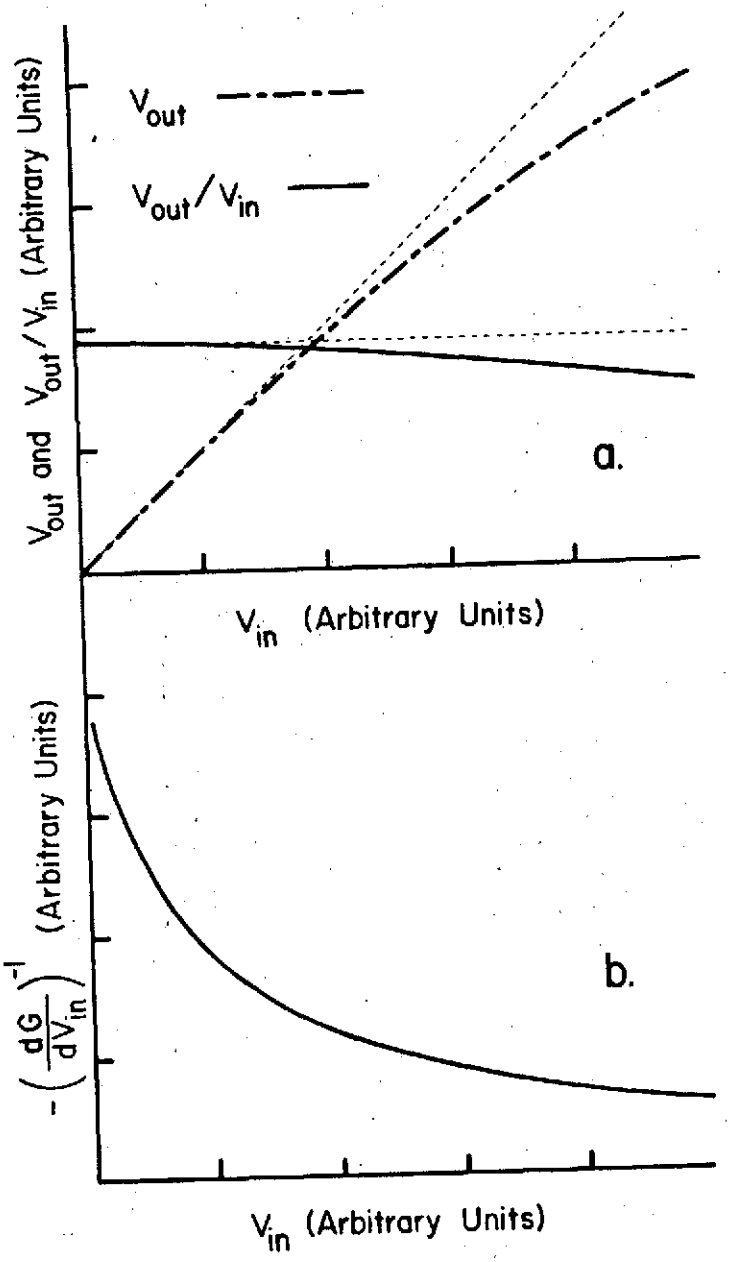

Figure 12) (a) Output voltage (V_{out}) and gain (V_{out}/V_{in}) versus input voltage (V in) for a hypothetical RF amplifier.
(b) $-(dG/dV_{in})^{-1}$ versus V_{in}, showing the enhanced sensitivity in the nearly linear region of the hypothetical amplifier.

thus the gain has decreased sufficiently, that the product of the gain and loss equals 1.0. Stable oscillations cannot occur in a region where the amplifier is strictly linear.

The primary use of the TOUS is in the detection of very small changes in acoustic attenuation. A small increase in acoustic attenuation results in a corresponding small increase in the attenuation of the loop. The small increase in loop attenuation reduces the RF level at the input of the amplifier and a slight increase in gain results (figure 12(a)). A new stable operating point is reached since the extra loss due to the additional acoustic attenuation is compensated by the additional gain. A measure of the sensitivity of the TOUS to small changes in acoustic attenuation α is the change in output level ΔV_{out} for a given $\Delta\alpha$. From the discussion above and an inspection of figure 12(a), one sees that the greatest change in V_{out} will occur in that region of the curve where the gain G is a rather slowly varying function of V_{in}. When dG/dV_{in} is small, the value of V_{in} (and thus the value of V_{out}) must decrease rather substantially in order to increase the gain sufficiently to compensate for the additional loss. Conversely, if dG/dV_{in} is large, only a relatively small change in output level results for the same change in acoustic attenuation $\Delta\alpha$.

These considerations can be made more quantitative in the following way. Since the condition $Gp = 1$ is always satisfied, a small fractional change $\Delta p/p$ in loss resulting from an increase in acoustic attenuation produces a corresponding change ΔG in the gain of the amplifier,

$$\Delta G = -G(\Delta p/p) \qquad \text{(II-1)}$$

The change ΔV_{out} in output voltage resulting from this change in gain is $\Delta V_{out} = (dV_{out}/dG)\Delta G = (dV_{out}/dV_{in}) \times (dV_{in}/dG)\Delta G$. Using equation II-1 and making the approximation $dV_{out}/dV_{in} = G$, one obtains

$$\Delta V_{out} = -(dG/dV_{in})^{-1} G^2 (\Delta p/p) \qquad \text{(II-2)}$$

Thus the sensitivity of the TOUS to small changes in acoustic attenuation is approximately proportional to $-(dG/dV_{in})^{-1}$. This is plotted in figure 12(B) for the hypothetical amplifier having the response shown in figure 12(A). Good sensitivity is achieved with amplifiers which are nearly linear and saturate slowly. Sensitivity increases when the operating point is chosen at RF levels where the amplifier is more nearly linear. In practice, the operating point is chosen by adjusting the variable attenuator shown in Figure 11.

To demonstrate some of the characteristic features of the TOUS, it is convenient to be able to produce small changes in ultrasonic attenuation of known magnitude. An ultrasonic calibration instrument[10,11] described in Section III-2 is used for that purpose. This calibrator makes use of an acoustic resonator consisting of two transducers bonded to a single crystal of CdS, the acoustic properties of which are modulated with a light beam. For this study, the light beam was chopped at 26 Hz and the detected output of the TOUS was passed through a narrow bandwidth filter (~ 3 Hz) centered at 26 Hz before final demodulation.

The amplitude of the 26 Hz audio output of the TOUS is plotted as a function of the RF level in figure 13. The change in acoustic attenuation of the CdS specimen which is responsible for the 26 Hz output was fixed at $\Delta\alpha = 6.4 \times 10^{-}$ cm^{-1}. The RF level was decreased

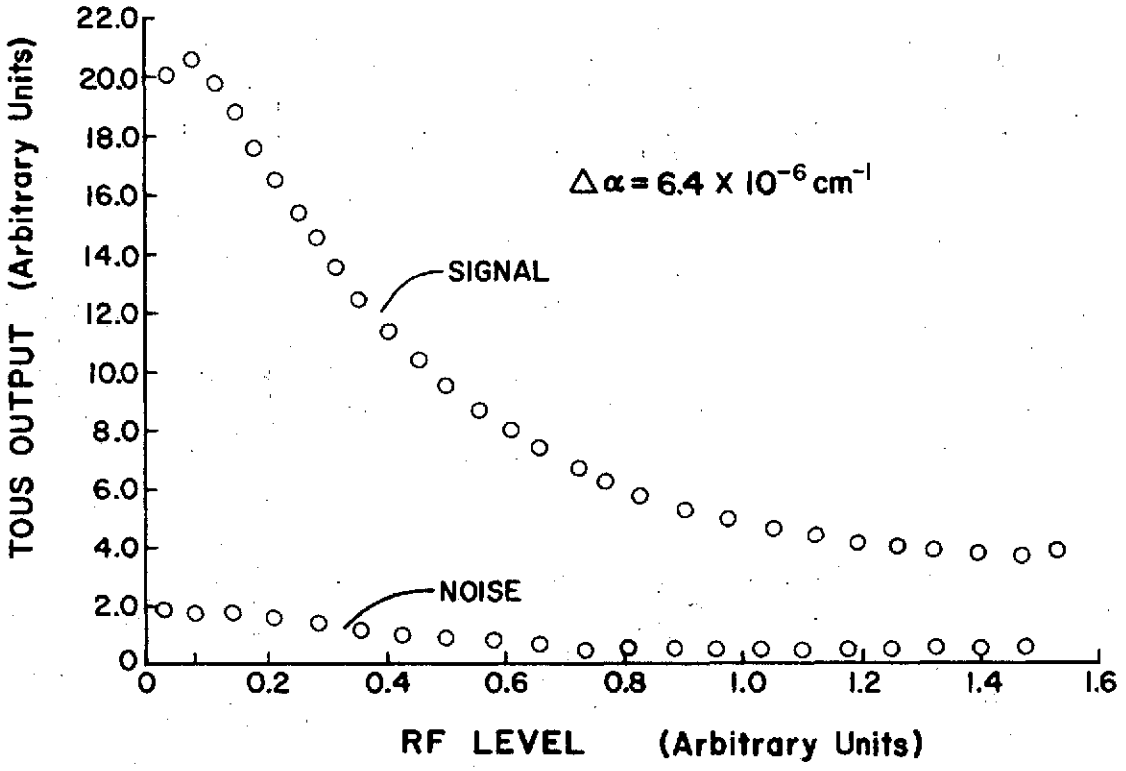

Figure 13) Output of the TOUS in a 3 Hz bandwidth centered at 26 Hz as a function of RF level. The change in acoustic attenuation was fixed at $\Delta\alpha = 6.4 \times 10^{-6}$ cm^{-1}. The increased output at low RF levels is consistent with the predictions of equation II-2 and figure 12 B.

(from right to left in figure 13) by adding attenuation to the loop by means of the variable attenuator. The amplitude of the 26 Hz audio output of the TOUS increases with increasing insertion loss even though a higher insertion loss means a lower RF operating level. These results look qualitatively like those presented in figure 12(b) where a functional form has been assumed for the input-output relationship of the amplifier. The increasing 26 Hz signal output with decreasing oscillation level is due to the $-(dG/dV_{in})^{-1}$ factor of equation II-2. The qualitative agreement makes us believe that our theoretical remarks are essentially correct in describing this aspect of the operation of the TOUS.

The signal-to-noise ratio obtained under these conditions is indicated in figure 13, where the noise output of the TOUS is shown on the same vertical scale as that for the signal. The optimum signal-to-noise ratio is usually achieved at an RF level slightly higher than that corresponding to the maximum audio (e.g., 26 Hz) signal.

A limited performance comparison of a TOUS system with a more conventional continuous wave (CW) transmission ultrasonic spectrometer is presented in figure 14. The TOUS system shown in figure 11 can be converted to a conventional CW spectrometer by opening the loop after the signal splitter and inserting a stable RF oscillator. This comparison is reasonably meaningful since all components function in the same fashion in both systems. (The stable RF oscillator was not a significant contributor to the noise in the conventional CW system.) The audio output and corresponding noise in a narrow band centered at 26 Hz are shown in figure 14 as functions of $\Delta\alpha$ for both the TOUS and the conventional CW spectrometer. The TOUS was operated at an RF level

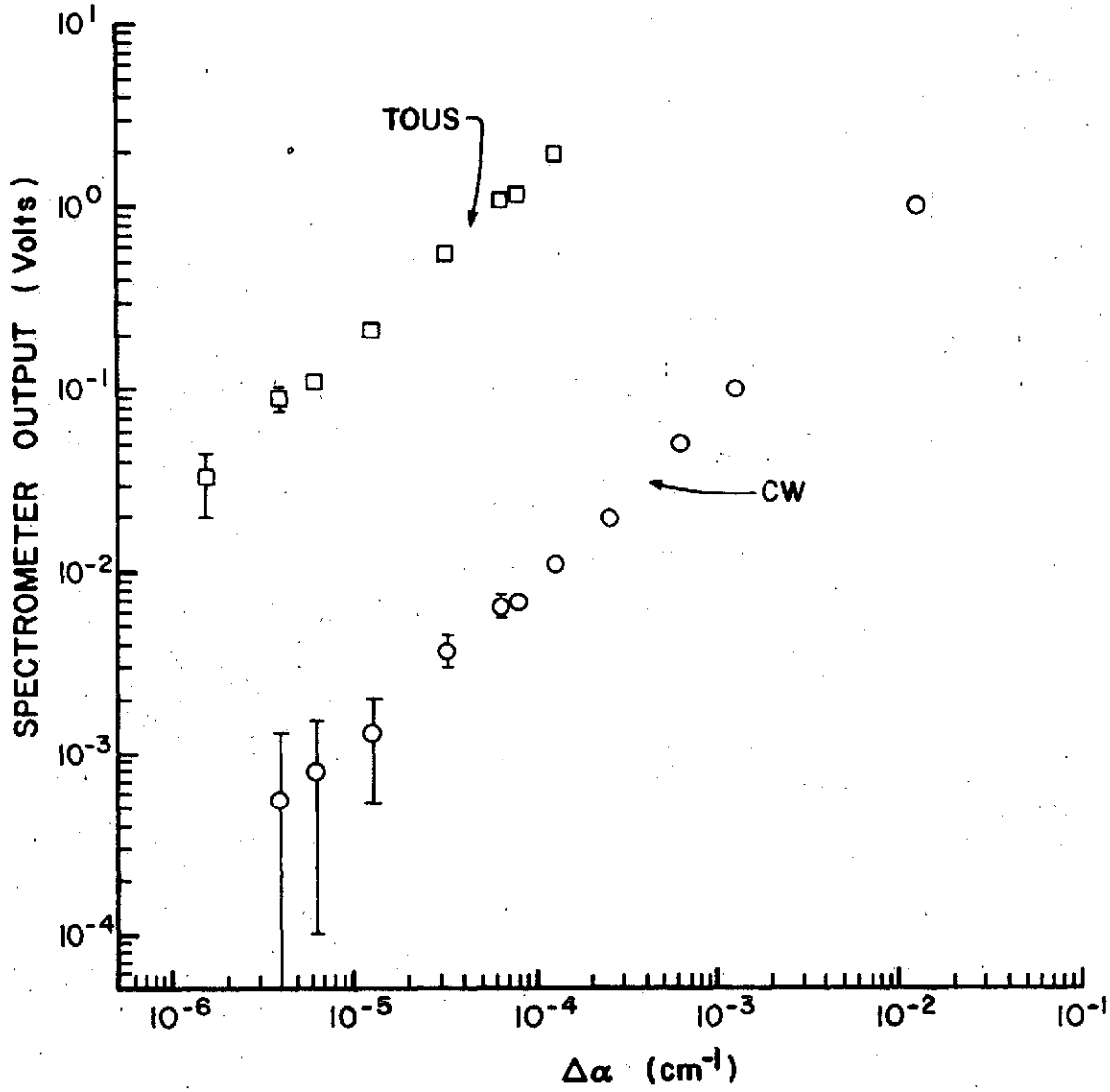

Figure 14) Output voltages of a TOUS and a more conventional transmission cw spectrometer as functions of the change in ultrasonic attenuation $\Delta\alpha$. The error bars represent the noise present in the spectrometer outputs.

corresponding to its optimum signal to noise. The CW spectrometer was operated with the output of the RF oscillator adjusted to produce the same voltage on the transducers as in the case of the TOUS. The audio output of the TOUS is two orders of magnitude larger than that of the conventional CW spectrometer for the same value of $\Delta\alpha$ due to the marginal operation of the TOUS. Of interest, however, are not the relative magnitudes of the spectrometer outputs, but rather their relative signal-to-noise ratios. From figure 14, the signal-to-noise ratio for the TOUS is seen to be substantially better than that for this CW transmission spectrometer.

Details of the signal processing system used with the TOUS as well as the appropriate operating procedures depend upon the particular application. Since the phase shift around the loop must remain zero for stable oscillation, the TOUS automatically tracks ultrasonic dispersion within the bandpass limits of the tuning network. This dispersion is exhibited as a shift in the acoustic mechanical resonance frequency and hence the oscillator frequency. Thus, for physical acoustics measurements, the TOUS provides detailed information about changes in both attenuation and phase velocity while taking maximum advantage of sensitivity enhancement factors.[3,17]

The high sensitivity of the TOUS is best achieved in cases where the small changes in acoustic attenuation of interest occur with characteristic frequencies in the audio range. An example is that of the small changes in acoustic attenuation produced by the presence of particulate or gaseous impurities in flowing fluids. Several applications of the TOUS have already been developed and will be discussed in Section II-4.

II-3. RF AMPLITUDE REGULATOR AND ITS OPERATION WITH THE TOUS

In this section an RF amplitude regulator is described which may be used with the TOUS (see section II-2) or any other RF system which requires a constant RF amplitude level. An electronic schematic of the regulator is presented along with a description of its use. Test data obtained with the regulator show that the regulator reduces spurious amplitude modulations by a factor of 100. Two configurations of the TOUS designed with an RF amplitude regulator are presented along with detailed schematics of the TOUS-regulator system.

Although the TOUS, as described in section II-2, is a useful instrument, a further refinement was necessary to make it something other than purely a laboratory device. A method was developed that keeps the TOUS at an operating point which can be described as truly marginal. The method developed for this purpose is an RF amplitude regulator having many applications other than the TOUS. In fact, the amplitude regulator appears to be useful in areas other than ultrasonics. Basically, the regulator maintains a low noise, constant RF level for any application (e.g., ultrasonics, electromagnetic radiation).

The amplitude regulator together with the TOUS is similar in concept to the marginal oscillator known as the Pound box[28] in that the saturation characteristics of the amplifier determine the output oscillation level. With the TOUS regulator, however, any operating point can be set that satisfies the criteria of the gain-loss product and the closed loop phase.

An electronic schematic diagram of the regulator is shown in figure 15. This particular embodiment of the regulator is built for use with double balanced mixer-modulators which require overdrive protection

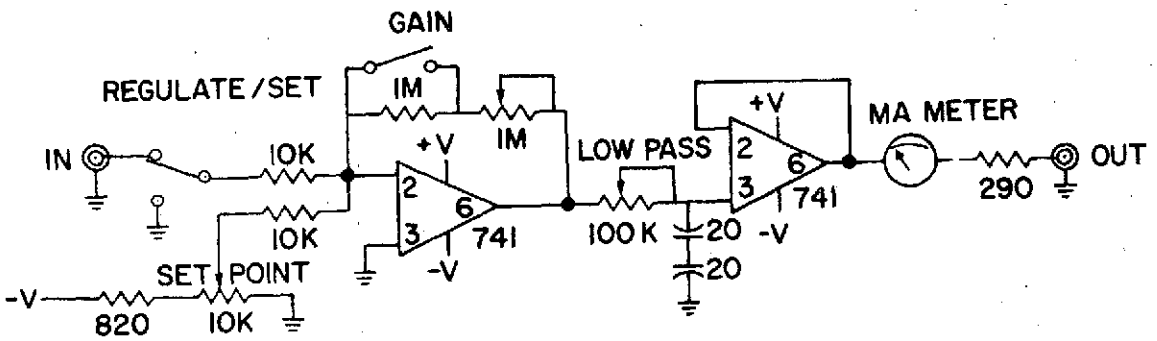

Figure 15) Schematic diagram of the RF amplitude regulator: First stage gain is lowered to 50 for TOUS operation.

from excessive currents. The first amplifier in the regulator (741) is a basic summing circuit with variable gain (0-200). The second amplifier (741) is a voltage follower to buffer the output of the first stage and provide a low pass filter (RC time constant 0-1 second). In the set mode, the current out of the regulator is controlled by a 40 turn set point pot. In the regulate mode, the input as well as the set point pot are summed. Any change in the input results in a correction current to the mixer which brings the input to its previous level. In this way, once an operating level has been set, the regulator will "lock" the input to that level.

A test of the characteristics of the regulator, as used with a high quality laboratory oscillator is shown in figure 16. The oscillator output is equally divided at the signal splitter with one leg detected, measured by an offset electrometer, and plotted on a y_1, y_2, t chart recorder. The other leg passes thru a double balanced mixer modulator, is amplified, detected, measured by a microvolt digital voltmeter and an offset electrometer, and recorded on the same y_1, y_2, t chart recorder. The mixer attenuation is controlled by the regulator shown in figure 14. The results of the test setup in figure 16 are presented in figure 17. In the bottom trace of the figure is shown the detected RF amplitude output of oscillator. The output level was at about 330 mV with a level stability of about 0.03 dB over the 30 minute test. At the top trace of the figure is the detected RF amplitude output from the regulator. As before, the signal level is about 330 mV with a much improved amplitude stability. In tests run over longer periods of time and with three different lab oscillators, results were similar to these of figure 17.

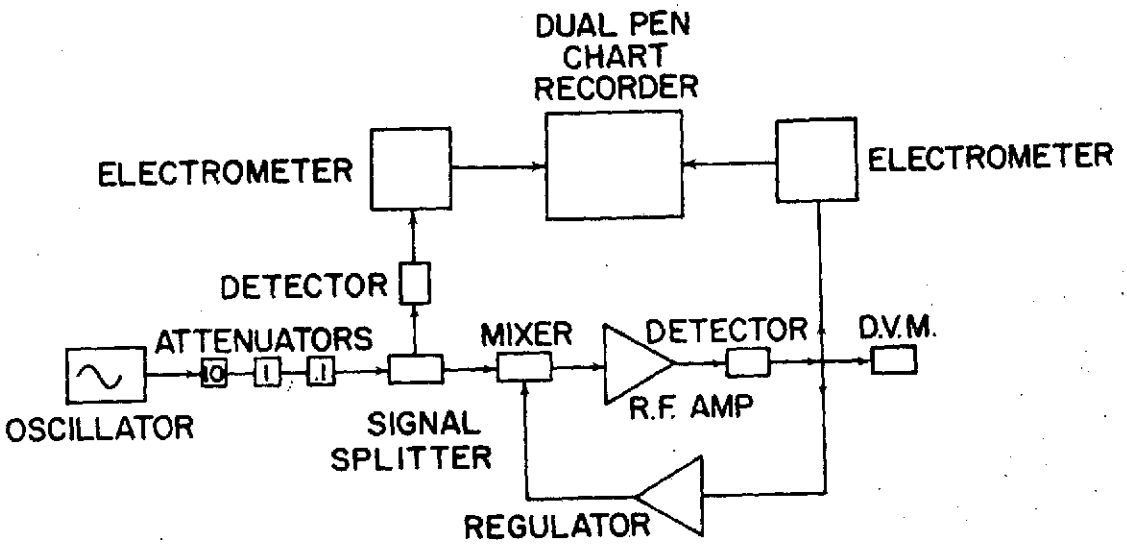

Figure 16) Block diagram of experimental arrangement for evaluation of the amplitude regulator. The results for small amplitude variations in the oscillator output are plotted on a dual pen chart recorder and shown in figure 17. Large variations in amplitude produced by the attenuators are measured with the D.V.M. and shown in figure 18.

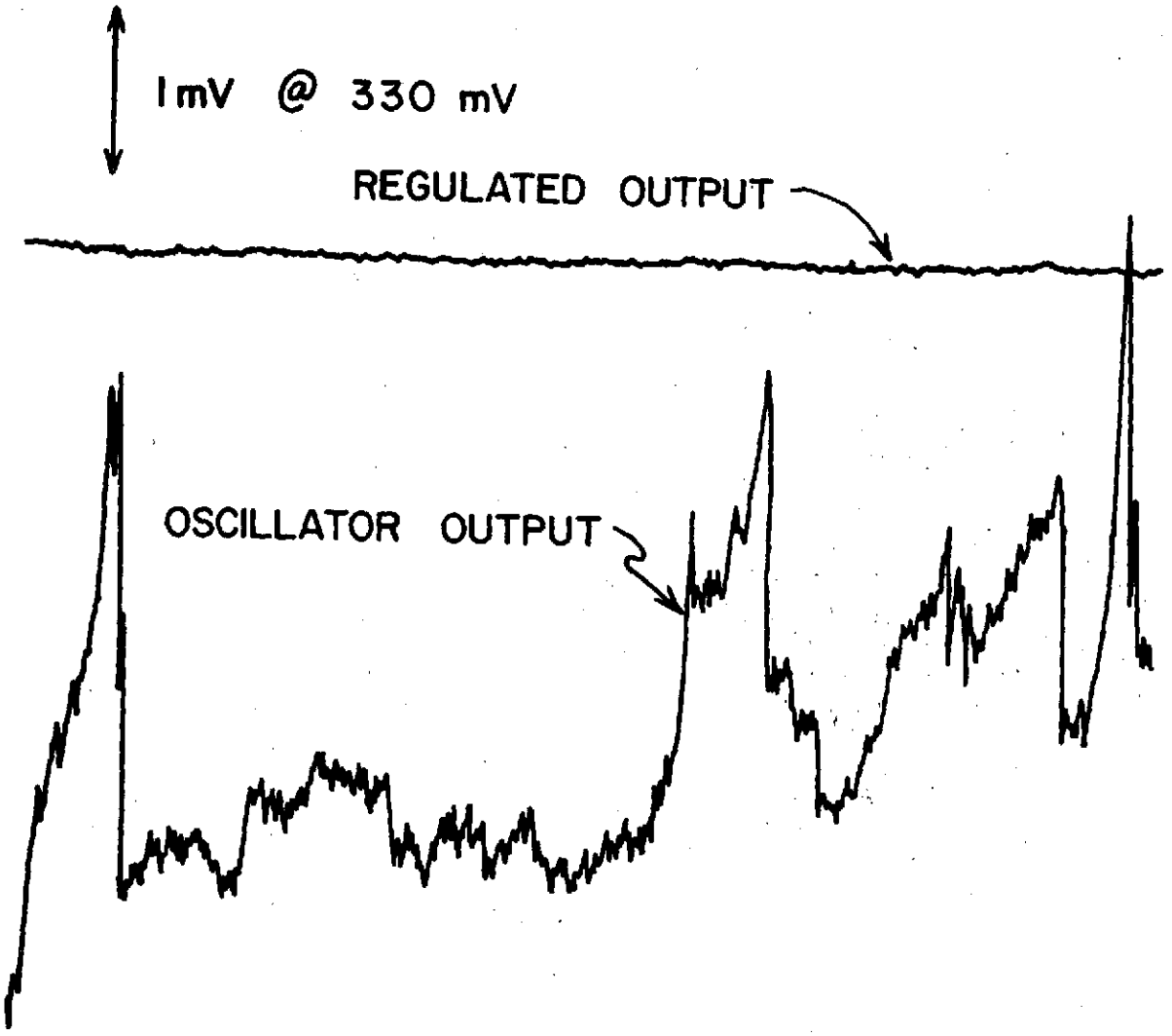

Figure 17) Stabilizing effects of the RF amplitude regulator on the output of a laboratory oscillator. 330 millivolts DC of the signal are bucked out for clarity.

To evaluate the amount of spurious amplitude noise corrected for by the regulator, the attenuators shown in figure 16 were varied. A plot of input to output variation is shown in figure 18. From this figure, the regulator is seen to reduce RF amplitude variations by a factor of 100. In addition, the regulator maintains this stabilization effect over a wide variation of input. In fact, the stabilization is fairly linear over nearly 20 dB change in input level. This type of stability for RF signals is especially useful for experiments in NAR, low temperature measurements, remote sensing or any situation where long term stability is necessary. In particular, the regulator used with a TOUS system can be regarded as an inexpensive yet sensitive ultrasonic system that has good stability and portability.

A slight modification of the TOUS in figure 11 is shown in figure 19(A). In this configuration, the regulator is used with the TOUS as a complete ultrasonic spectrometer. The heavy arrows indicate the RF signal paths while the light arrows indicate audio signal paths. Note that the resonant circuitry illustrated here is for liquid studies and that the tuning network in figure 11 is not used. Although the tuning network does remove some noise that is outside the TOUS operating bandwidth, it does present some problems with liquid flow. For a typical 1-cm. path length brass cavity a temperature shift of $1^{\circ}K$ caused by the liquid produces a cavity length change corresponding to a resonant frequency shift at 10 MHz of 200 Hz. A narrow bandwidth fixed frequency component in the TOUS system prevents it from automatically tracking changes in the resonant frequency. On the other hand, without the tuning network most changes in resonant frequency are followed by the TOUS since as a marginal oscillator, the system tracks the highest Q

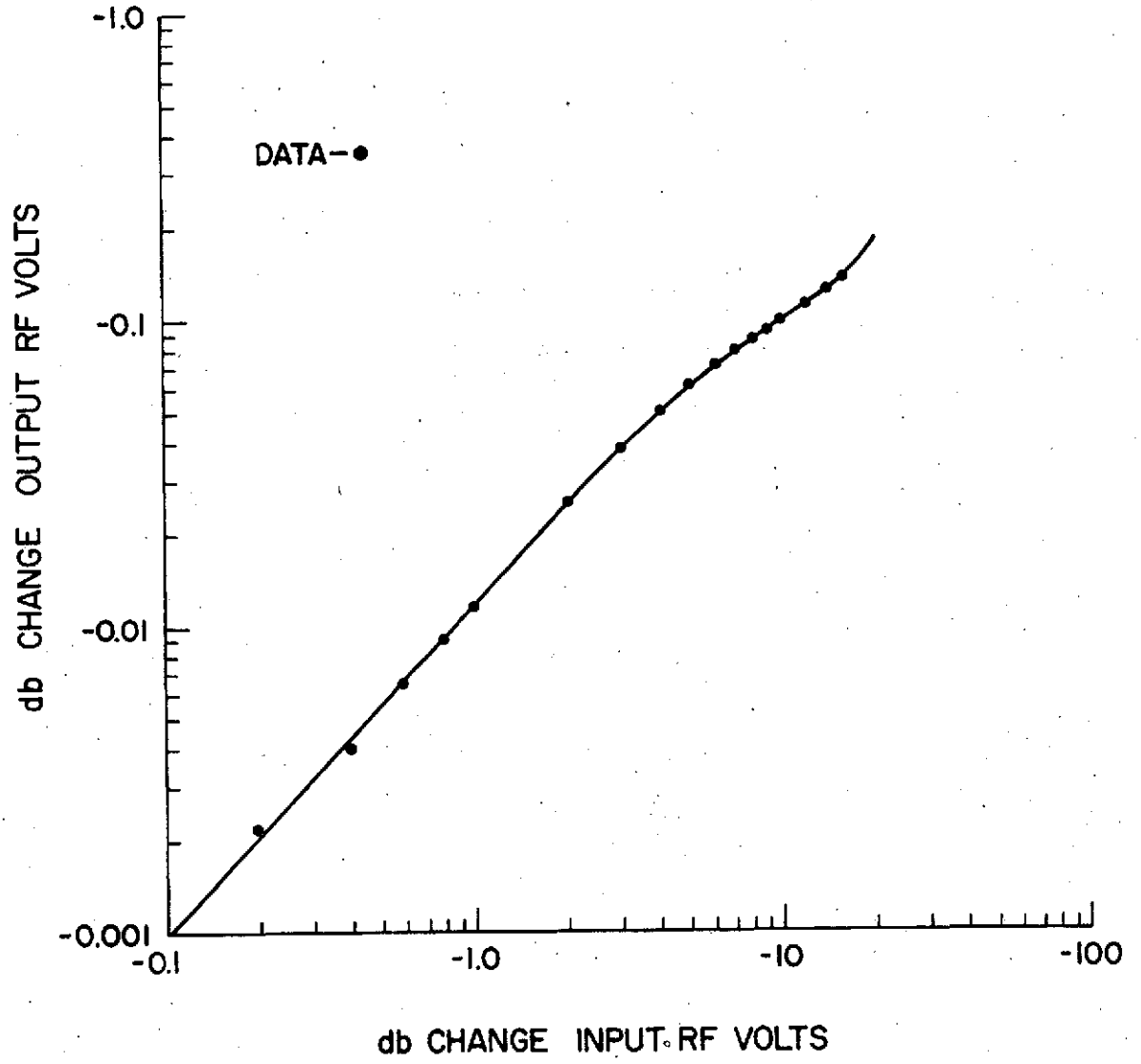

Figure 18) RF amplitude regulator dynamic range and correction linearity. This is indicative of a reduction by two orders of magnitude in spurious amplitude modulation.

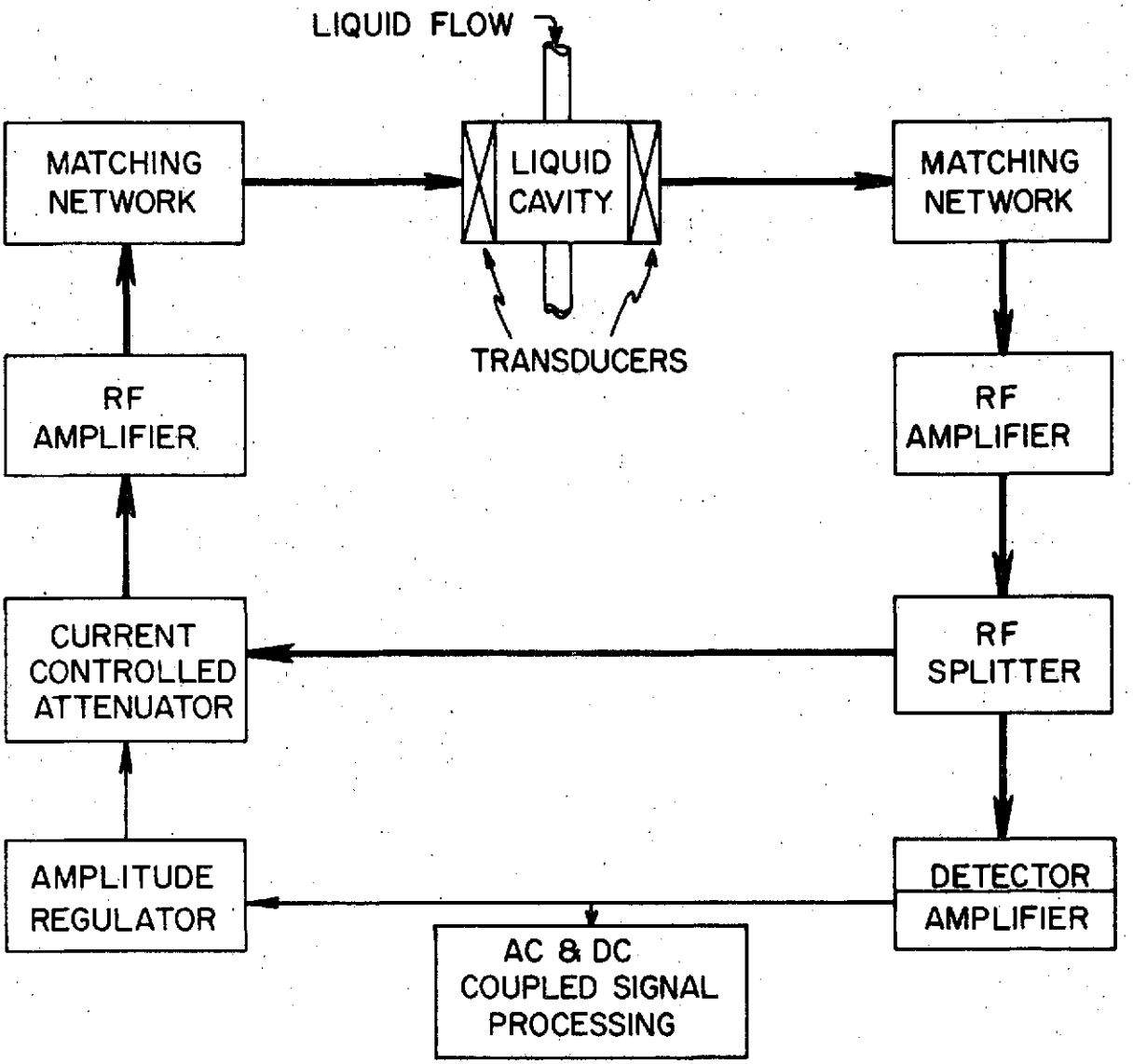

Figure 19A) Block diagram of the TOUS particulate monitor configured with RF amplitude regulation. Particulates or gas in the liquid under study are pumped through the resonant cavity and produce variations in the detected RF signal.

element in the loop. Therefore, the resonant peak is followed so that sensitivity enhancement factors remain constant even though the frequency may drift.

Figure 19(B) is a photograph of the physical components of the block diagram in figure 19(A). The two figures are composed identically so that the labeling in figure 19(A) is compatible with the layout of figure 19(B).

A second configuration of the TOUS has been built specifically for liquid studies. The electronics for this instrument were designed around commercially available integrated circuits. This simplified the overall set-up as is shown in figure 19(C). The major change in this system is the automatic gain control (AGC) section of the RF amplifier shown in figure 19(D). Basically, the AGC takes the place of the current controlled attenuator (mixer-modulator) in figure 19(A). Use of the AGC also modifies the regulator itself, since the AGC requires a non-inverting signal while the mixer requires an inverting signal (an increase in the voltage to the AGC decreases the amplifier gain while an increase in the current to the mixer decreases loop insertion loss). The regulator (figure 19(E)) built for the AGC amplifier contains the RF signal splitter as well as a times 4 RF detector in addition to the convenient Hi-Z RF out and the Hi-Z detected signal out.

A subtle difference between the regulators of figures 15 and 19(E), is the position of the summing junction (the 10K resistors at pin 2 of the 741 amplifier). Locating the junction after the gain stage permits one to change the gain without changing the set point voltage thereby making the two controls more independent. This is desirable for operation of the TOUS at its normal low RF levels. For high RF levels

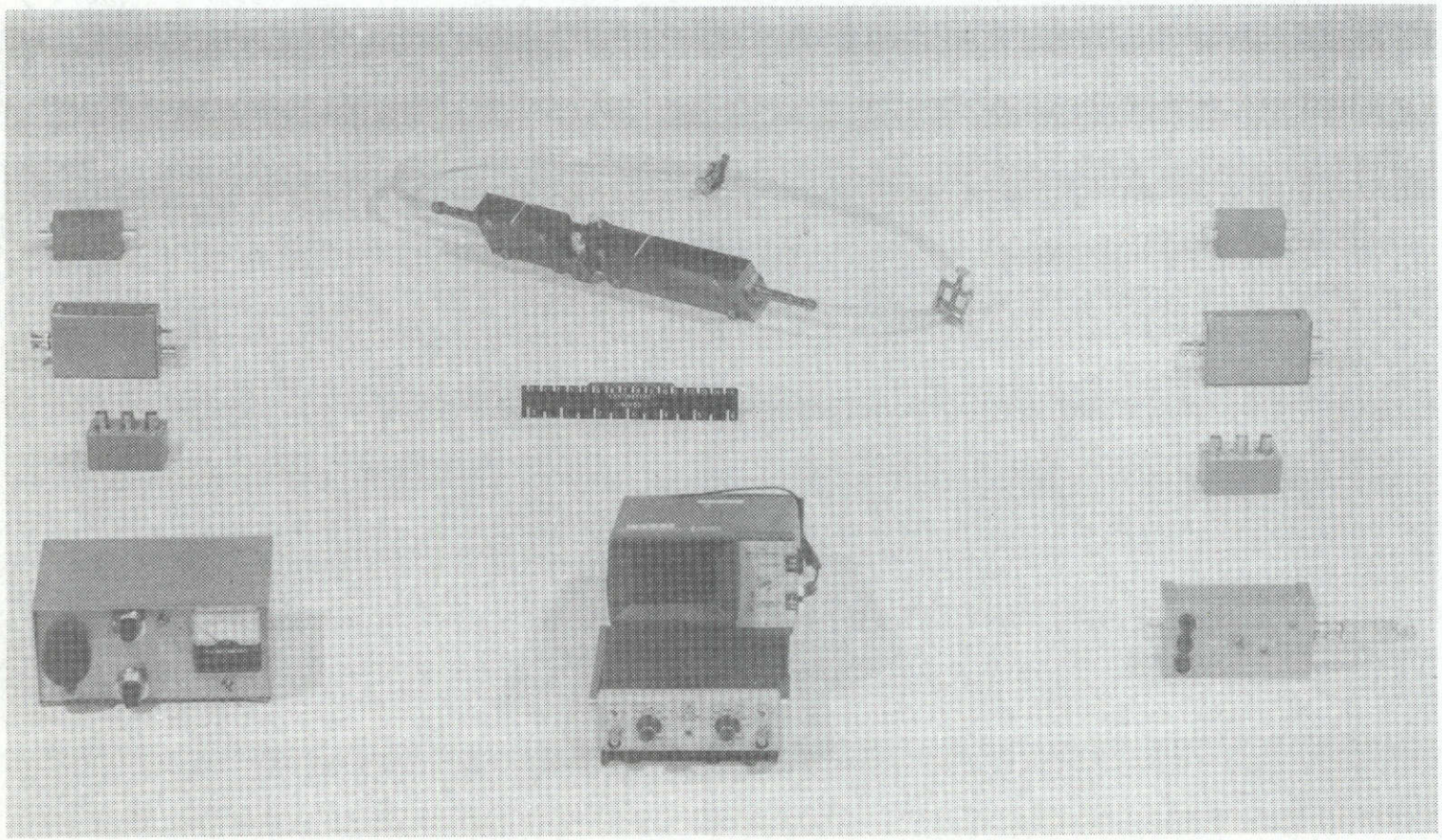

Figure 19B) Photograph of the constant cross section resonant cavity with related electronics for TOUS operation. The individual components in this picture are labeled in the block diagram in figure 19(A).

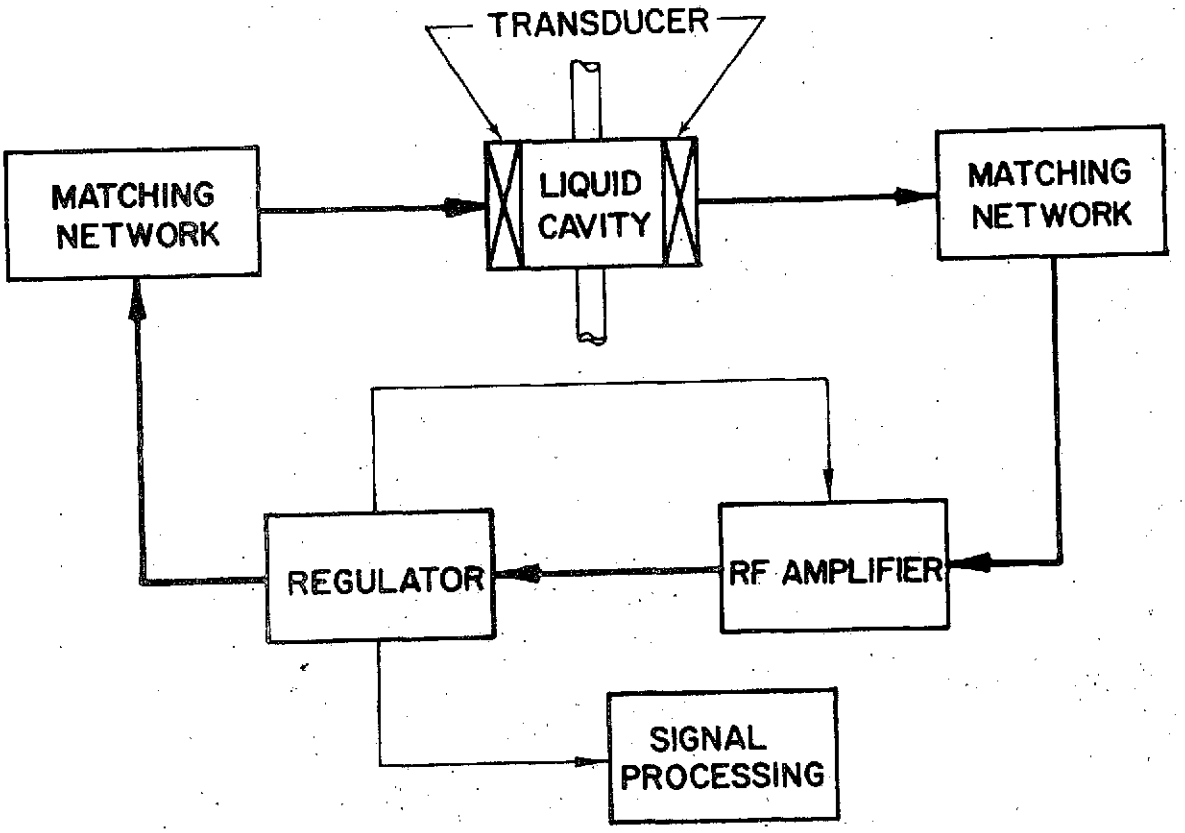

Figure 19C) Block diagram of the TOUS system designed for studies of liquids. Use of commercially available integrated circuits simplified the organization of the instrument to an automatic gain controlled RF amplifier and an RF amplitude regulator.

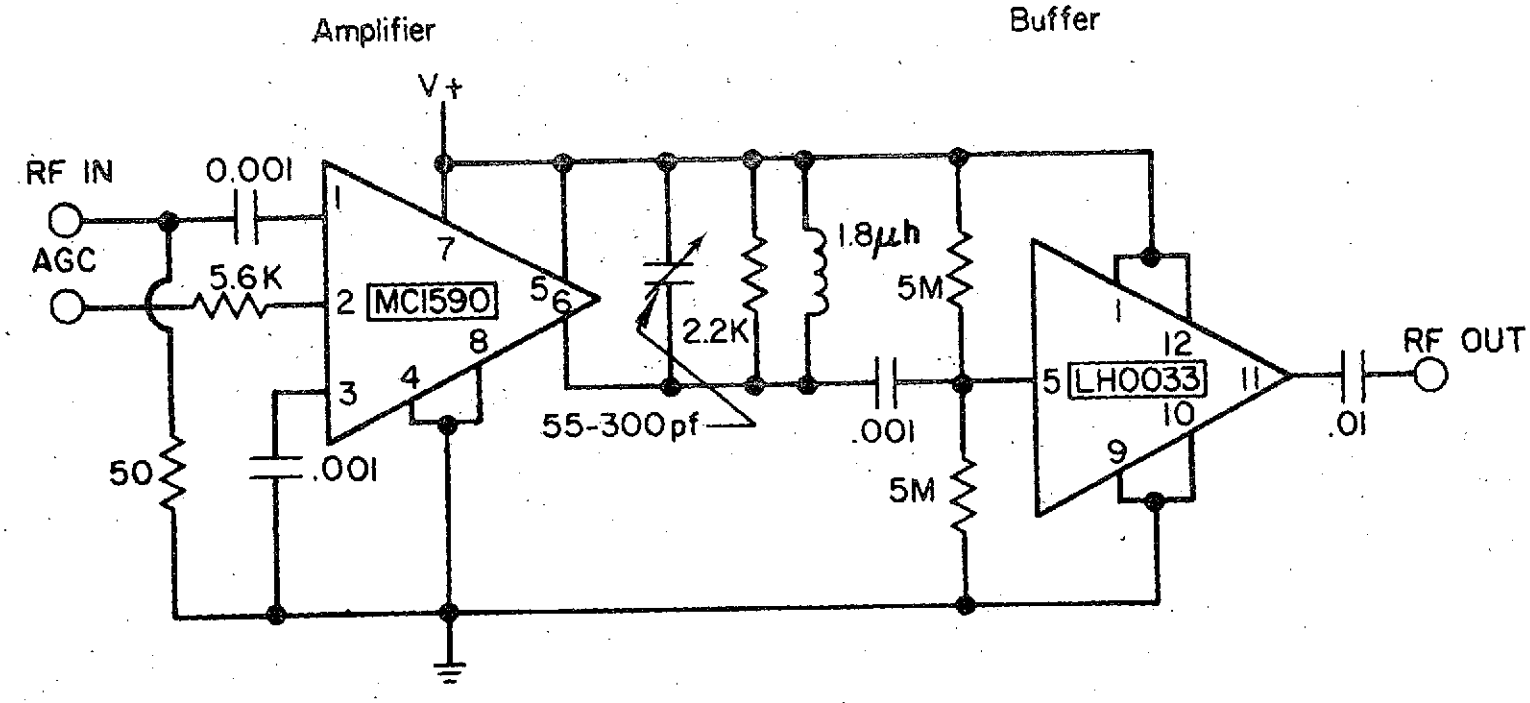

Figure 19D) Schematic diagram of the automatic gain controlled RF amplifier. Center frequency is about 11MHz.

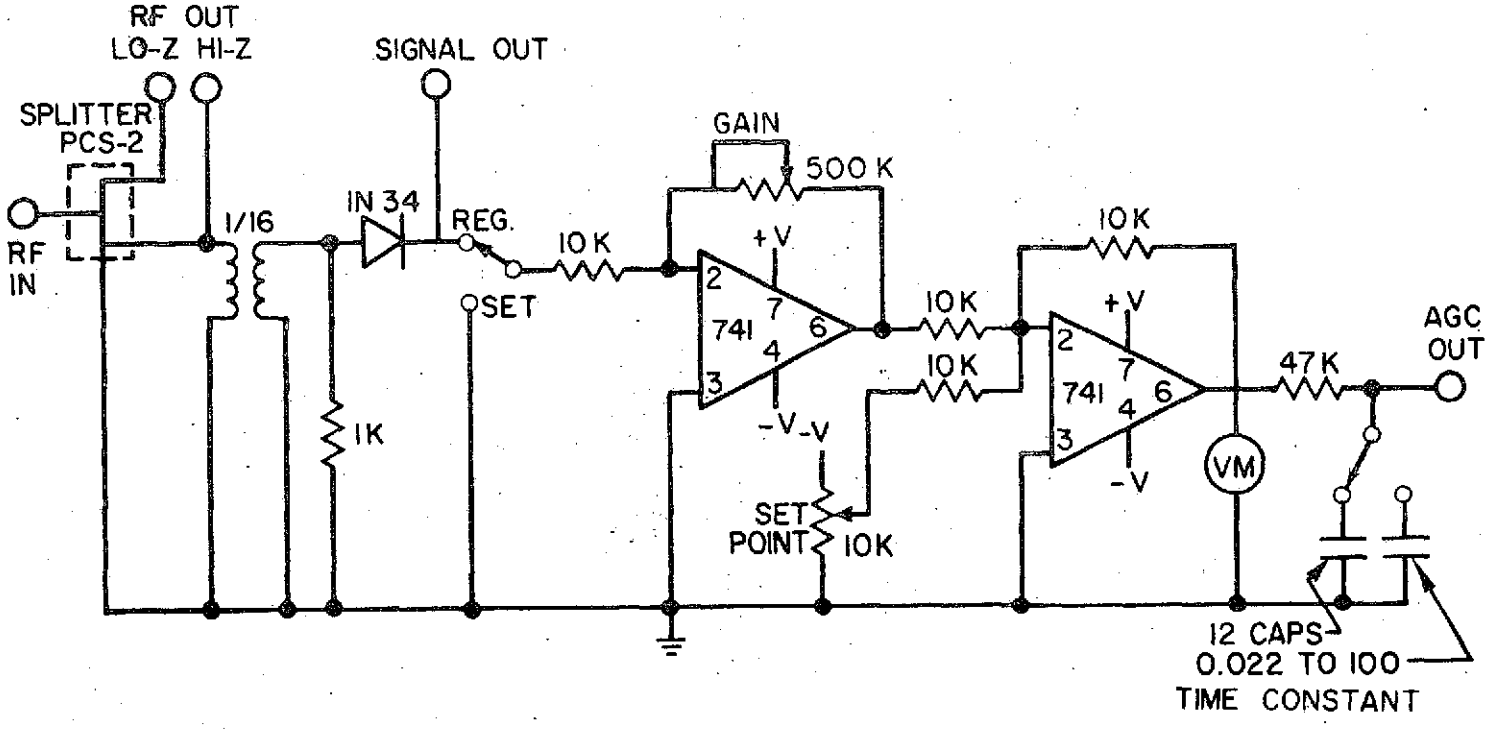

Figure 19E) Schematic diagram of the RF amplitude regulator used with the automatic gain controlled RF amplifier.

such as might be used in CW ultrasonics, the summing junction must be located before the gain stage to buck out the higher detected RF voltages.

II-4. CONTINUOUS WAVE ULTRASONIC PARTICULATE MONITOR

The characteristics of the TOUS-regulator system described in section II-3 have led to an application of the system as a monitor of particulates in flowing fluids. In this section, such an application is discussed and areas of its future use are indicated. Specific design details of resonant cavities for fluid flow measurements are presented along with experimental data of a cavity ultrasonic resonance. In addition, data are presented of calibration runs of the particulate monitor with 400 micrometer contaminents added to the test fluid. Further refinement of the system as a medical monitor is described which resulted in the construction of a microemboli monitor for use in heart-lung bypass surgery. Data obtained during animal surgery is presented to show the effectiveness of the device in monitoring an injection of an anticoagulant.

Several resonant cavities were built and investigated for use with the particulate monitor. Figure 20(A) shows a liquid flow cavity with variable parallelism. The three knurled screws adjust the parallelism of a quartz disk with respect to a fixed quartz disk on the back of the cavity. The internal disks can be seen in figure 20(B) which also shows the seating "O" ring for liquid tight seal. 10 MHz transducers bonded to the outside of the quartz disks provide the ultrasonic excitation for the cavity. By using optically flat and parallel disks, effects due to transducer non-parallelism can be evaluated with little perturbation due to the disks. Qualitative results obtained with this cavity indicated that a fixed parallelism resonator is desirable. First, the "O" rings used for a liquid seal relax overnight thereby

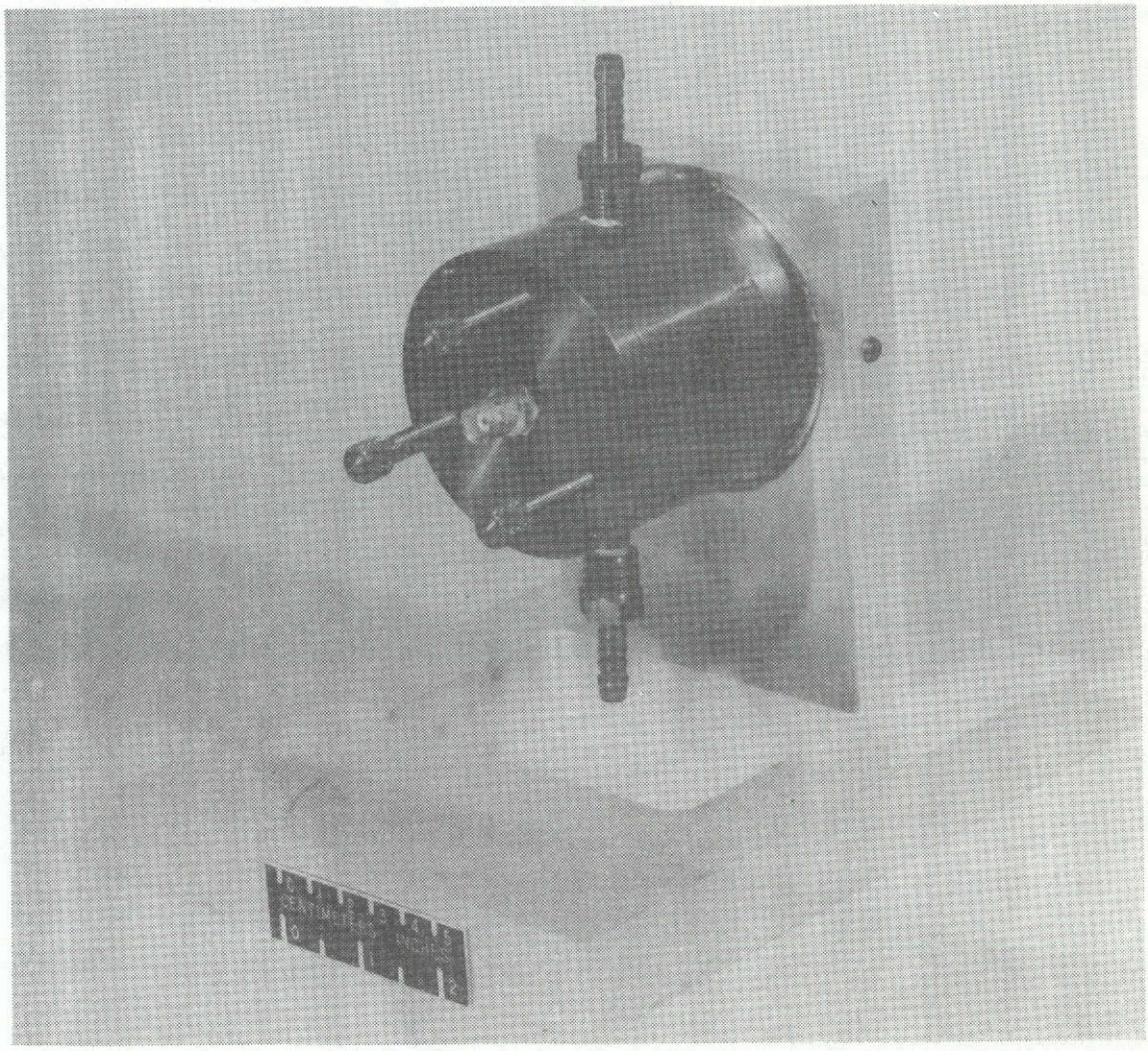

Figure 20A) Photograph of a variable parallelism resonant cavity. The parallelism of 2 internal quartz plates is controlled with the external knurled screws.

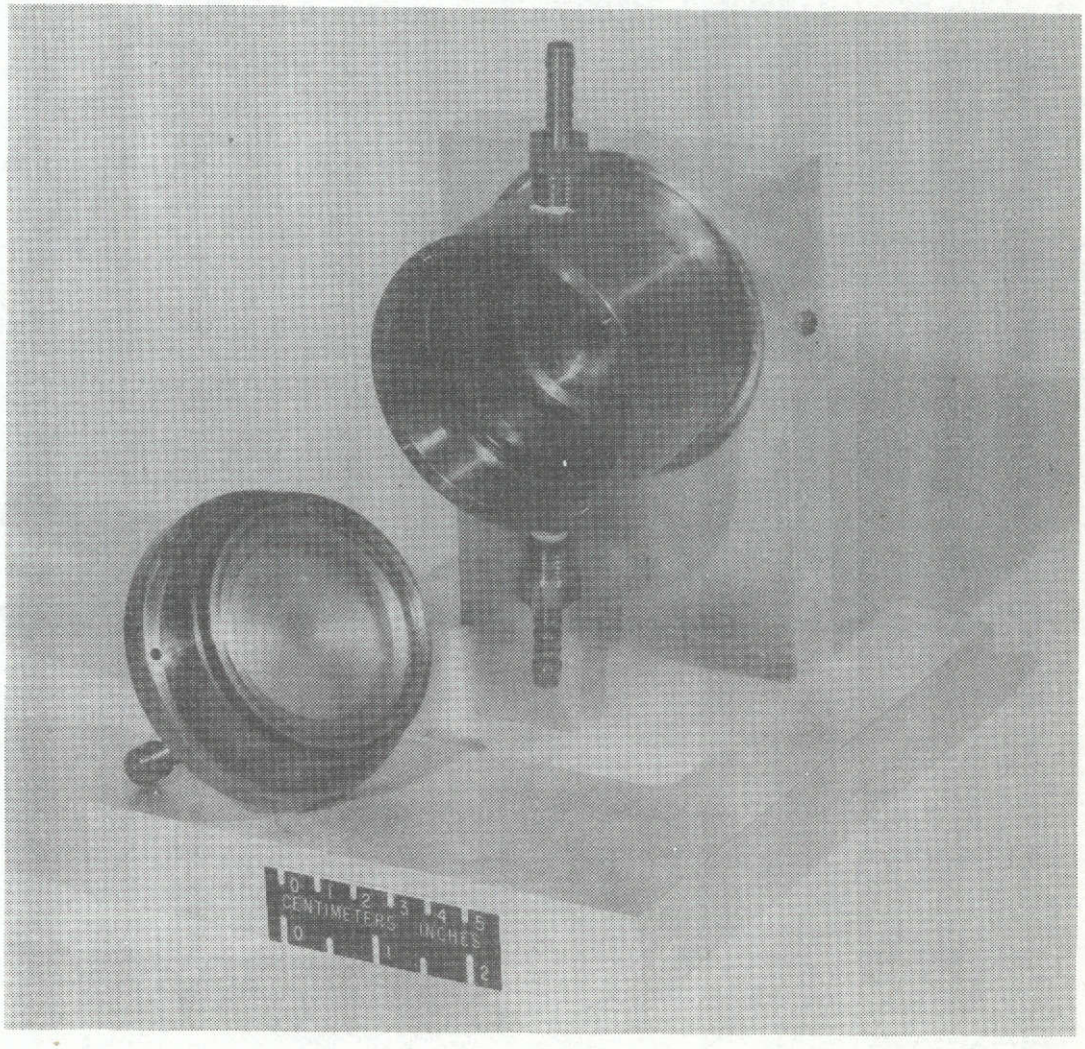

Figure 20B) Inside of the variable parallelism cavity showing the 2 quartz plates and the "O" ring for liquid seal.

requiring frequent "peaking up" to maintain parallelism. Secondly, variations in pressure due to pump pulses seemed to produce a "noisier" signal with this cavity than any other tested. This has been attributed to the compressibility of the "O" rings.

Several other cavity designs have been tried with the most recent shown disassembled in figure 21. This design provides constant cross sectional area from the round tubing connectors through the rectangular flow path. The tubing connectors have a gradual ($<5^{o}$) geometric variation from round to rectangular while maintaining a constant cross sectional area. These coupling pieces were a problem to fabricate. Eventually, a complementary structure was made of graphite and used as a tool to spark cut the transition piece as close as possible to a constant cross sectional area. The cavity is shown assembled in figure 19(B), along with typical electronics necessary to operate it as a particulate monitor. In figure 22 is a sampled CW decay of this cavity with about 15 steps visible in the ultrasonic decay. This verifies that the parallelism tolerances for this assembly are better than $\lambda/10$(15 micrometers).

A closed-loop water flow system was used to test the particulate monitor. Glass microspheres (100-400 micrometers in diameter) were individually dropped into the flow system. Particles smaller than 100 micrometers (Al_2O_3 irregular shapes) were easily measured with a signal to noise better than 15 to 1. In a second test, after the liquid cavity had been cleaned and filled with distilled, filtered (<60 micrometer size particles were removed) water, one 400 micrometer particle was added to the system. The particle was counted by the monitor in the closed loop system for 10 minutes. A similar procedure was followed

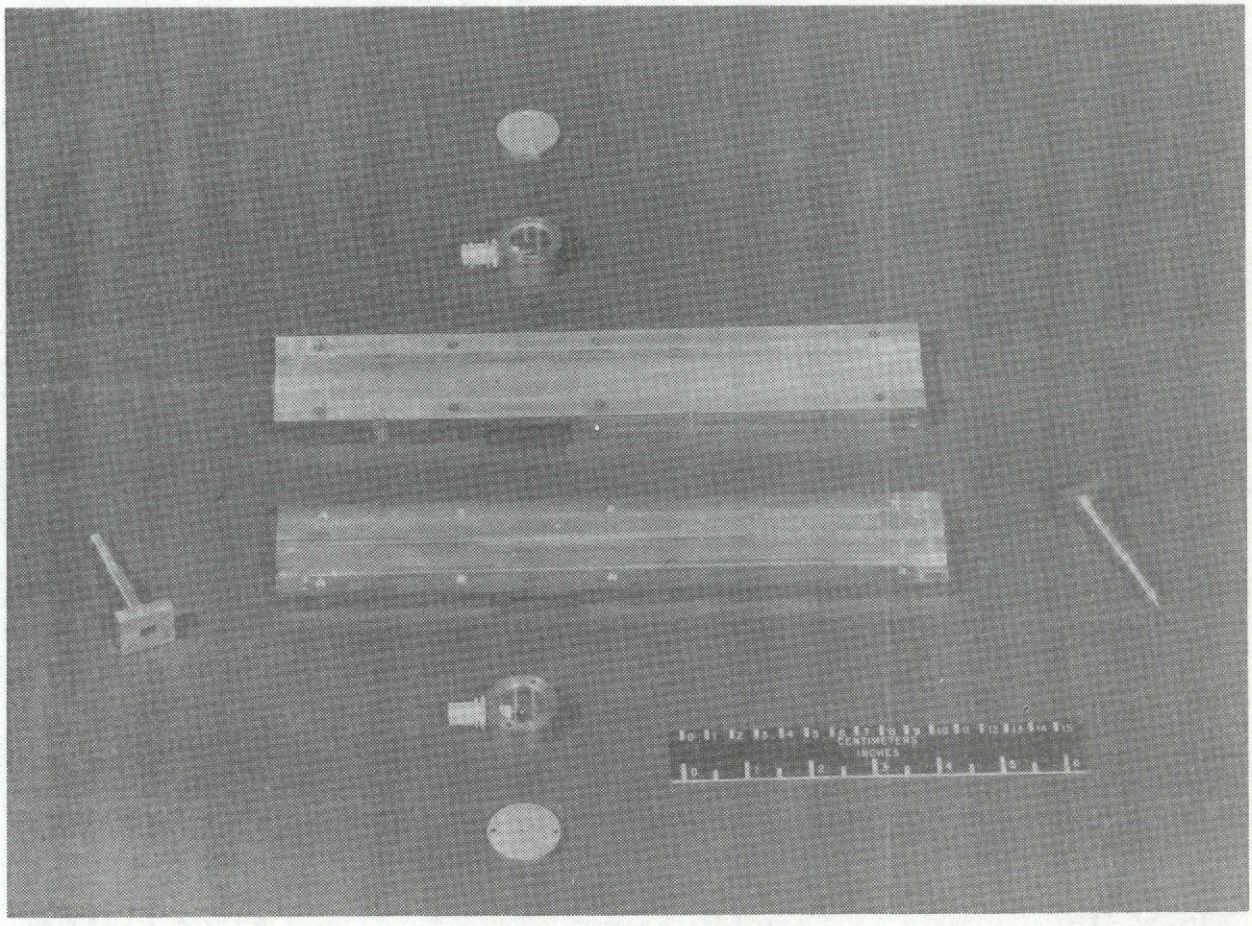

Figure 21) Constant cross section resonant cavity shown disassembled. The end transition tubes are constant cross section with round inlet and rectangular outlet shapes. This reduces flow turbulence in the cavity.

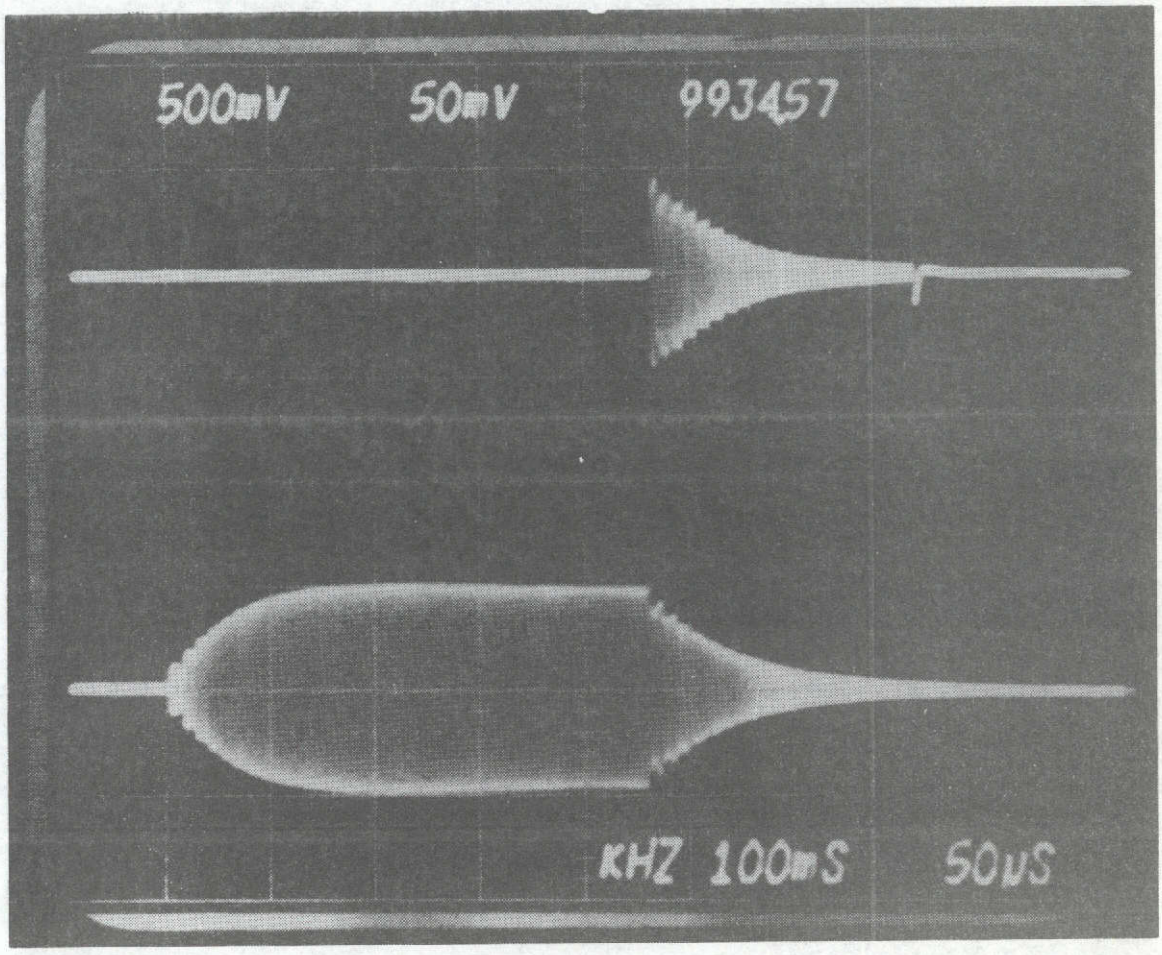

Figure 22) Reflection Sampled CW (top trace) and transmission sampled CW (bottom trace) wave shapes for the water filled constant cross section cavity in figure 21. The stepwise build up and decay of the resonance shown here indicates a cavity parallelism of better than $\lambda/10$.

until 30 particles had been added and counted for periods of time ranging from 5-10 minutes. The results of this test are shown in figure 23 along with the standard deviation of the measurements. The active water volume of the flow system is about 90 ml while the count rate average corresponds to 85 ml/count which is excellent agreement. These results and figure 23 indicate that the monitor is quite linear as well as being accurate.

Specific applications of the monitor are suggested by the results of these tests. One use of the particulate monitor is as a medical instrument.[1,29] Reports of brain damage resulting from extracorporeal perfusion during open heart surgery have led to substantial interest in ultrasonic microemboli detection. Previously reported devices have relied on pulsed ultrasonic techniques.[30] Our instrument, a Continuous Wave Ultrasonic Microemboli Monitor, offers features of non-invasive continuous monitoring of the total volume of blood with high sensitivity and yet takes the form of a compact, inexpensive instrument. The instrument uses a 10 MHz stainless steel resonator probe shown disassembled in figure 24. The probe is designed so that the transducers are in contact with the blood flow itself. Since 10 MHz transducers are too thin to maintain their flatness under pressure, 2 MHz transducers are used operating at their 5th harmonic. The probe is small, easily sterilized and integrates well with the heart-lung medical equipment.

The basic monitor uses similar electronics shown in block diagram figure 19(C). The output of the signal processor consists of pulses with amplitudes proportional to the cross-sectional areas of the micro-

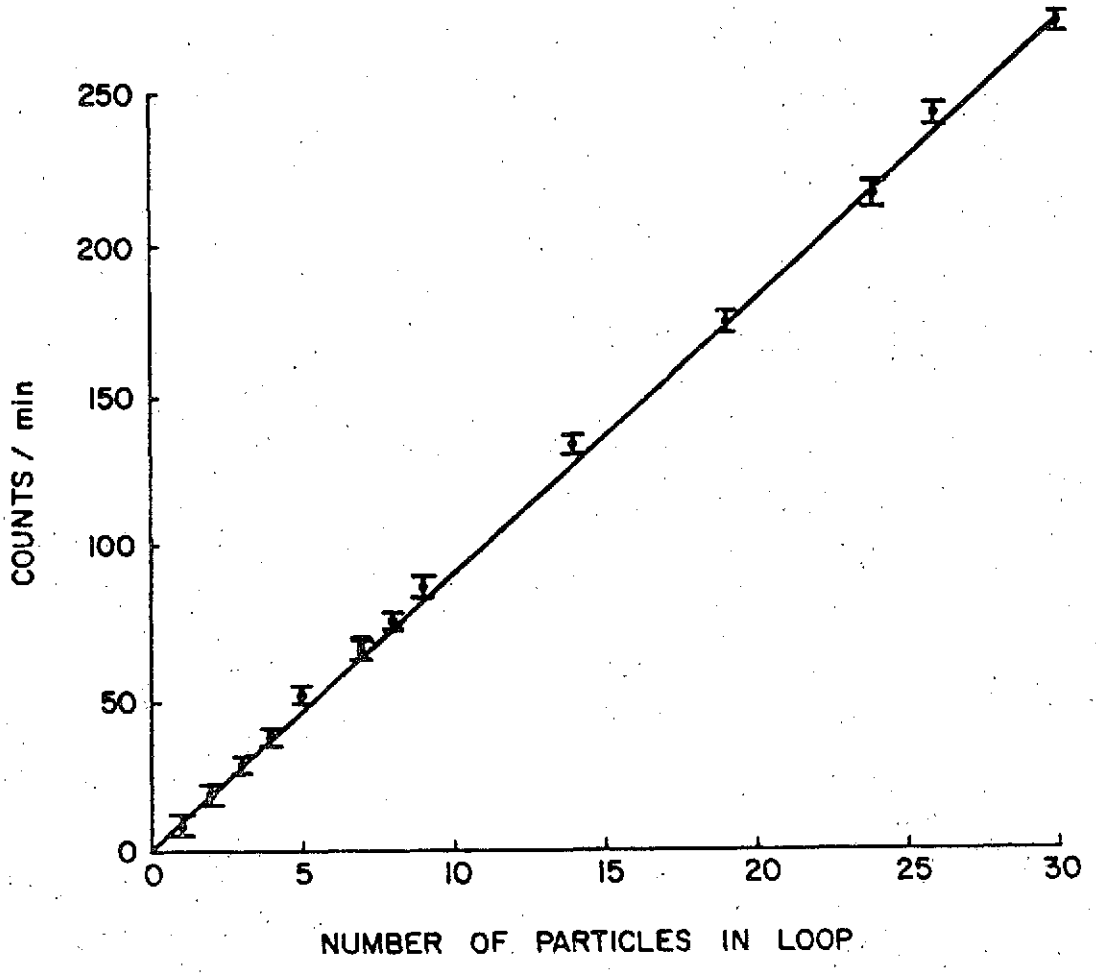

Figure 23) Output of the particulate monitor as a function of the number of 400 micrometer glass spheres in a closed circulatory loop.

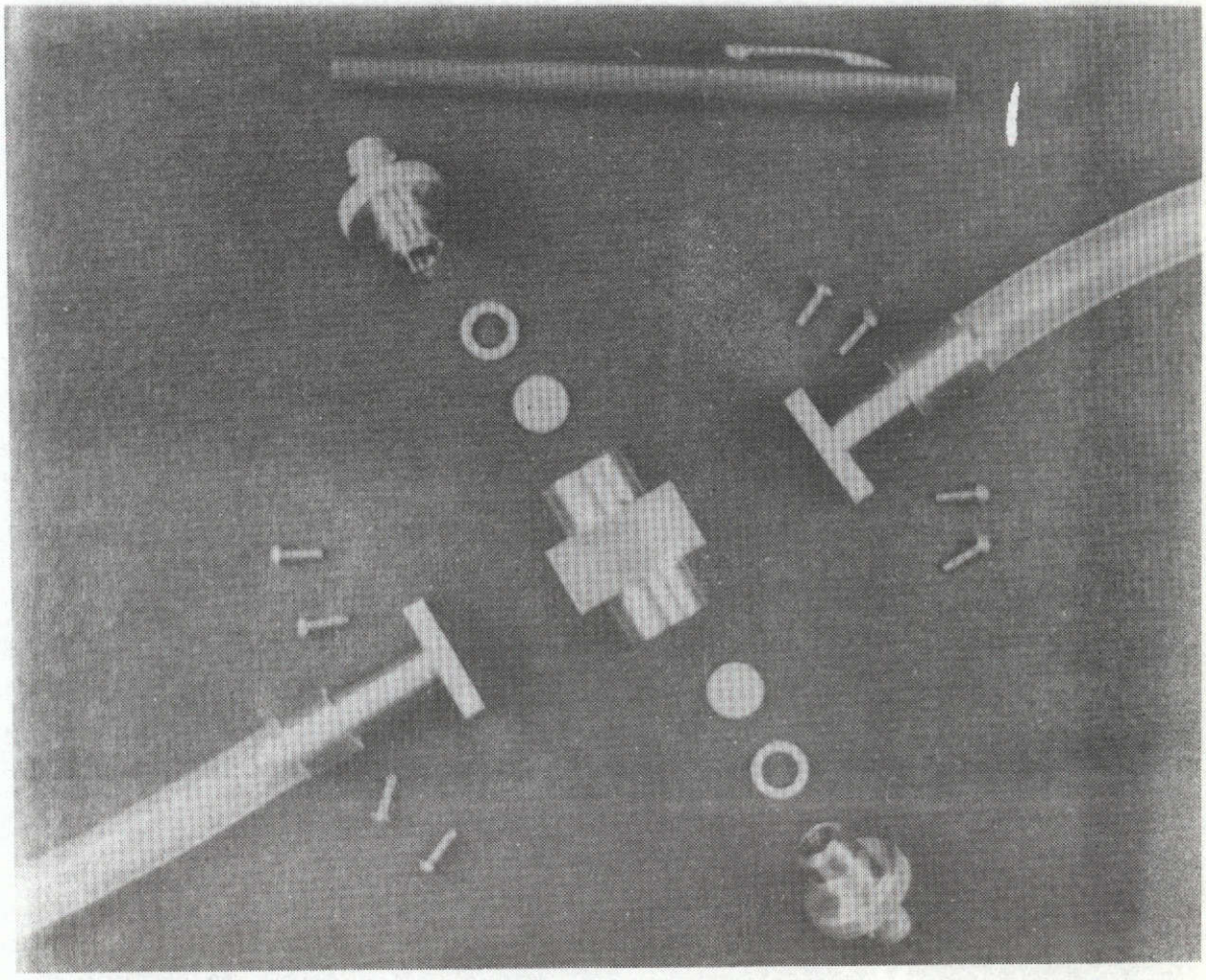

Figure 24) Medical resonator probe used with the TOUS system as a microemboli monitor. Blood circulated extracorporeally during heart-lung bypass operations is monitored ultrasonically while pumped through the probe. The presence of gas bubbles or solid particulates modulates the ultrasonic field and is measured electronically.

emboli and widths representing the transit time of a microembolus through the resonator. Two typical microemboli events are shown in the oscilloscope trace in figure 25. For routine clinical monitoring, a threshold particle size, e.g. 50 micrometers could be selected by the setting of a discriminator level. The total number of events per minute corresponding to the passage of impurities of size greater than the selected minimum are displayed and recorded. Results obtained during heart-lung bypass on a canine indicate that typical counting rates for a 100 micron discriminator level setting range from fewer than 100 counts per minute under "normal" conditions to thousands of counts per minute within a few minutes after the generation of microemboli.

The use of the instrument to continuously monitor microemboli is shown in figure 26. The number of counts per minute corresponding to particles greater than 100 microns in diameter is plotted as a function of time. The data were obtained from the total body perfusion of a mongrel dog. From a point 100 minutes into the run the counting rate remained reasonably stable in the range of 60 to 80 counts per minute for about 16 minutes. An increase in counting rate began at minute 117 in figure 26. Heparin was added at minute 122. Shortly thereafter, the counting rate began to fall, stabilizing at a low of fewer than 20 counts per minute within 3 minutes of the time that the anticoagulant was added. An attempt has not yet been made to repeate this experiment.

The microemboli monitor has been chosen by Industrial Research magazine as one of the 100 most significant technical products of the

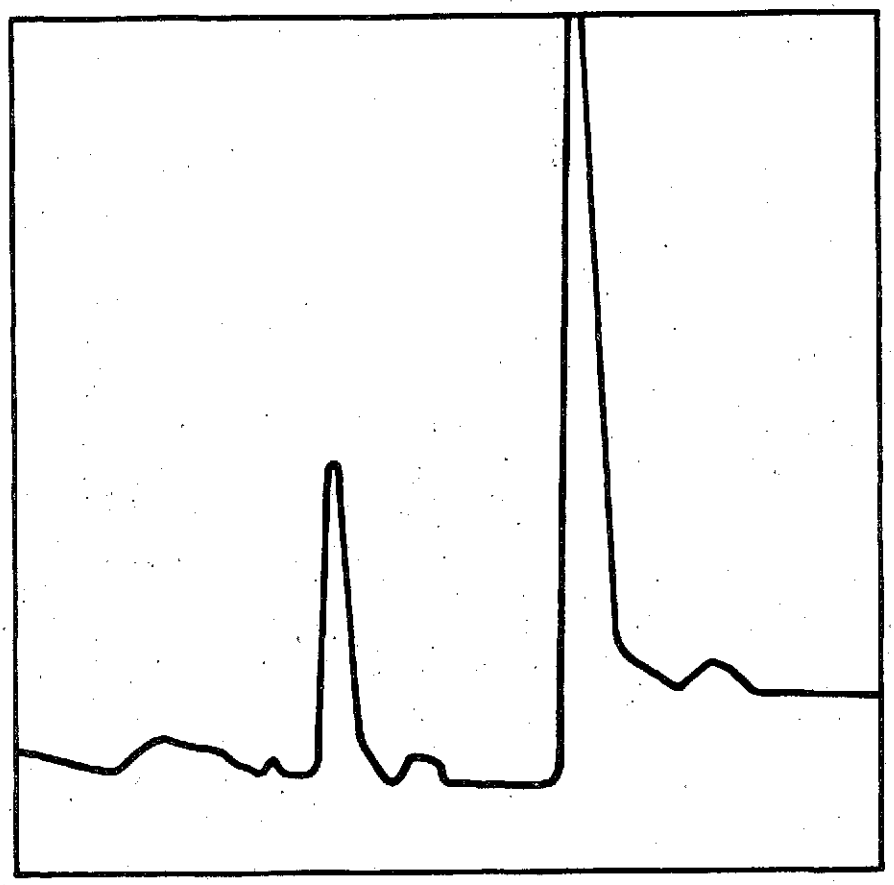

Figure 25) Oscilloscope trace of 2 microemboli events. Microemboli passing thru the resonator decrease its effective Q and therefore decrease the RF amplitude producing the pulses shown. Entire horizontal axis is 100 milliseconds.

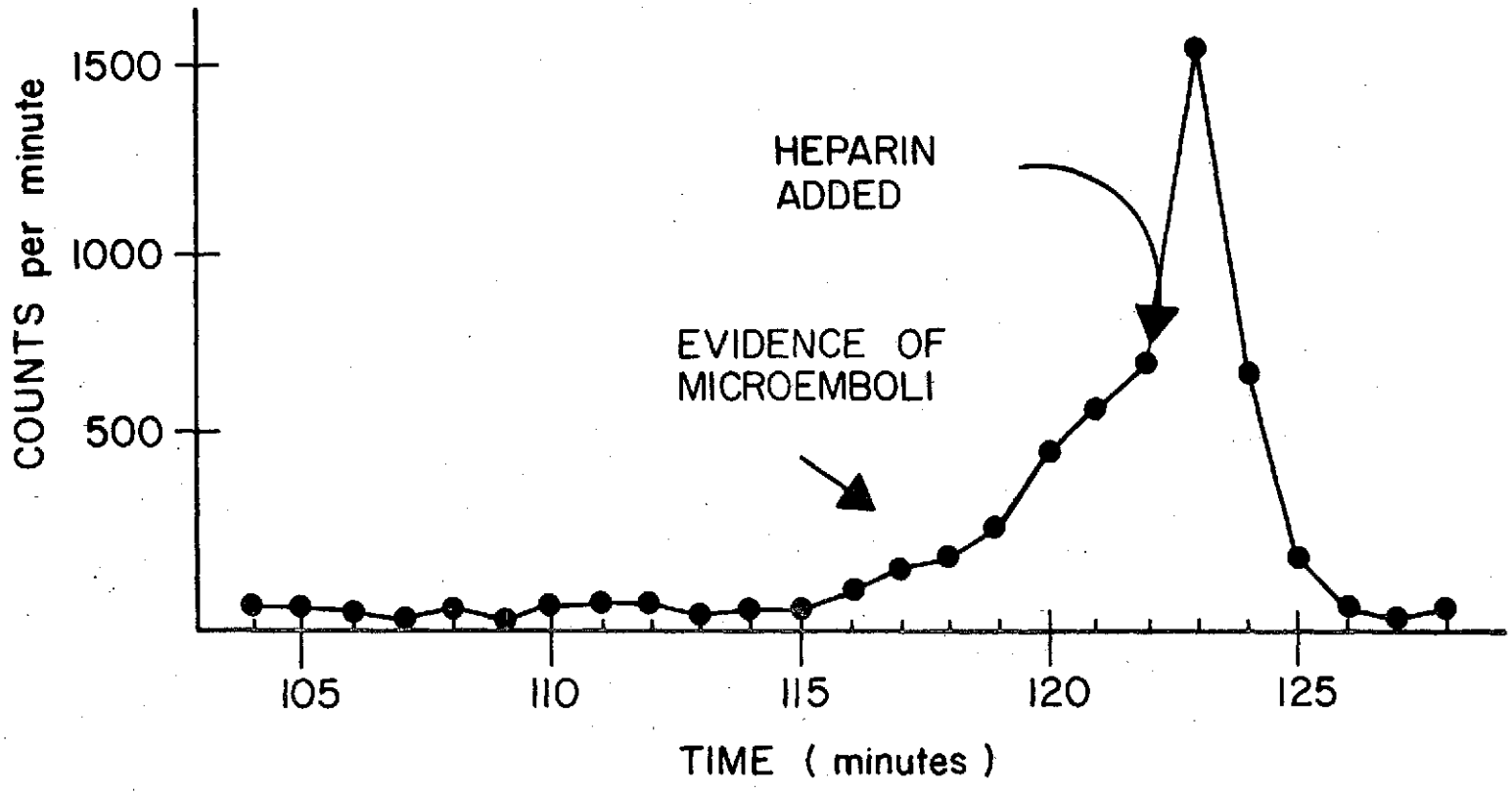

Figure 26) Heparin event as measured by the ultrasonic particulate monitor 120 minutes into animal operation.

year 1974.[1] Since that award, the monitor has been used successfully during an operation on a human. As clinical experience is accumulated, the information generated by the monitor will be evaluated and may prove it to be an important medical instrument. Additional medical applications include monitoring of hemodialysis units as well as blood used for transfusions. In comparison with other published monitors[30] the particulate monitor based on the CW TOUS concept appears to have certain benefits which are indicated in Table 1. Future developments may lead to a more sensitive, less expensive device than indicated.

Another use of the particulate monitor would be as a machinery wear monitor (i.e. aircraft engines, helicopter gearboxes, hydraulic systems). Wear particles transported by the lubricant can be counted and sized by the monitor thereby providing the user with real-time on-line information as to lubricant and machine condition. The real-time information can be especially important in aircraft systems as an alert "signature" of impending catastrophic failure.

III. ULTRASONIC INTERACTIONS IN CdS

III-1. PHONON-CHARGE CARRIER COUPLING IN CdS

In this section, we examine the interaction of ultrasonic waves with charge carriers in CdS. The theory of Hutson and White[9] is utilized in linking ultrasonic absorption and dispersion to conductivity in piezoelectric semiconductors. The theory of reference 9 is verified with measurements of the effects of photogenerated charge carriers on ultrasonic parameters. A tentative explanation presented for small errors in the measured data is the existence of inhomogeneities in the crystal. A hypothetical model with inhomogeneities is developed which predicts results consistent with the observed data.

CdS is a II-VI semiconducting compound of the hexagonal-wurtzite structure. Although it can exist as a cubic zincblend structure, it will revert to the hexagonal structure if heated above 100°C. Single crystal material has a bandgap of 2.5 ev and a corresponding peak in the optical absorption coefficient at 0.5 micrometers.

CdS is also a photoconductor with the conductivity varying nearly linearly with light intensity. The photoconductivity is impurity and defect dominated for optical wavelengths greater than 0.5 micrometers. The impurity dominated conductivity causes a broadening of the photocurrent vs. photon wavelength curve and results in a monotonic decrease in the photocurrent of five orders of magnitude between 0.5 micrometers (2.5 ev) 1.0 micrometers (1.3 ev).

In addition, since the crystal structure of CdS lacks a center of symmetry, it is piezoelectric and has an electromechanical coupling coefficient equal to about 0.03. The piezoelectric property causes

electric fields to accompany ultrasonic stress waves and produces a coupling mechanism between the ultrasonic wave and charge carriers.

Although a good model for the phonon-charge carrier coupling was not fully developed until 1962, experimental observations of the coupling effect were reported in 1959 by Gobrecht and Bartschat[31] and later by Nine[32], Ogawa[33], Hutson[34], and Nine and Truell[35] for CdS. The observations reported that ultrasonic attenuation was a function of light irradiation. In references 34, 35, a correlation between conductivity and ultrasonic attenuation is attributed to an interaction between conduction electrons and stress waves coupled by the piezoelectric effect.

A model of this coupling is developed by Hutson and White in reference 9 with a linear theory that includes effects due to carrier drift, diffusion, and trapping. In this model, the propagating stress wave is accompanied by an electric field produced from the strain on the piezoelectric crystal. The electric field is composed of both longitudinal and transverse components with the transverse wave small and therefore neglected. The longitudinal wave, however, is sufficiently large to produce measurable effects on charge carriers. Conversely, the charge carriers play a role in the crystal's ultrasonic properties resulting in acoustic dispersion and changes in loss.

In reference 9, it is shown that the ultrasonic velocity takes the form:

$$v = v_o \left\{ 1 + \frac{e_2}{2c\epsilon} \left[\frac{1 + \omega^2/\omega_D\omega_C}{2 + \omega^2/\omega_D\omega_C + \omega_D\omega_C/\omega^2} \right] \right. \qquad \text{(III-1)}$$

where: $v_o = (C/\rho)^{1/2}$

c is the elastic constant

ρ is mass density

$\frac{e^2}{2c\varepsilon} \simeq \frac{K^2}{2}$, the electromechanical coupling constant

e is the piezoelectric constant

ε is the dielectric permittivity

ω is the ultrasonic angular frequency

ω_D is the "diffusion frequency" $\simeq \frac{ev^2}{ukT}$, or $v\left(\frac{\tau}{\omega_D}\right)^{1/2} = L_D$

where τ is lifetime and L_D is the diffusion length.

μ is the mobility

ω_c is the "conductivity frequency" = $\frac{\sigma}{\varepsilon}$

σ is the conductivity

For values of $\omega << \omega_D$ ($\omega_D \simeq 3\text{x}10^{10}$ Hz at 300°K for CdS) and $\omega_c << \omega_D$ ($\omega_c = 3\text{x}10^{7}$ Hz for $\sigma = 3\text{x}10^{-5}$ $(\Omega\text{- cm.})^{-1}$ in CdS) this relation becomes:

$$v = v_o \left[1 + \frac{e^2/2c\varepsilon}{1 + \left(\frac{\omega_c}{\omega}\right)^2} \right] \qquad \text{(III-2)}$$

or simply

$$\frac{v_\infty - v}{v_o} = \frac{K^2}{2} \left(\frac{F^2}{1 + F^2} \right) \qquad \text{(III-3)}$$

where $K^2 \cong \frac{e^{2*}}{c\varepsilon}$, the electromechanical coupling coefficient

$$F = \frac{\omega_c}{\omega}$$

$$v_\infty = v_o \left(1 + \frac{K^2}{2} \right),$$

For the attenuation, it is shown that:

$$\alpha = \frac{\omega}{v_o} \frac{K^2}{2} \left\{ \frac{\omega_c/\omega}{1+2(\omega_c/\omega_D)+(\omega/\omega_D)^2+(\omega_c/\omega)^2} \right\} \qquad \text{(III-4)}$$

which for $\omega << \omega_D$ and $\omega_c << \omega_D$ becomes:

$$\alpha = \frac{\omega}{v_o} \frac{K^2}{2} \left(\frac{F}{1+F^2} \right) \qquad \text{(III-5)}$$

An experimental method was devised to verify equations III-3 and III-5. It is necessary to measure ultrasonic attenuation and phase velocity as a function of ω_c. Since a CdS resonator can be fabricated to be photoconductive, its conductivity can be varied with light. Therefore, the conductivity frequency can also be varied with light. Assuming that the conductivity varies linearly with light intensity, a simple accurate method employing neutral density filters can be used to vary ω_c.

---

*The coupling strength parameter κ is approximately equal to the square of the electromechanical coupling coefficient K, since

$$\kappa = K^2/(1 - K^2) = K^2, \text{ where } K^2 << 1.$$

It was convenient to use the ultrasonic calibrator (Section III-2) to verify the Hutson and White theory. The calibrator contains a flat and parallel single crystal of photoconductive CdS. A constant intensity lamp is focused on the resonator through a sequence of neutral density filters. By setting the lamp intensity to a maximum attenuation value (i.e. F = 1 or $\omega_c = \omega$), it was possible to obtain accurate measurements relative to F = 1. The results of this experiment are shown in figure 27 along with a theoretical plot of equation III-3 and III-5. The theoretical plots are drawn for $K^2 = 0.03$ which was determined from a best fit to the data. The agreement between theory and data is seen to be good.

However, examination of figure 27 reveals some lack of agreement between theory and experiment. A tentative explanation for the deviations from theory is based on inhomogeneities in the crystal itself. Since these samples were annealed in sulpher to increase their photoconductivity, one expects cadmium vacancies. If these represent inhomogeneities in the sample, they may account for the observed deviatiations when the phenomona of superlinearity (or supralinearity) is considered[36]. This effect produces a relationship between σ and I such as $\sigma = C_o I^n$, $n>1$. This "sensitizing" results from the addition of doubly charged centers which lengthens the recombination lifetime for holes. Since these holes are close to the valence band, they play no role in conductivity until the hole demarcation level drops below their position due to low temperatures and/or high illumination. The result of the increased hole lifetime is to decrease the recombination rate thereby increasing the conductivity.

C2

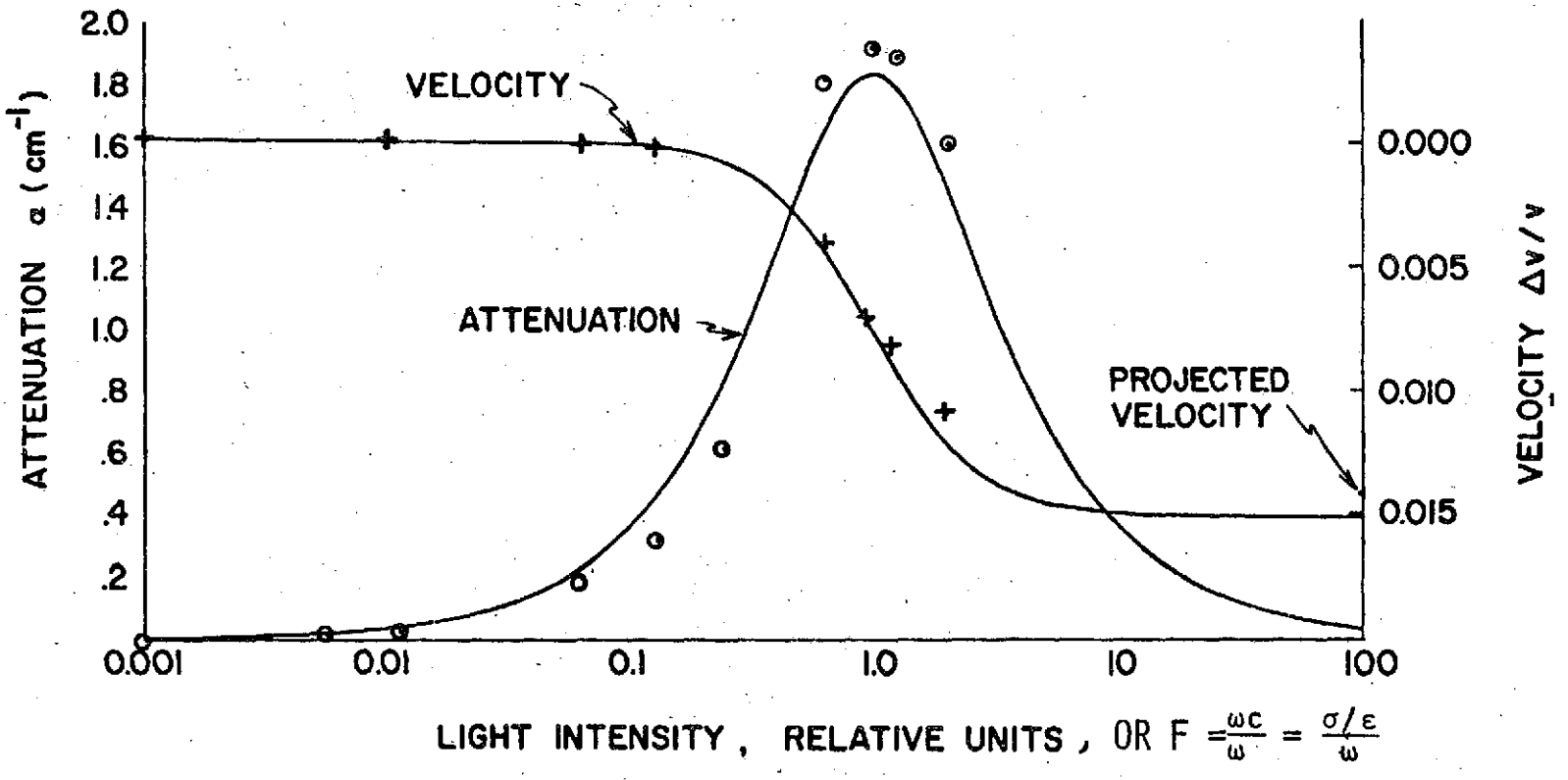

Figure 27) Effect of light on ultrasonic attenuation and velocity in photoconducting CdS. The solid lines are theory for $K^2 = 0.3$. The experimental points were measured at 17 MHz.

A further examination of figure 27 shows that the data "error" for attenuation (7%) is worse than the "error" for velocity (3%) measured at the peak of attenuation (at F = 1).

If there are large inhomogeneities in the density of the doubly charged centers it might explain the observed behavior since the experimental data for dispersion is obtained from a measurement of the frequency at the resonant peak. With inhomogeneities in the crystal, this peak could be shifted from its expected mechanical resonance to one corresponding to a lower conductivity. In addition, the shifting of the position of the mechanical resonance would produce a distorted attenuation vs. light intensity figure.

To examine if superlinearity is a possible explanation for the observed errors, a simple model is evaluated. In this model the resonator is composed of 2 segments: an A un-sensitized half and a B sensitized half. The conductivity in the A half is less than that in the B half. Therefore, for values of $F < 1$, the ultrasonic attenuation for the A half is less than that for the B half. Since the ultrasonic signal is obtained by adding the signals of each half, the combined signal is dominated by the A half. Thus, the resonance peak of the combined signals would be shifted to that corresponding to higher phase velocities found in sample A. Actually, the resonance peak would occur as if the combined samples had a velocity higher than the average of their velocities. This is not the case for attenuation.

The attenuation of the combined samples is nearly the average of the attenuation for each half. A theoretical plot is shown in figure 28(A) of the mechanical resonance for each half and for the combined signals. The effect of an increase in the conductivity is a decrease

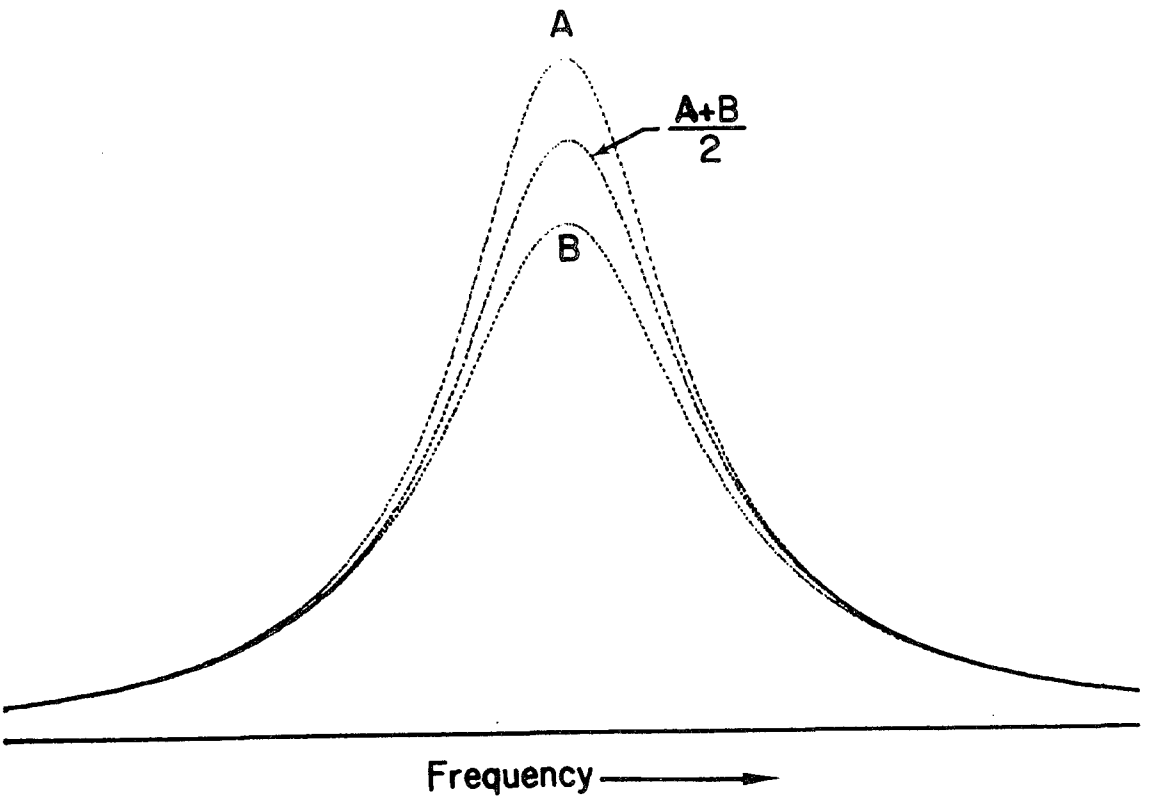

Figure 28A) Ultrasonic mechanical resonances for two hypothetical CdS resonators. The A sample is unsensitized while the B sample is sensitized. The resulting higher conductivity in the B sample leads to an increase in ultrasonic attenuation.

in the resonance peak by about 20%. Figure 28(B) is a plot of the derivative of the curves in figure 28(A). The location of the resonance peak may be determined from the zero crossings of the derivative. Although the same increase in conductivity as in figure 28(A) is calculated here, a shift in the zero crossings is indiscernible.

To help visualize the shift, the X and Y axis of figure 28(B) are expanded (a factor of 400 for the X axis and 30 for the Y axis) in figure 28(C). The change in resonance frequency shown in figure 28(C) corresponds to a change in $\Delta v/v$ of about 10%. One feature is apparent from this model. Large inhomogeneities in density of sensitizing centers can lead to discrepancies consistent with those measured in figure 27. The discrepancies are larger for attenuation than for velocity and result in a shift toward higher velocities.

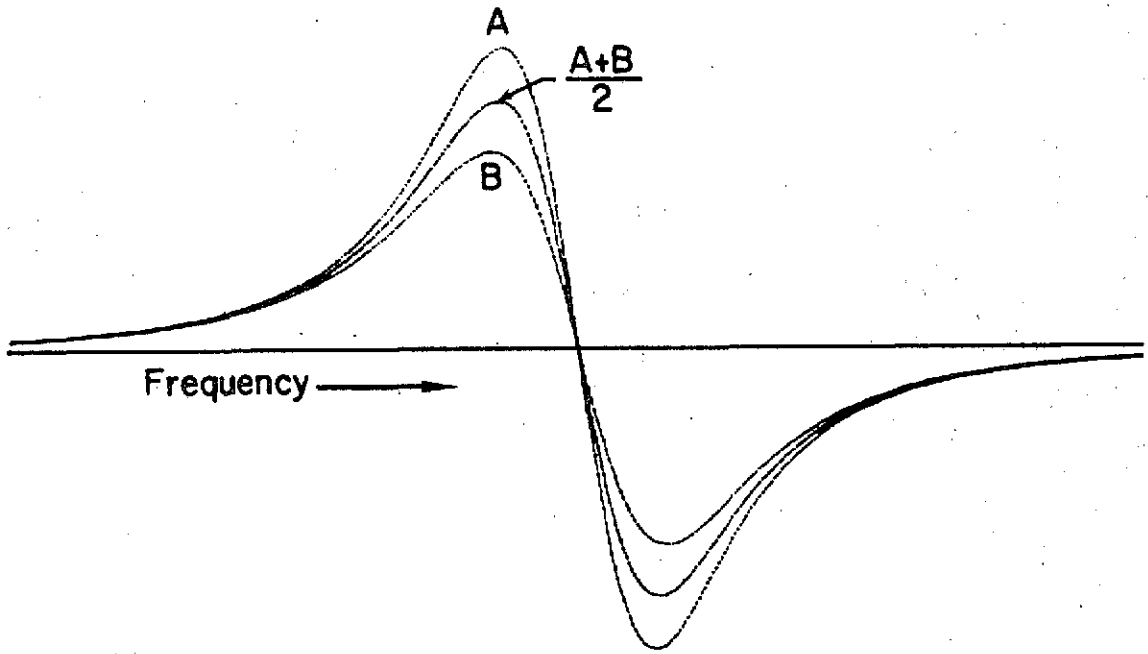

Figure 28B) Derivative of the ultrasonic mechanical resonances shown in the previous figure. A shift in the peak of the resonance produces a shift in the position of the zero crossings of the derivative. No shift is apparent on this scale.

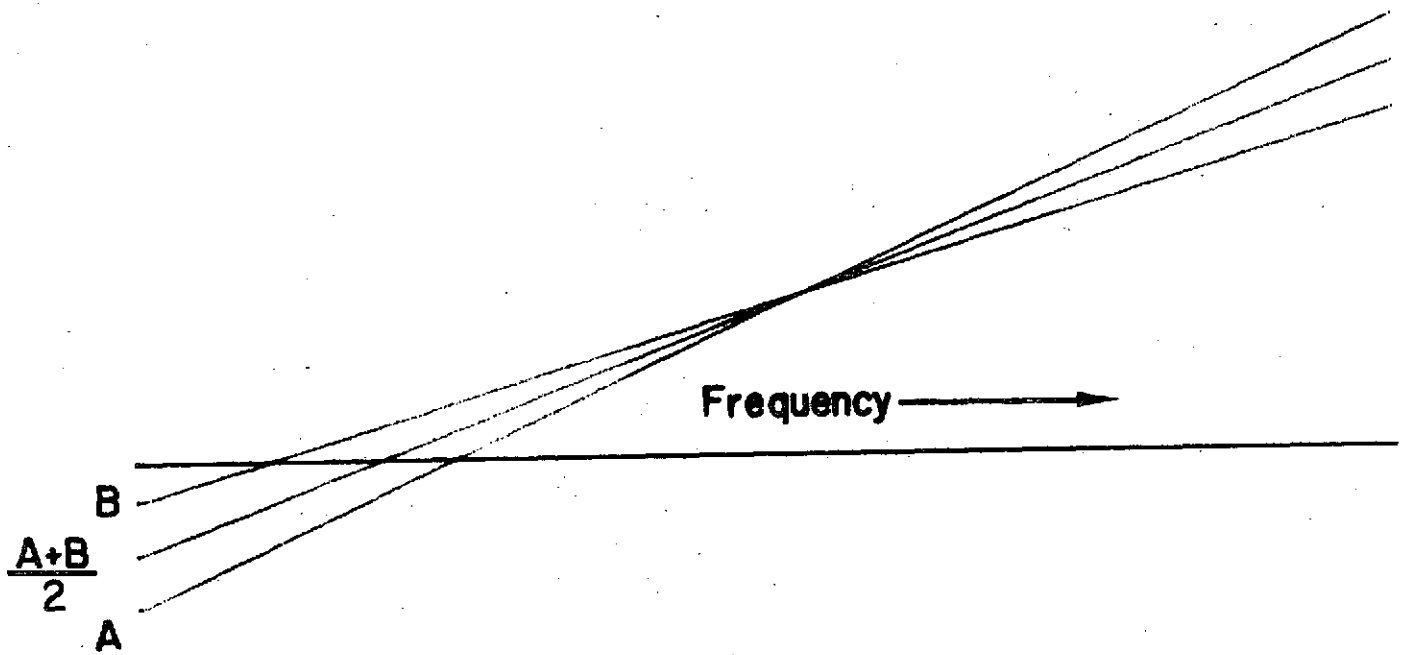

Figure 28C) Expanded axis of the derivative curves shown in the previous figure. The X-axis is expanded by a factor of 400 and the Y-axis is expanded by a factor of 30. On this scale, shifts in the zero crossings are apparent. In addition, the composite sample zero crossing is closer to the A side than to the B.

III-2. AN ULTRASONIC CALIBRATOR

In this section is described an ultrasonic calibration device. The theory of its operation is developed and the actual operation with an experimental sample is discussed. Data obtained with the calibrator is presented and a technique for calibrating the system with a secondary standard is described. Causes of calibration error are discussed.

The interaction of light on the ultrasonic properties of CdS suggests an application of this phenomena as a calibrator for ultrasonic spectrometers. In this section, an ultrasonic calibration device is described which is capable of producing known changes in both acoustic attenuation and phase velocity while simulating the essential ultrasonic properties of the specimen of interest. Since the calibration results from actual changes in acoustic properties rather than from an electrical simulation, not only are the electronic characteristics of the spectrometer accounted for by the use of the calibrator, so also are the sensitivity enhancement factors associated with the acoustic resonator. (See Section I-2) The calibration technique is based on the use of a CdS specimen whose ultrasonic properties can be adjusted and modulated with light as described in Section III-1.

The calibrator is being used with sensitive ultrasonic spectrometers capable of detecting small changes in acoustic phase velocity $\Delta v/v$ and attenuation $\Delta\alpha$ which occur in specimens during ultrasonically induced electron or nuclear spin resonance.[17] In order to relate the output of such a spectrometer (e.g., a voltage or a chart recording) to the physical parameters $\Delta\alpha$ and $\Delta v/v$, a calibration scheme is usually employed. Existing calibration schemes rely on an electrical simulation of the acoustic event which gives rise to the changes in

acoustic attenuation and phase velocity.[7,37,38] Although electrical calibration schemes of this sort are adequate in some respects, a more satisfying calibration technique would utilize actual changes in ultrasonic properties, e.g., changes in time domain decay rates or frequency domain line widths.[17] Without producing such actual changes in acoustic properties, a calibration scheme cannot properly include the sensitivity enhancement factors which arise from the use of ultrasonic resonators.[3,17]

III-2-1. DESCRIPTION AND THEORY OF OPERATION

A block diagram of the ultrasonic calibrator is presented in figure 29. The composite resonator consists of a CdS crystal to which is bonded an appropriate transducer so that longitudinal ultrasonic waves can be propagated along the C-axis. The flat and parallel single crystal of CdS was prepared from high purity photoconductive material. Light from both the bias and the signal lamps, which are powered by constant current sources, is focused on the CdS crystal. A light chopper and a platform carrying neutral density filters are in the optical path of the signal lamp. The entire assembly is housed in a light tight case external to which are controls that insert or retract various combinations of neutral density filters.

The physical basis for the calibration scheme is as follows. Because CdS is a good photoconductor, light incident on the crystal can change its electrical conductivity by many orders of magnitude. Since the charge carriers are coupled to the elastic properties of CdS by the piezoelectric mechanism, changes in electrical conductivity

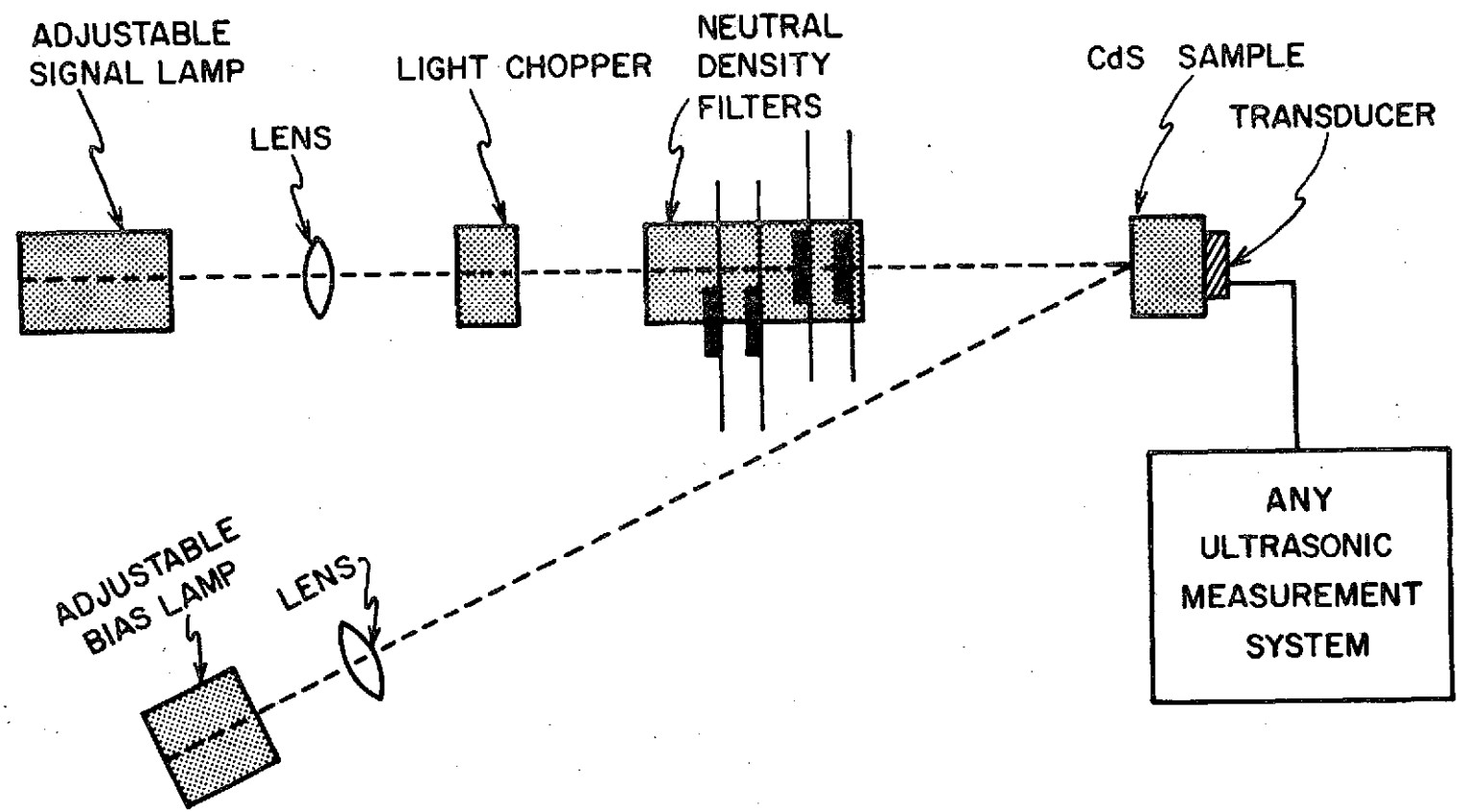

Figure 29) Block diagram of the ultrasonic calibrator.

result in changes in ultrasonic phase velocity and attenuation. This phonon-charge carrier interaction is treated with the aid of the formalism of Hutson and White[9] in Section III-1 and is shown in figure 27. By applying the phonon charge carrier interaction (Section III-1) to ultrasonic resonators (Section I-2), it is possible to obtain the necessary conditions for the operation of the calibrator.

For attenuation calibration, let us define A_1 as the ultrasonic signal related to the calibrator and A_1^* as the ultrasonic signal related to the specimen being studied. We recall that A_1 is the in-phase component of the ultrasonic signal as shown in equation I-3. If the assumption is made that $\alpha a \ll 1$ and $\alpha^* a^* \ll 1$ (starred quantities are related to the specimen) and that measurements are taken near a mechanical resonance, equation I-10 becomes:

$$\Delta A_1 = \frac{\Delta \alpha}{\alpha^2 a} \tag{III-6}$$

$$\Delta A_1^* = \frac{\Delta \alpha^*}{\alpha^{*2} a^*} \tag{III-7}$$

If the assumption is made that $\Delta A_1 = \Delta A_1^*$, then a condition exists such that $\Delta \alpha = \Delta \alpha^*$. The assumptions are justified in the section on calibrator operation. Using III-6 and III-7:

$$\frac{\Delta \alpha}{\alpha^2 a} = \frac{\Delta \alpha^*}{\alpha^{*2} a} \tag{III-8}$$

or

$$\alpha = \left(\frac{a^*}{a}\right)^{1/2} \alpha^* = \alpha_e \tag{III-9}$$

where α_e is defined as an effective attenuation. Therefore with the above conditions and assumptions met, the change in attenuation in the calibrator equals the change in attenuation in the specimen.

For dispersion calibration, we define A_2 as the ultrasonic signal related to the calibrator and A_2^* as the signal related to the specimen of interest. The A_2 response is the out-of-phase component of the ultrasonic signal shown in equation I-3. As before, we assume $\alpha a \ll 1$, $\alpha^* a^* \ll 1$ and that the measurements are taken near a mechanical resonance. Then equation I-11 becomes:

$$\Delta A_2 = \frac{1}{a^2 a} \Delta k \qquad \text{(III-10)}$$

$$\Delta A_2^* = \frac{1}{\alpha^{*2} a^*} \Delta k^* \qquad \text{(III-11)}$$

If we assume $\Delta A_2 = \Delta A_2^*$ we obtain:

$$\frac{\Delta k}{\alpha^2 a} = \frac{\Delta k^*}{\alpha^{*2} a^*} \qquad \text{(III-12)}$$

As before, a condition exists such that $\Delta k = \Delta k^*$. The condition is:

$$\alpha = \left(\frac{a^*}{a}\right)^{1/2} \alpha^* = \alpha_e \qquad \text{(III-13)}$$

We note that equation III-13 equals equation III-9. Therefore with the same conditions and assumptions met as before, the change in wave number in the calibrator equals the change in wave number in the specimen.

In summary then, the same changes in ultrasonic parameters that are occurring in the specimen of interest are adjusted to occur in the calibrator. The condition that $\alpha a << 1$ is easily met in most experiments. The other conditions that must be met for use of the calibrator are that $\Delta A_1 = \Delta A_1^*$ for attenuation measurements and $\Delta A_2 = \Delta A_2^*$ for dispersion measurements. In addition, the attenuation of the calibrator must be adjusted so that the results of equation III-13 or III-9 are met. These conditions are justified in the operation section. Similiar conditions apply for attenuation measurements using $|A|$ for the ultrasonic signal.

III-2-2. OPERATION OF THE CALIBRATOR

Using the same notation as in the theory section, operation of the calibrator is described and data are presented for absorption and dispersion calibrations. The first condition to be satisfied operationally is the adjustment of the calibrator background attenuation. The bias lamp is varied to obtain the condition that:

$$\alpha_e = \left(\frac{a^*}{a}\right)^{1/2} \alpha^*$$

This condition is easily accomplished for most experiments. The light chopper is turned on for synchronous measurements (AC) or left off for DC measurements. The next condition to be met uses the calibrated signal lamp to set $\Delta A_1 = \Delta A_1^*$ or $\Delta A_2 = \Delta A_2^*$ (the calibration of the signal lamp is discussed later). This condition is easily achieved for most experimental samples. Simply, neutral density filters are inserted into the signal lamp producing accurately known changes in

in light intensity. Since light intensity is nearly linearly related to ultrasonic absorption and dispersion over a region of figure 27, calibrated changes in the ultrasonic properties are produced (i.e., one-tenth of the signal lamp intensity produces one-tenth of the initial changes in ultrasonic properties). Therefore, a wide dynamic range of changes in parameters may be achieved since there is a wide dynamic range of conductivities in CdS (at least a factor of 10^5). The only limitations on the calibrator range are linearity considerations and spectrometer noise. These are discussed later with other sources of error.

III-2-3. CALIBRATOR RESULTS

With the appropriate conditions met as discussed previously, two different values of α_e were set (0.03 and 0.1 cm^{-1}) and calibration signals obtained for each as is shown in figure 30. These signals were measured with a synchronous amplifier tuned to the light chopper frequency and as such are an example of the AC mode of calibrator operation. Neutral density filters were inserted in the signal lamp path to obtain values of $\Delta\alpha$ for light intensity less than 1. The relative light intensity scale here has no connection to F, the relative light intensity scale in figure 27. The noise shown as error bars is believed due to spurious amplitude modulation in the spectrometer. The AC dispersion calibration was obtained in a similar

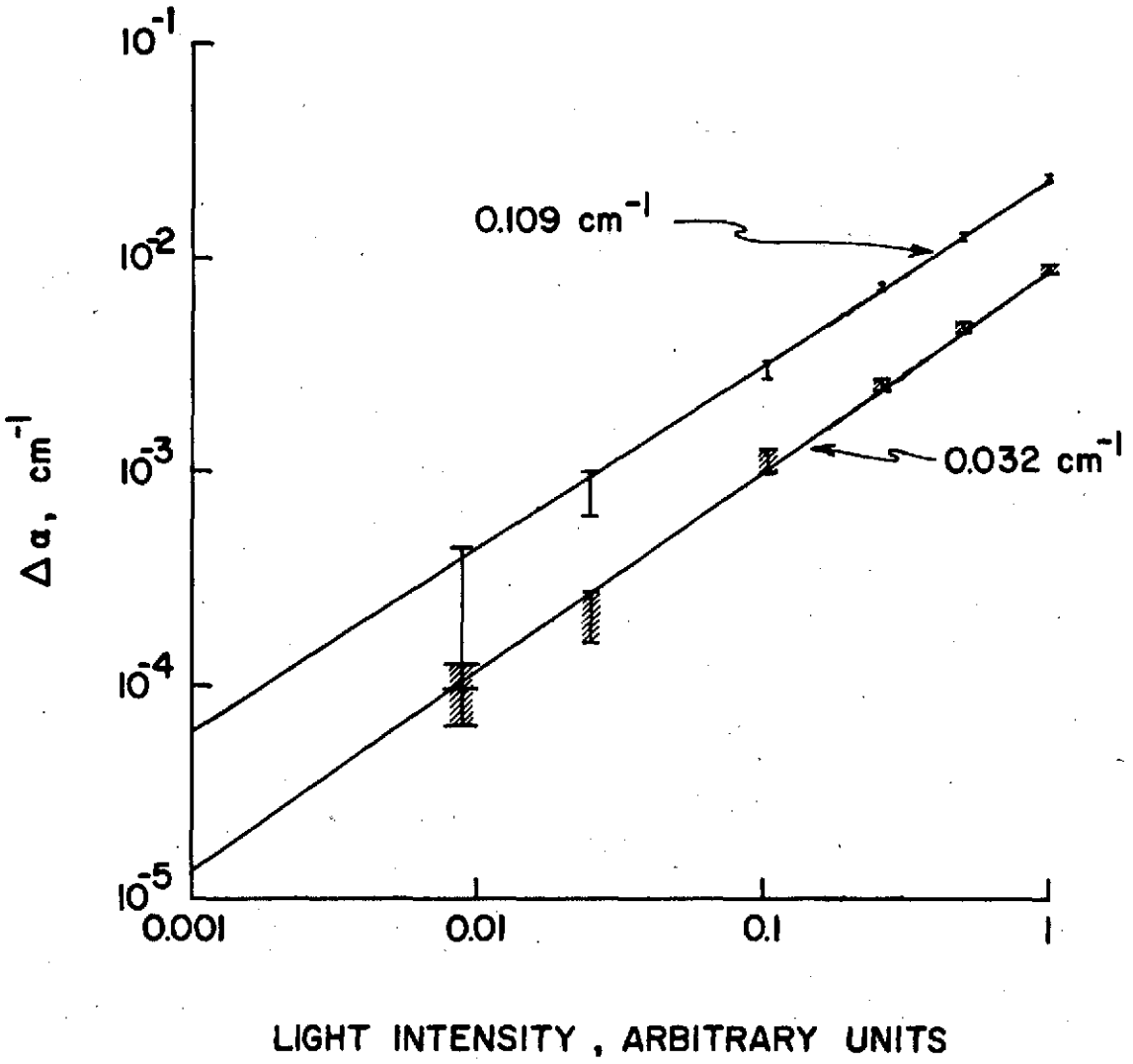

Figure 30) Absorption calibrator output (AC mode for two values of background attenuations.

fashion and is shown in figure 31. Once again, the noise shown as error bars is believed due to the spectrometer.

The second mode of operation for the calibrator does not make use of synchronous detection and is called the DC mode. For this operation, the light chopper is switched off and changes in ultrasonic parameters are measured with a direct coupled spectrometer. As before, calibrated changes in material properties are obtained by inserting various combinations of neutral density filters in the signal lamp path. Operation of the bias lamp is the same as for the AC mode. Figure 32 is an example of operation in the DC absorption calibration mode.

As an example of the flexibility of the calibrator, a special arrangement was set up. The output intensity of the signal lamp was modulated with a square wave at a very low frequency (about 0.1 Hz) with the calibrator operating in the DC mode. The bias lamp was adjusted to an intensity such that $F = 1 - \delta F$ and the signal lamp intensity adjusted to produce a $(2\delta F)$ change in light intensity. Therefore, a condition was produced so that ω_c varied from a value just less than ω to one just greater than ω. Since α is a double valued function symmetrical with respect to $F = 1$, little change in attenuation occurs between the two generated values of F. However, the dispersion is varying most rapidly during the condition $F = 1$ and the two generated values of F correspond to two different phase velocities. A very slow ultrasonic frequency sweep through the mechanical resonance with these conditions is shown in figure 33. A line connecting all the peaks in the modulation on the low frequency side with the minima on the high frequency side correspond to the $F > 1$ mechanical resonance. Likewise, a line connecting all the minima on the

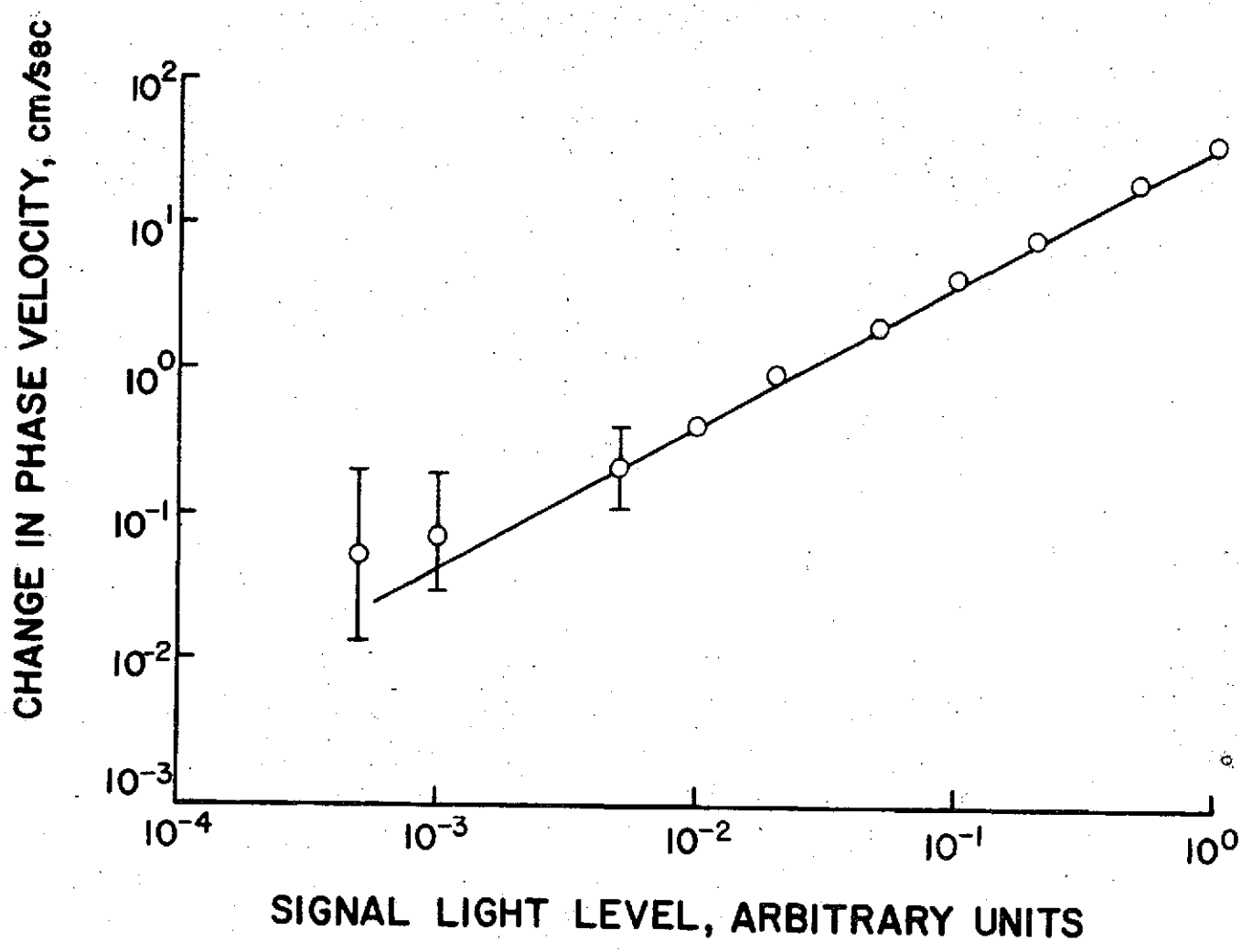

Figure 31) Dispersion calibrator output (AC mode).

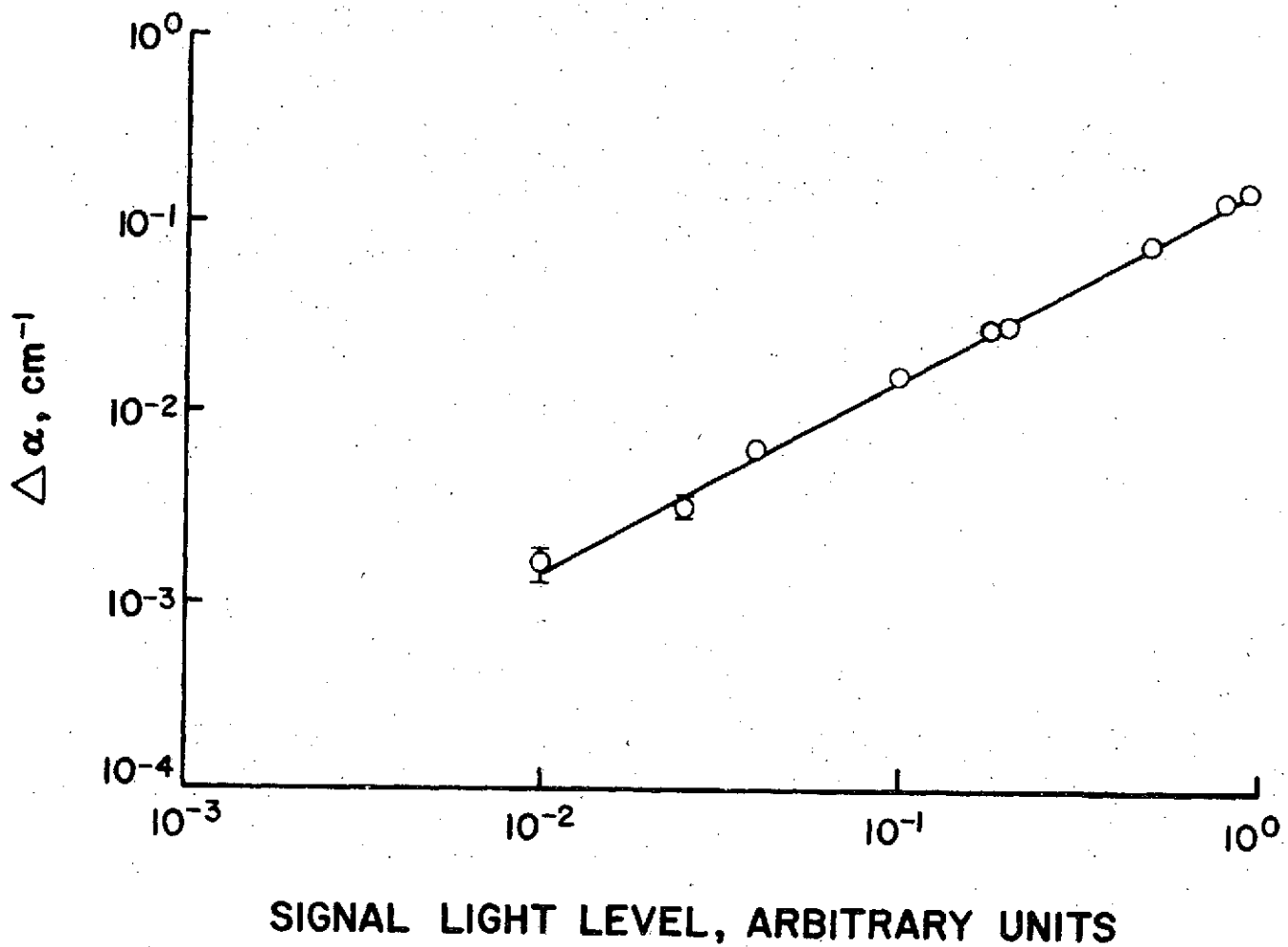

Figure 32) Absorption calibrator output (DC mode).

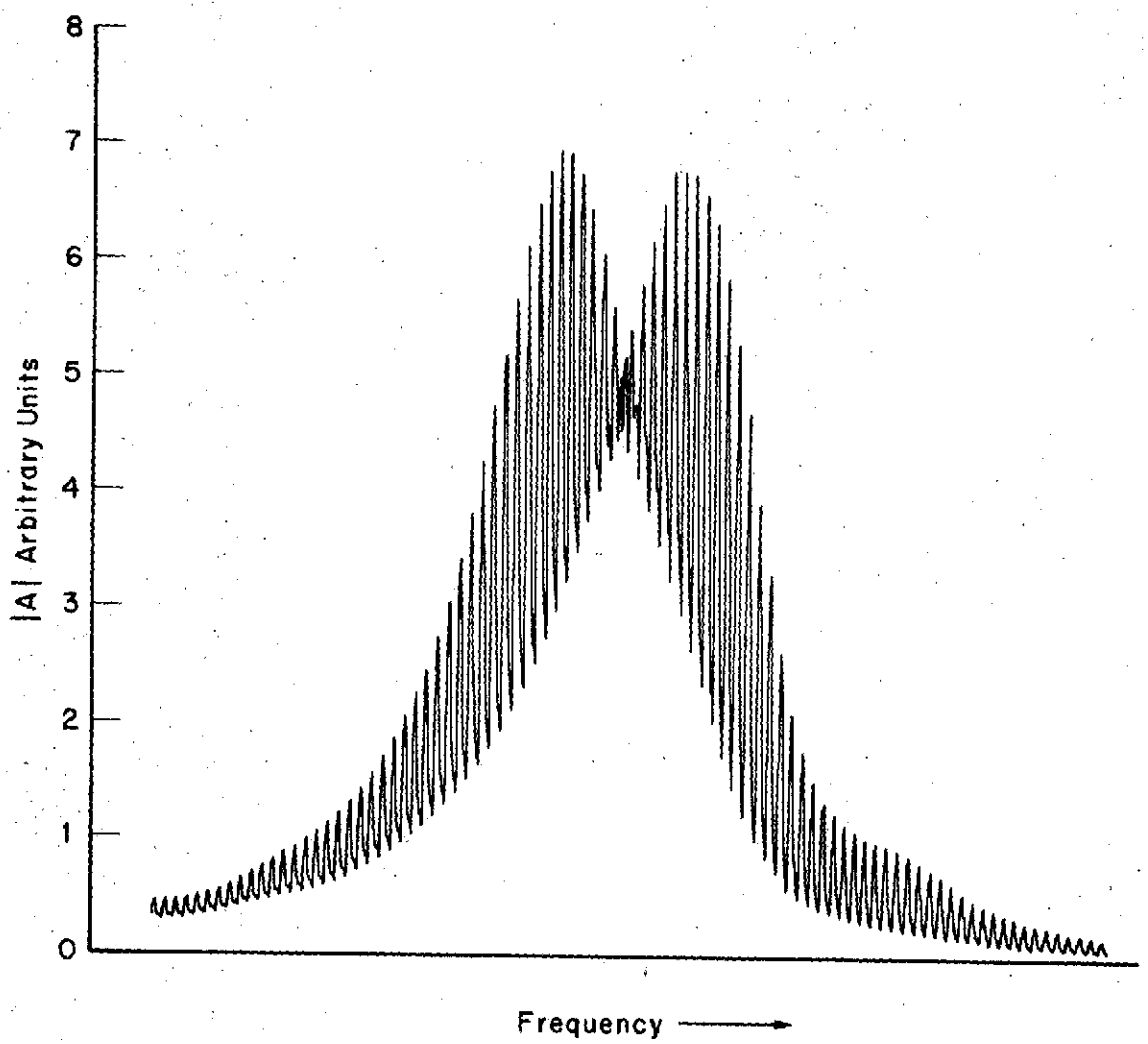

Figure 33) Mechanical resonance of a CdS sample illuminated at just below maximum photogenerated acoustic absorption. In addition, a modulated lamp shining on the CdS raises the conductivity (on the minus part of the modulation) to just above the maximum absorption. The resulting figure shows changes in both absorption and dispersion as well as sensitivity enhancement effects (see text).

low frequency side with the peaks on the high frequency side represent the condition $F < 1$. In addition, a line connecting the midpoints of the modulations represents the condition $F = 1$. The zero in the modulation amplitude between the two mechanical resonances represents the peak of the mechanical resonance at $F = 1$. Therefore, in one figure we can see dispersion as shifts of the mechanical resonance peak with respect to $F = 1$, and changes in absorption as a reduction in peak height at $F = 1$. In addition we see the $F = 1$ increased mechanical resonance width with respect to the widths of the $F = 1 \pm \delta F$ curves. Also in this figure is shown the sensitivity enhancement factor as a change in the amplitude of the modulation. In fact, if we were to plot the modulation amplitude vs. frequency, we would obtain a rectified image of figure 4.

III-2-4. CALIBRATION OF THE CALIBRATOR

For attenuation, the calibrator system is itself calibrated with an external insertion-loss standard. For this purpose, we use standard click-stop 0.1 and 1.0 dB attenuators. Changes in the ultrasonic signal (ΔA_1, ΔA_2, or $\Delta|A|$) are carefully measured by AC coupling the detected RF signal to an oscilloscope. First, the calibrator attenuation is adjusted to α_e as described in the theory operation. Next, the signal lamp intensity is set such that the change in ultrasonic signal produced by the attenuator is exactly matched by that produced by the signal lamp. For AC operation, the light chopper is on so that the change in ultrasonic signal appears as a modulation at the chopper frequency. For DC operation, the change in ultrasonic signal is a

decrease in the detected amplitude. With the attenuation calibration procedure performed as above, the change in attenuation $\Delta\alpha$ in the CdS equals the change in attenuator setting in dB. To verify that the above conditions calibrate the system, it is necessary to examine what is actually measured.

Let us define A_1 as the ultrasonic signal used with the calibrator. Also, define A_1' such that the observed change in calibrator output due to the signal lamp is $\Delta A_1 = A_1 - A_1'$. Furthermore, we let C be the attenuator insertion loss factor determined from:

$$xdB = 20 \log \left(\frac{cA_1}{A_1}\right) \qquad \text{(III-14)}$$

where x is the dB change dialed in. Then:

$$c = 10^{\left(\frac{x}{20}\right)} \qquad \text{(III-15)}$$

For example, if $x = 1$, $c = 1.122$. When the calibrator signal is set equal to the signal produced by x attenuation loss, we obtain the condition:

$$A_1 - A_1' = A_1 - cA_1 \qquad \text{(III-16)}$$

Therefore, $A_1' = cA_1$ and since at the peak of resonance $A_1 = (1/\alpha a)$ it can be shown that:

$$\alpha' = \frac{\alpha}{c} \qquad \text{(III-17)}$$

The change in α in dB is:

$$20 \log \frac{\alpha}{\alpha'} = 20 \log c^{-1} \equiv -x \text{ dB} \qquad \text{(III-18)}$$

Therefore, the change in α in the calibrator is accurately known and is equal to the change dialed into the attenuator. Even though no mention has been made of sensitivity enhancement during this initial calibration, it has been taken into account during the procedure. Equations I-10, I-17, and I-18 can be used to describe a change in the A_1 signal at the resonance peak using the sensitivity enhancement factors as:

(III-19)

$$A_1 - A_1' = \Delta A_1 = \frac{\partial A_1}{\partial \alpha} \Delta\alpha = \frac{1}{\alpha^2 a} \Delta\alpha = \frac{\left(\frac{c-1}{c}\right)}{\alpha^2 a} \alpha = A_1 \left(\frac{c-1}{c}\right)$$

where c is the change in α as in equation III-17. From III-19, we deduce that $A_1' = A_1/c$ so

$$x\text{dB} = 20 \log \frac{A_1}{A_1'} = 20 \log c \qquad \text{(III-20)}$$

This is the result expected from equation III-14 and therefore, sensitivity enhancement factors have been taken into account.

For dispersion measurements, the calibrator is calibrated with an accurate frequency counter. Whether we change k or k_m in the equations of section I does not affect the amplitudes of changes in ultrasonic signals. Therefore, we may frequency modulate (FM) the RF carrier to produce the same effect amplitude wise as a modulated-phase

velocity. The identical procedure is followed for dispersion as for attenuation except we use the A_2 (out-of-phase) ultrasonic signal (see section I). Instead of using for comparison the change in A_2 due to an attenuator, we use the change in A_2 due to a known FM amplitude. The signal lamp intensity is set to produce the same ΔA_2 as the FM produces. As before, the Δk for the signal lamp is then equal to the Δk for the FM oscillator.

III-2-5. CALIBRATOR ERROR ANALYSIS

Two basic assumptions are made for the calibrator. The most important is that conductivity varies nearly linearly with light intensity. For the lower levels of illumination, most likely used with the calibrator, this is true. Deviations from linearity at intense illumination or low temperatures have been seen[39] but differ from sample to sample. An error such as this would be apparent instantly from the calibrator output, since a plot such as figure 30 would not be linear. In fact, if data similar to that in figure 30 are linear at the more intense illuminations, they will surely be linear at the more important smaller changes in parameters.

The second basic assumption is that the slope of light intensity versus absorption or dispersion as shown in figure 27 is constant over the region being used. In fact, the slope changes are small. For example, the slope of the attenuation curve is:

$$\frac{d\alpha}{dF} = \frac{K^2}{2} \frac{\omega}{v} \frac{1 - F^2}{(1 + F^2)^2} \qquad \text{(III-21)}$$

But this need not introduce a large error in the system. Once the calibrator has been calibrated for some value of α_e (i.e., F has been set with the bias lamp), the error introduced by equation III-21 is fixed by the range of $\Delta\alpha$ used. For most experimental work, the smaller $\Delta\alpha$ values are most significant since large changes in α may be directly measured from resonance width studies.[17] For example, in figure 30 the $\alpha = 0.032$ cm.$^{-1}$ curve covers about two orders of magnitude in $\Delta\alpha$, yet the slope changes by less than 0.02 percent which is insignificant. Actually, so long as $F < 0.2$ the change in slope of α versus light (equation III-21) changes by only 5 percent. This means that the calibrator need not be recalibrated for each specimen of interest at a small decrease in accuracy. However, for highest accuracy, the procedure outlined in the previous section should be used for each change in specimen especially for values of $F > 0.2$.

Other non-theory errors are related to the accuracy of the neutral density filters (5 percent for this case), the stability of the lamp intensities, and finally, noise in the spectrometer itself.

III-3. ACOUSTOELECTRIC ULTRASONIC POWER DETECTOR

In this section results of theoretical and experimental analysis are presented for an acoustoelectric ultrasonic power detector similar to one discussed in reference 12. The significance of power detection for pulsed as well as CW measurements is described. Calculations of the acoustoelectric voltage based on a theoretical model with both constant as well as exponential electron density are presented for a flat and parallel ultrasonic resonator. An anomolous change in sign of the acoustoelectric voltage for certain conditions of resonator length and charge distribution is reported which has not been accounted for theoretically. Experimental data are presented which agree with other aspects of the theoretical model and further demonstrate the benefits of power detection.

Ultrasonic measurements made on flat and parallel samples are relatively easy to obtain with either pulse echo or continuous wave techniques. Modern applications, however, have taken ultrasonics from the laboratory with controlled flatness and parallelism to the real world of non-destructive testing and biological monitoring. Serious difficulty in interpreting ultrasonic data often arises for these modern applications. A significant cause of unusable data is phase modulation due to non-homogeneous samples and non-parallel reflecting interfaces. For example, phase variations due to non-parallelism make accurate attenuation measurements difficult if not impossible[13,40] and lead to inhomogeneous broadening[17] of mechanical resonance width and modulation of pulse echo decay patterns. A detection technique insensitive to phase information in the acoustic wave would eliminate phase modulation

effects in the resulting signal. Since ultrasonic power is related to the square of particle velocity, a true power detector would be insensitive to relative phase variations in particle displacement in an ultrasonic wave. Therefore, a physical phenomena linearly related to acoustic power can be used as the basis of a power detector. The acoustoelectric effect is such a phenomena.

III-3-1. THE WEINREICH RELATIONSHIP WITH CONSTANT ELECTRON DENSITY

As discussed in Section III-1, the coupling of an ultrasonic wave to charge carriers in a piezoelectric semiconductor leads to an increased absorption. A second aspect of this absorption is an electric field (or current) due to the phonon wave. This latter effect is called the acoustoelectric (AE) effect, theoretically predicted by Parmenter[41] in 1953. Physically, the AE effect is produced by the transfer of momentum from the ultrasonic wave to the conduction electrons and valence holes. The coupling mechanism between the phonons and charge carriers may be either the deformation potential or the piezoelectric effect. The first observation of the AE effect was by Weinreich & White[42] in 1957. In reference 42, the deformation potential coupling to charge carriers was observed in germanium. Weinreich[43] links the magnitude of the AE effect to the loss of energy by the ultrasonic wave. His argument is that the momentum flux carried by the ultrasonic wave (which is the energy flux divided by the wave velocity) must appear as a dc force exerted on the free carriers which absorb the ultrasonic wave. Therefore, the AE effect manifests itself externally either as a current (for a short circuited device) or as an electric field E_{AE}. The net result of the momentum transferred is:[44,45]

$$E_{AE} = \frac{\Phi}{v} \frac{\alpha}{ne} f \qquad \text{(III-22)}$$

where Φ is the power flux in the wave, v is the wave velocity, α is the attenuation, n is the carrier density, e is the charge per carrier, and f is the fraction of mobile space charge (1-f is trapped). Equation III-22 is valid under the assumptions that $\omega_D >> \omega$ and that the drift velocity due to fields in the resonator is much less than the ultrasonic phase velocity. Using equation III-4 and III-22 with the relationship that $\sigma = ne\mu$, one obtains:

$$E_{AE} = \frac{K^2}{2} \frac{\Phi\mu}{\varepsilon v^2} \left[\frac{\omega^2}{\omega^2 + \omega_c^2} \right] \qquad \text{(III-23)}$$

For the case $\omega_c << \omega$, the acoustoelectric field is independent of frequency. However, for $\omega_c >> \omega$, the field varies as the square of frequency. The frequency dependence would seem to eliminate the acoustoelectric effect as a candidate for use in the power detector. In fact, for the power detector we measure an AE voltage V_{AE} which, as shown below, eliminates the frequency dependence problem.

The frequency dependence of E_{AE} is eliminated when we integrate the field through the length of the detector. If the assumption is made that the detector is flat and parallel, that insignificant mode conversion occurs at the reflection boundary and that complete reflection occurs at that boundary the V_{AE} becomes:

$$V_{AE} = \int_0^{a/2} E_{AE}\, e^{-\alpha x} dx - \int_0^{a/2} e^{-\frac{\alpha a}{2}}\, E_{AE} e^{-\alpha x} dx +$$

$$\int_0^{a/2} e^{-\alpha a} E_{AE}\, e^{-\alpha x} dx - \ldots =$$

$$\frac{E_{AE}}{\alpha}\left[1 - e^{-\frac{\alpha a}{2}}\right] \sum_{j=o}^{\infty} \left(-e^{-\frac{\alpha a}{2}}\right)^j \qquad \text{(III-24)}$$

where $a/2$ is the detector length. This result is similar to one derived in reference 12. If we neglect carrier trapping (valid for $\omega^{-1} >> \tau = 10^{-9}$ seconds trapping time)[44] and combine equation III-23 and III-24, the acoustoelectric voltage becomes:

$$V_{AE} = \frac{\Phi}{nev}\left[1 - e^{-\frac{\alpha a}{2}}\right] \sum_{j=o}^{\infty} \left(-e^{-\frac{\alpha a}{2}}\right)^j \qquad \text{(III-25)}$$

A plot of this function is shown in figure 34 for values of $\frac{\alpha a}{2}$ equals 0.1, 0.5, 1.0, and 2.0 for a constant n (i.e., fixed α). Note that the oscillatory behavior of V_{AE} damps out with increasing reflection number and increasing $\alpha a/2$. In fact for large $\alpha a/2$, V_{AE} becomes a function of acoustic flux only (n fixed). This condition is ideal for a power detector. Other optimum conditions for this simple model are apparent in figure 35. Here, V_{AE} from equation III-25 is plotted as a function of $\alpha a/2$ for several values of j. The acoustoelectric voltage generated for the $j = o$ term is larger in amplitude than for any other j value. This indicates that for this model, zero reflections in the power detector would achieve the optimum V_{AE}. Zero

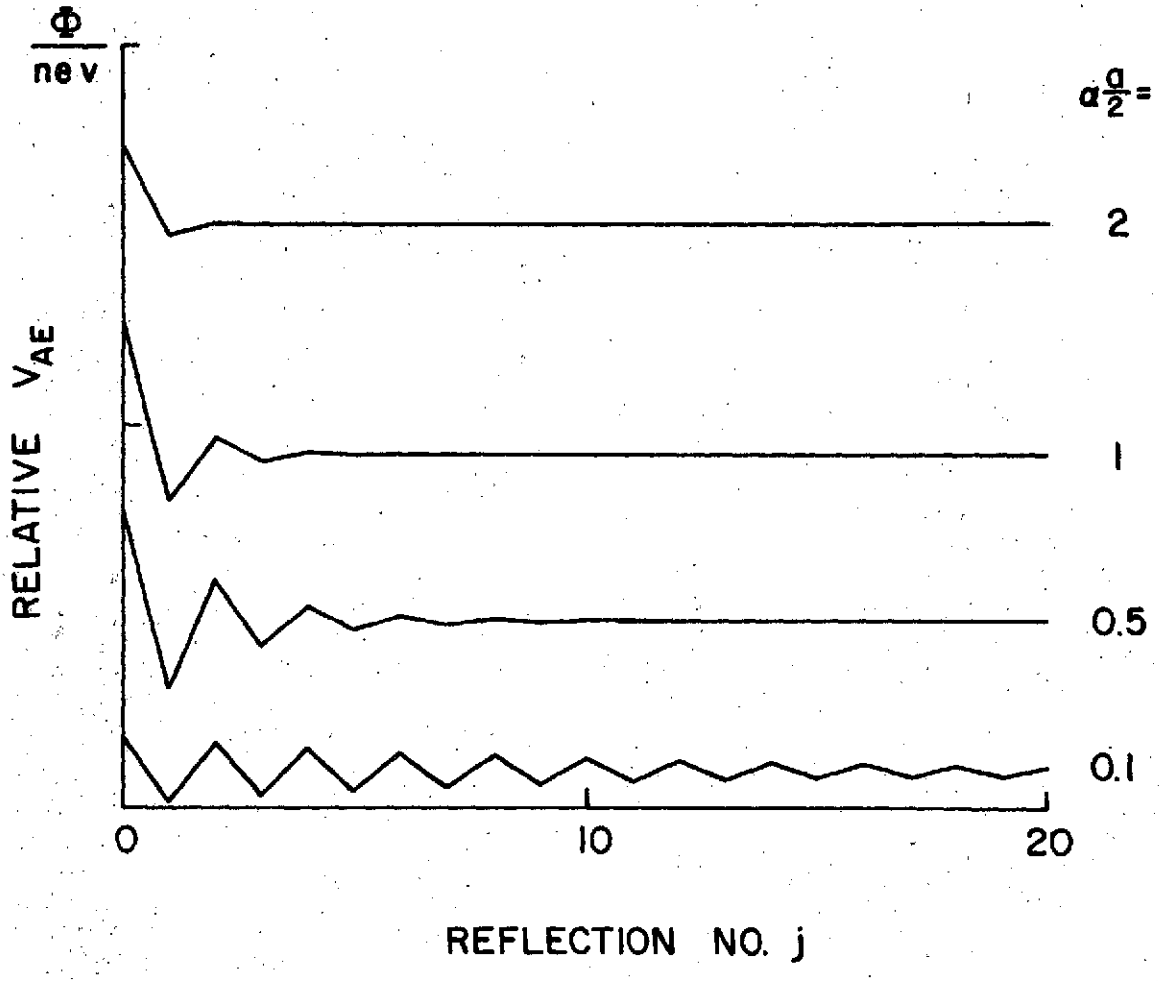

Figure 34) Acoustoelectric voltage for several values of $\alpha a/2$ as a function of reflection number j. Note that j = 0 produces the largest V_{AE} for a particular value of $\alpha a/2$ (fixed n).

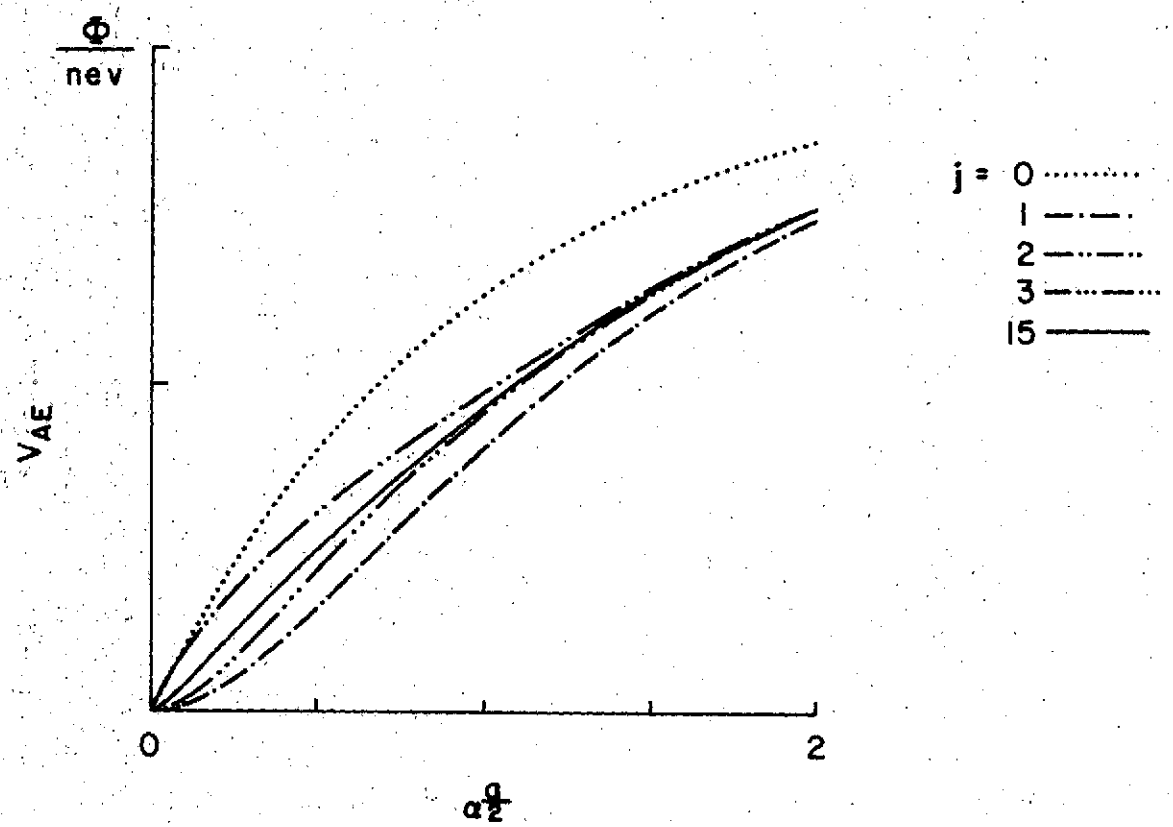

Figure 35) The acoustoelectric voltage for several different values of j, as a function of αa/2. This shows that the condition j = 0 optimizes V_{AE} (for fixed n).

reflections can be achieved by properly matching the acoustic impedance of the power detector with that of an external material. Impedance matching is nearly realized by waxing the reflective surface thereby absorbing the acoustic wave without reflection[17].

III-3-2. THE WEINREICH RELATIONSHIP WITH EXPONENTIAL ELECTRON DENSITY PROFILE

Although III-25 does indicate some design parameters, a more complete model should include effects due to non-constant electron density. A simple method of controlling n makes use of the photoconductive properties of CdS. By varying n and therefore α, an optimum V_{AE} should be achieved for various detector configurations. A simple method of controlling n makes use of the photoconductive properties of CdS. If we assume ultrasound is incident on a CdS power detector from the $x = a/2$ side and light incident from the $x = o$ side, we have a complicated combination of effects to include.

For example, the light intensity is not constant through the length of the crystal. This is due to the light absorption ($\bar{\alpha}$) in the crystal. For light with a wavelength corresponding to an energy greater than the bandgap ($\lambda < 0.5$ micrometers), the photon absorption coefficient is about 10^5 cm.$^{-1}$ and drops to less than 1 cm.$^{-1}$ near $\lambda = 1.0$ micrometer. A second complication due to non-constant n concerns the electron mobility. Since electron mobility is a function of conductivity, a numerical solution for the V_{AE} became necessary. A computer program was written (see appendix 1) for a Hewlett Packard computer to include some of the effects of a non-constant n. For this analysis, n is replaced with:

$$n = n_o \exp(-\bar{\alpha} x) \qquad \text{(III-26)}$$

where n_o is the photoelectron concentration near the surface. To calculate the mobility, experimental data reported in reference 39 was used to derive the following empirical relation:

$$\mu \simeq (33 \log n - 200) \text{ cm}^2/\text{volt-second} \qquad \text{(III-27)}$$

This relationship is valid for values of $10^9 < n < 10^{14}$. To apply the theoretical calculations to an experimental detector, the value of n_o is related to a measurable external parameter - detector resistance. The assumption is made that the detector is a 0.7 × 0.7 × 0.1 millimeter slab of photoconductive CdS. The resistance of such a slab is found to be:

$$R = \int_0^{a/2} \frac{\rho(x)dx}{A} = \int_0^{a/2} \left[\frac{(n(x)e\mu)^{-1}}{A}\right]dx \qquad \text{(III-28)}$$

Substituting equation III-26 into III-28 and solving for the surface electron density we obtain:

$$n_o = \frac{[\exp(\bar{\alpha}\, a/2) - 1]}{Ae\mu R\, \bar{\alpha}} \qquad \text{(III-29)}$$

where R is the detector resistance in ohms, and A is the detector cross sectional area in cm.^2. An iterative method is used to obtain final values of n_o assuming an effective mobility in the calculations.

Basically, the value for n_o in equation III-29 is used in equation III-27 to obtain a new value of μ which in turn is used to calculate a new value of n_o. The conductivity is then determined by:

$$\sigma(x) = n(x)e\,\mu(x) \qquad \text{(III-30)}$$

and used in equation III-5 to calculate the ultrasonic absorption due to the phonon - charge carrier interaction. Finally, equation III-23 is used with the above calculations to obtain a value for the acousto-electric voltage:

$$V_{AE} = \sum_{\substack{\text{all}\\ \text{reflections}\\ j=o}}^{\infty} \sum_{i=o}^{i=N} \Delta x\, E_{AE}(x) = \sum_{\substack{\text{all}\\ \text{reflections}\\ j=o}}^{\infty} (-1)^j \sum_{i=o}^{i=N} \left(\frac{a}{2N}\right) E_{AE}(x) \qquad \text{(III-31)}$$

where N equals the summation interval.

A detailed program of these calculations is shown in appendix 1.

The results of these calculations for values of $\bar{\alpha}$ from 1 to 100 are shown in figures 36(A), 36(B) and a summary in figure 36(C). For each case, a low conductivity ($\sigma = 1.6 \times 10^{-6}$ $(\Omega\text{-cm})^{-1}$) and a high conductivity ($\sigma = 7.5 \times 10^{-6} (\Omega\text{-cm.})^{-1}$) AE voltage are presented. In figures 36(A) and 36(B), V_{AE} is shown as a function of reflection number which is the number of times the ultrasonic wave is at the $x = o$ surface. For these calculations, it is assumed that the acoustic excitation is left on so that we are observing the V_{AE} superposition to equilibrium.

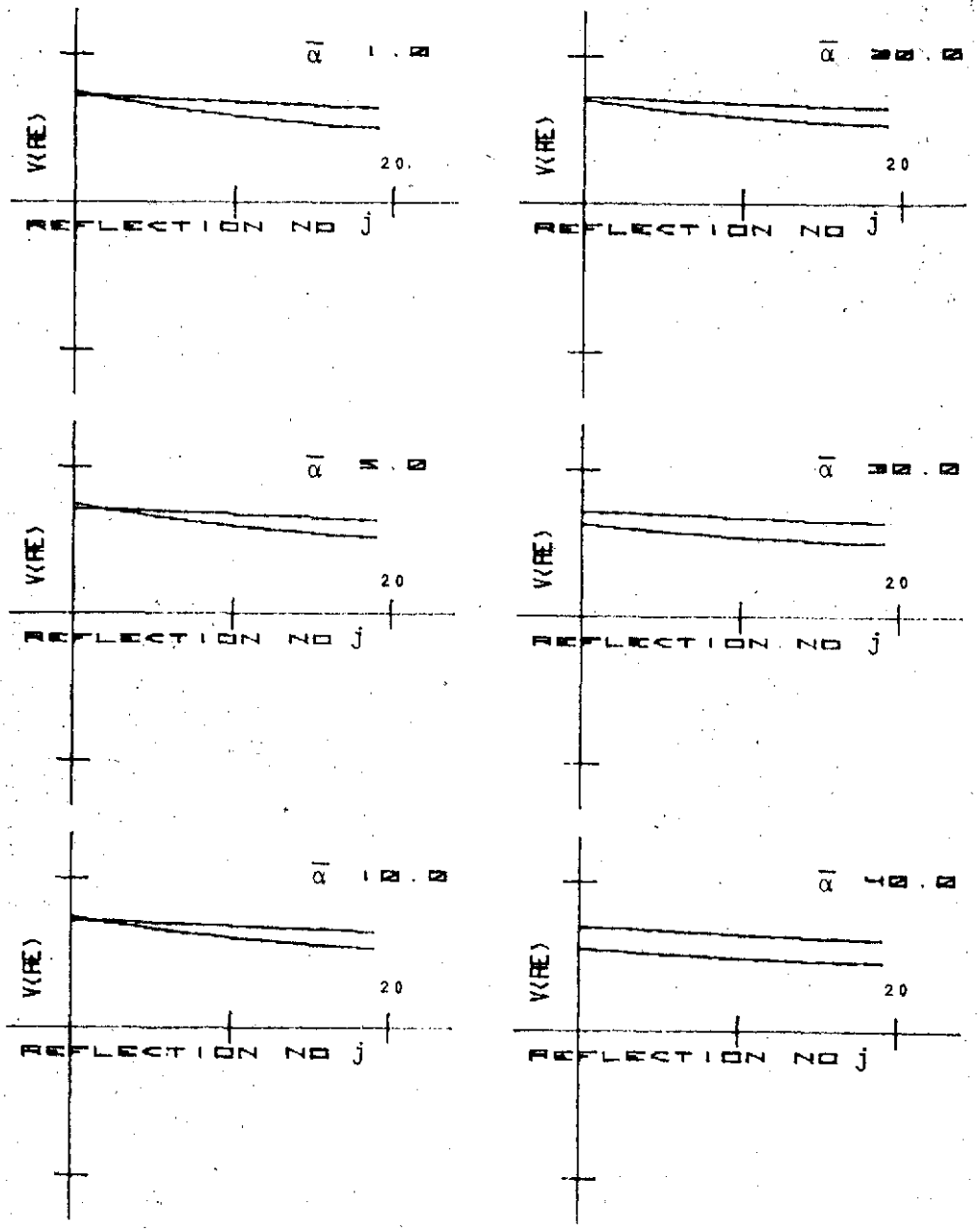

Figure 36A) The acoustoelectric voltage for both high and low conductivity samples as a function of reflection number j for several different values of optical absorption $\bar{\alpha}$. Reflection number j corresponds to the x=0 surface.

108

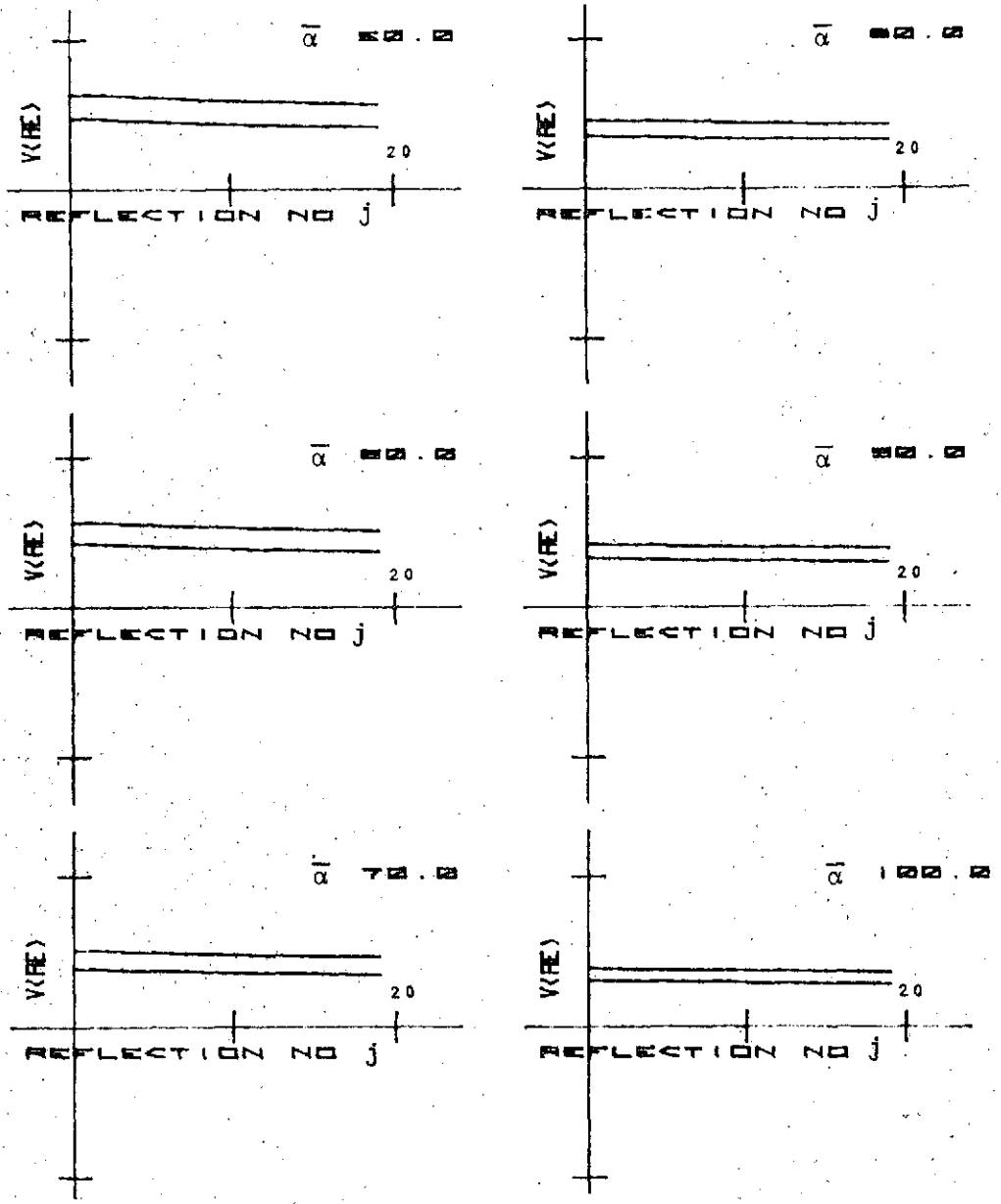

Figure 36B) The acoustoelectric voltage for both high and low conductivity samples as a function of reflection number j for several different values of optical absorption $\bar{\alpha}$. Reflection number j corresponds to the x=0 surface.

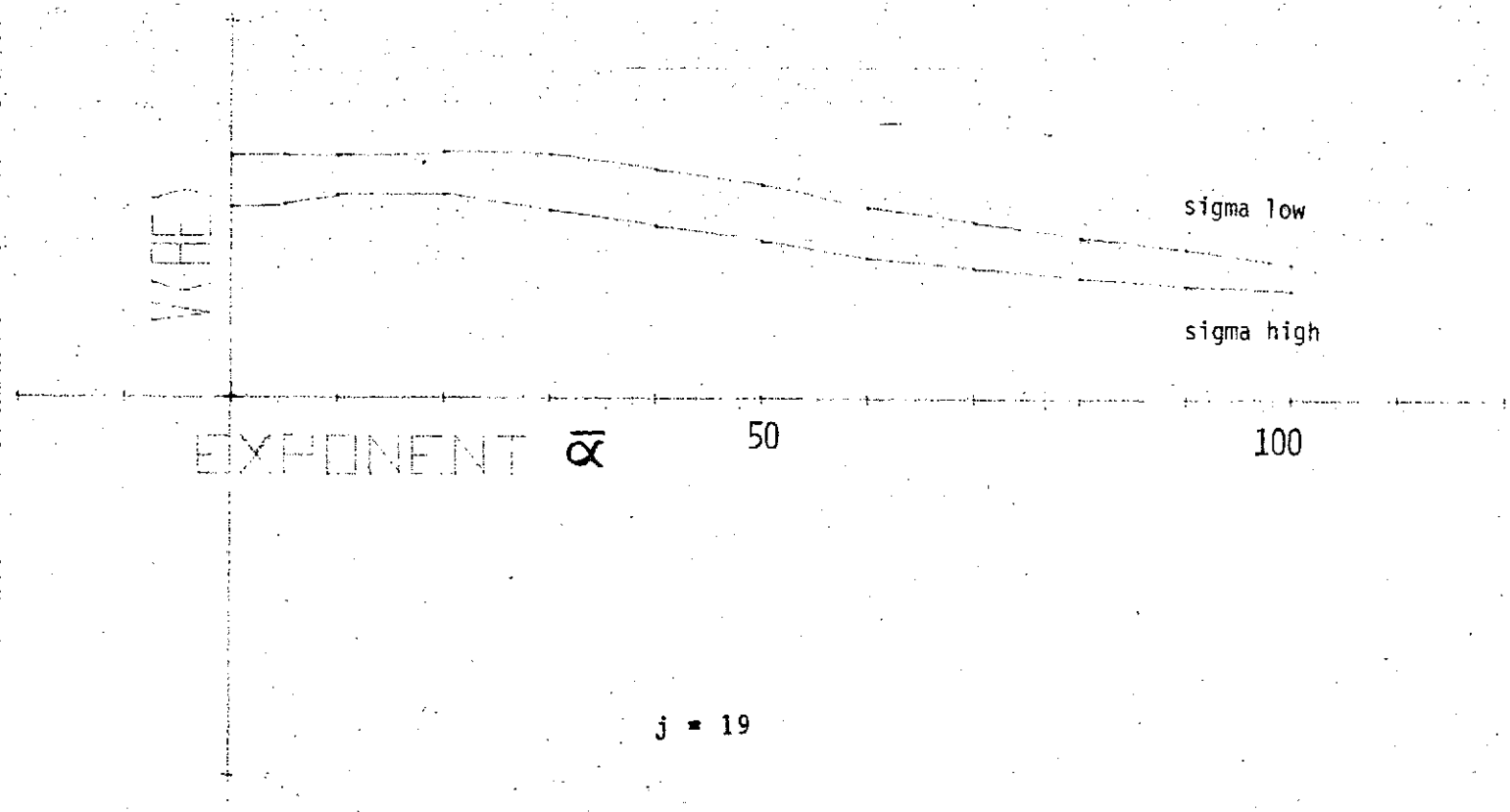

Figure 36C) The acoustoelectric voltage at reflection number j=19 for both high as well as low conductivity samples as a function of optical absorption $\bar{\alpha}$. Reflection number j corresponds to the x=0 surface.

Figures 36(A) and 36(B) show the effects of non-uniform charge carrier distribution on V_{AE}. For the cases presented, the low conductivity V_{AE} are greater than the high conductivity V_{AE}. In addition, as $\bar{\alpha}$ increases the V_{AE} decreases. This is more clearly shown in figure 36(C) which shows V_{AE} vs $\bar{\alpha}$. The results of the simple model shown in figure 34 and 35 are not sufficient to predict the effects of a non constant n. In fact, even the more complex model does not predict an anomalous sign reversal of the acoustoelectric effect reported in the following section.

III-3-3. EXPERIMENTAL RESULTS

An experimental AE detector was built to verify the results of the simple as well as the more complex model. The basic design of the detector is shown in figure 37, along with the experimental arrangement utilized to obtain both the AE detector response as well as the phase-sensitive response.

The CdS detector for this test purpose was a 0.7 × 0.7 × 0.1 millimeter slab cut from a boule of single-crystal type A photoconductive material. The "C" axis was aligned normal to the flat and parallel faces. The crystal was bonded with indium or a coloidal solution of graphite (aquidag) to a quartz resonator. Ultrasonic energy introduced and measured in the quartz by a sampled CW (see Section II-1) ultrasonic spectrometer is compared with the measured V_{AE}. For this purpose, the CdS is weakly coupled to the quartz sample minimizing perturbation to the resonator acoustic field.

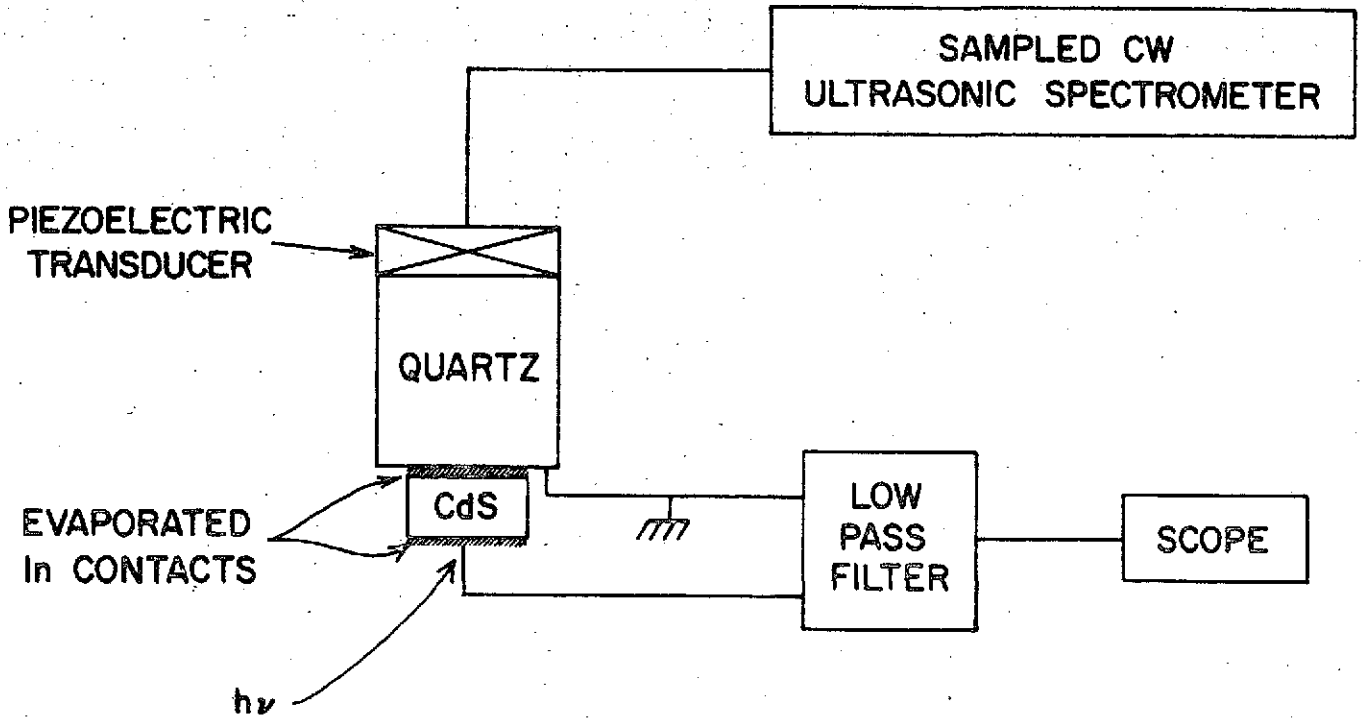

Figure 37) Acoustoelectric power detector test configuration. The CdS power detector has one transparent In contact. Piezoelectric voltages generated in the power detector are blocked by the low pass filter so that only acoustoelectric voltages are displayed on the oscilloscope.

The sampled CW response for this resonator shown in figure 38 was first reported by us in reference 46. Superimposed in this figure are the outputs of an AE detector and a piezoelectric detector for a sampled CW parallel resonator decay at 5 MHz. The piezoelectric detector is shown as an RF envelope while the AE detector appears as a solid line. As anticipated, the AE power response decays at twice the rate of the piezoelectric voltage response. Although this means the AE detector will be in the noise faster than a piezoelectric detector, this is not a severe handicap for most signal levels.

Figure 39 shows a more familiar pulse echo decay for a non-parallel quartz sample. Again, as in figure 38, both a piezoelectric detector (lower figure) and an AE detector (upper figure) are shown. In each case, an electronically-generated exponential decay is superimposed on the decays for comparison. The piezoelectric detector shows severe non-parallelism effects (phase cancellation) while the AE detector matches the electronically-generated exponential decay. These agree with similar figures shown in reference 12. While it would be difficult to determine an absorption for the piezoelectric detector case, it is simple for the AE detector case.

Instead of looking at the time domain decay as in figures 38 and 39, figure 40 shows a frequency domain line shape for both the piezoelectric and AE detectors for a parallel resonator at 14 MHz. The AE response is approximately the square of the piezoelectric response with the full width at 1/2 power in agreement to about 1 percent (9.4 KHz for the piezoelectric case, 9.3 KHz for the AE case). Recall that 1/2 power for the piezoelectric detector occurs at 0.707 peak height while 1/2 power for the power detector is at 1/2 peak height.

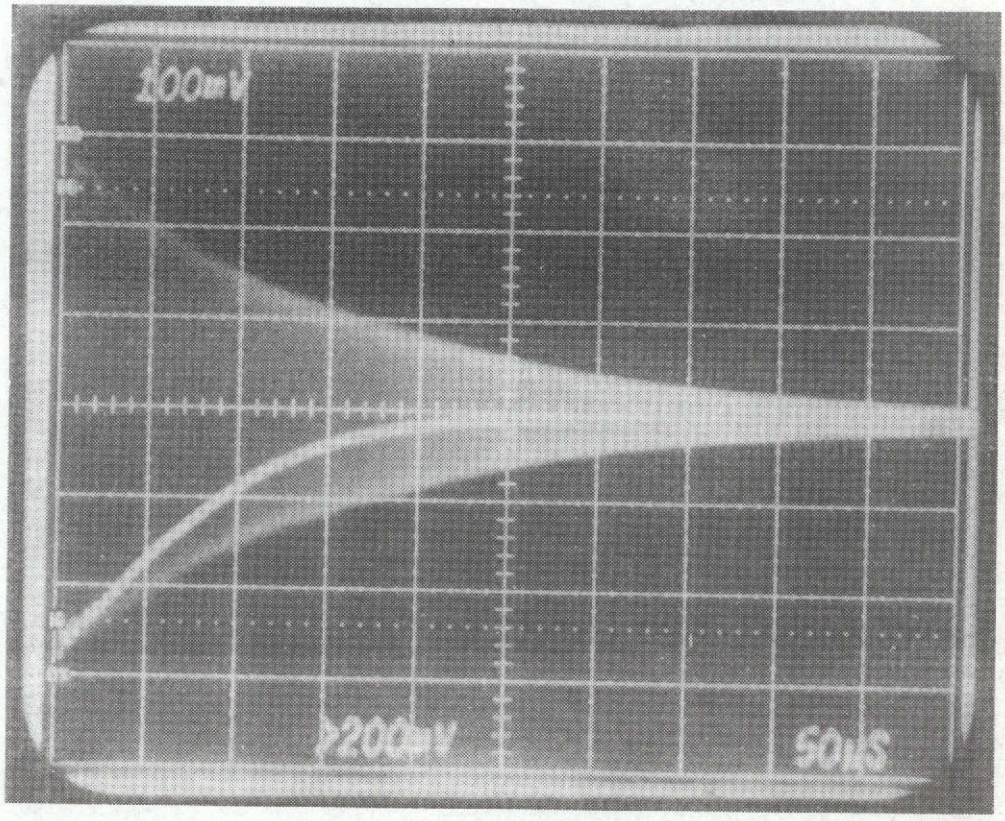

Figure 38) A sampled CW response for the test configuration of figure 37 showing the response of both the power detector (solid line) as well as a piezoelectric detector (RF envelope). The power detector voltage decays at twice the rate of the RF envelope (ie. power is proportional to voltage squared).

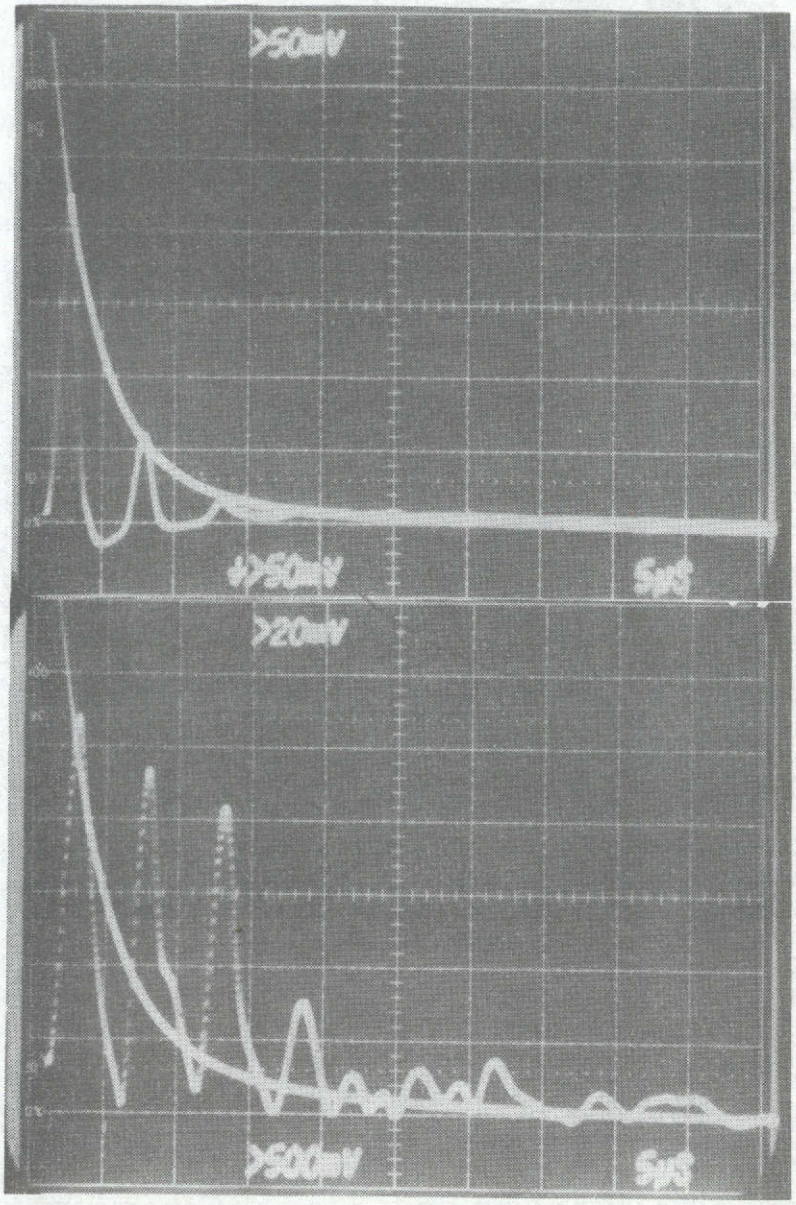

Figure 39) Pulse echo pattern of a non-parallel quartz resonator as measured by the power detector (top figure) and a piezoelectric transducer (bottom figure). An electronically generated exponential is superimposed on the decay pattern for comparison. The power detector conforms to the exponential decay while the piezoelectric detector is modulated by inhomogeneous phase shifts thereby making measurements difficult.

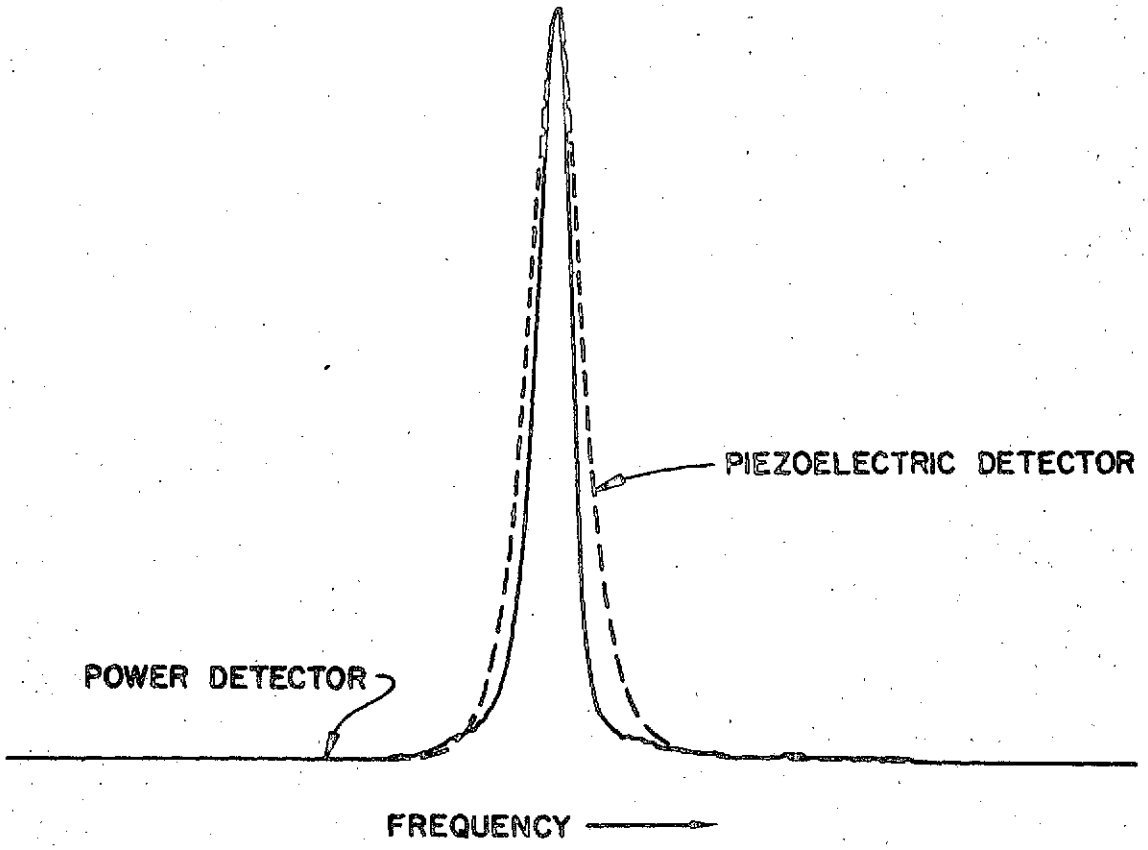

Figure 40) Frequency domain lineshape for a parallel quartz resonator as measured by a power detector (solid line) and a diode detected piezoelectric transducer (dashed curve). Half maximum on the power detector corresponds to 0.707 on the piezoelectric detector.

Figure 41 shows the same situation for a non-parallel sample. Of interest are the several peaks present in the AE response that do not appear in the piezoelectric response. It is believed that phase-cancellation effects obscure the "real" resonance shape in the piezoelectric response. Therefore, information is lost by not using power detection where phase cancellation occurs.

The experimental results reported in figures 38-41 verify the operating characteristics of a power detector as predicted by the simple n = constant model. Complications due to phase modulation of the ultrasonic wave are clearly absent in the pulse echo data for a non-parallel sample. In addition, SCW data show that the AE detector decays at twice the rate of a normal phase-sensitive detector as is expected. To verify the more complex $n \neq$ constant model, the same experimental configuration shown in figure 37 is used to obtain the data reported in figure 42. When the light amplitude was varied a region was located where V_{AE} would change sign due to a change in sample photoconductivity. The upper oscilloscope figure shows both V_{AE} (top trace) and the sampled CW decay (bottom trace). The sign of the V_{AE} is positive indicating an anomalous acoustoelectric voltage. The sign reversal has not to date, been accounted for. The RF is seen to decay in less than 100 microseconds while the acoustoelectric voltage is seen to decay in about 250 microseconds. The long decay time is attributed in part to the RC time constant of the low conductivity sample and the measurement equipment.

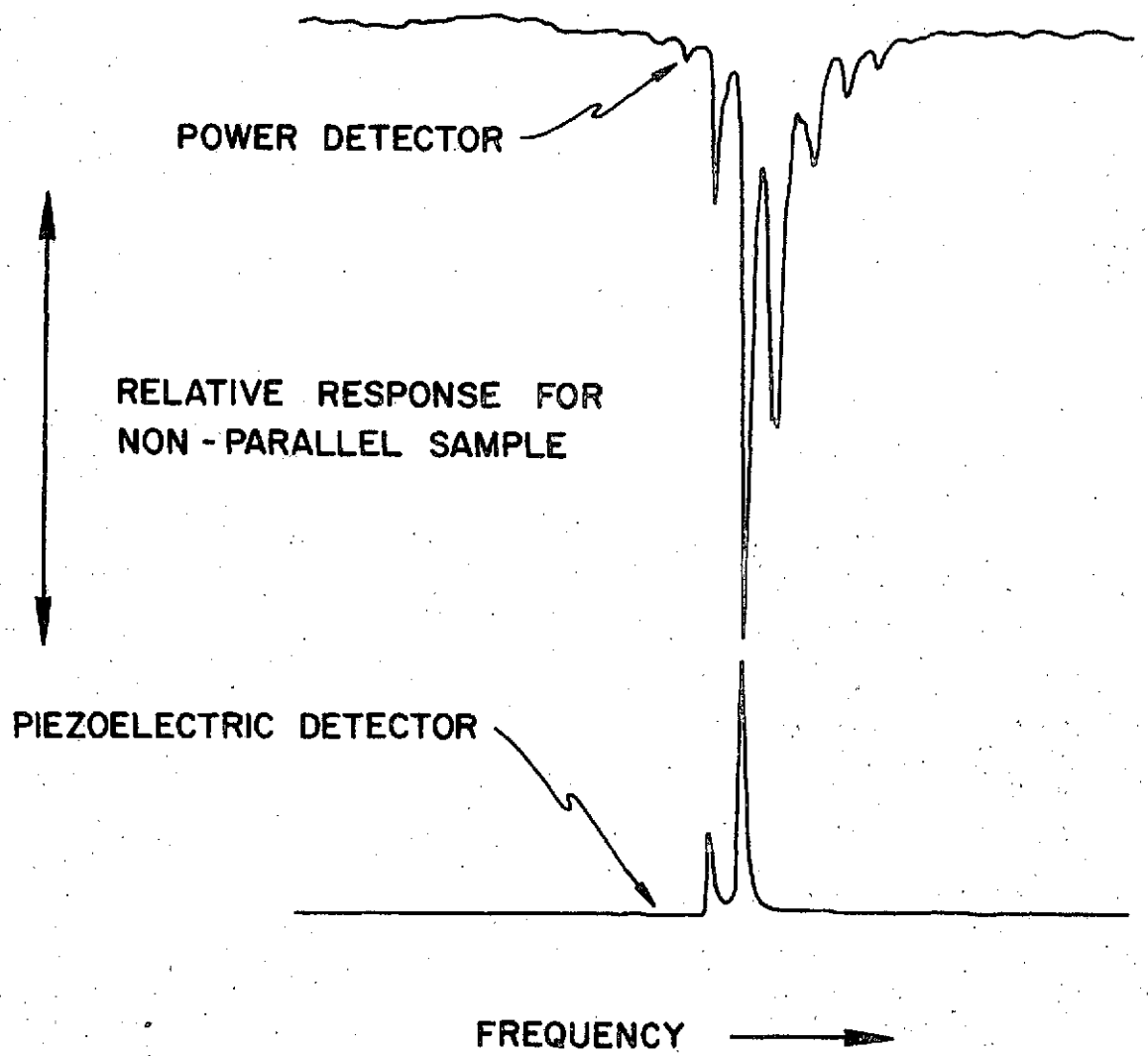

Figure 41) Frequency domain lineshape for a non-parallel quartz resonator as measured by a power detector and a piezoelectric detector. The additional peaks in the power detector lineshape are missing in the piezoelectric lineshape. This is attributed to phase cancelation resulting in lost information.

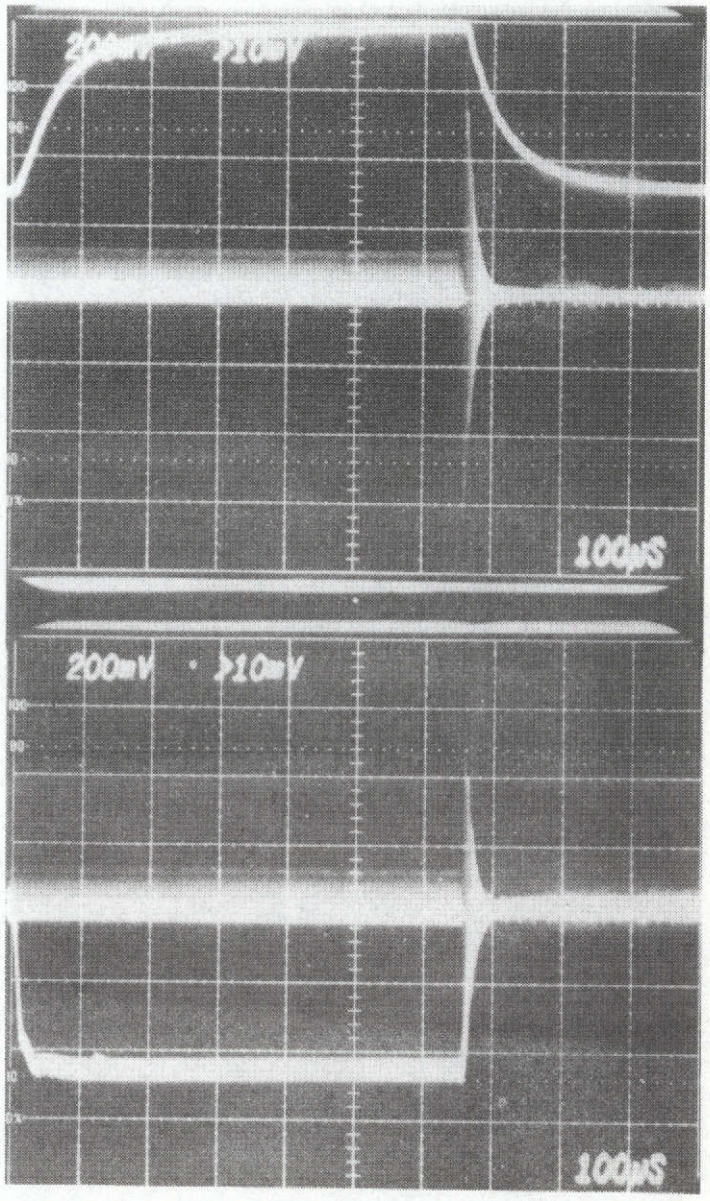

Figure 42) SCW time domain decays for both the power detector and the piezoelectric detector for low sample conductivity (upper oscilloscope picture) and for high sample conductivity (lower oscilloscope picture). The power detector voltage reverses sign in the lower picture and is not explained by theory.

The lower oscilloscope figure shows the case for high conductivity. The decay of the V_{AE} is two times faster than the decay of the RF (as verified in figure 38) since V_{AE} is power and the RF is voltage. The sign of the V_{AE} is now negative compared to the upper oscilloscope figure (low conductivity) and behaves as is predicted by the acousto-electric effect.

The experimental results along with the proposed model indicate that it is necessary to take the photoelectron density distribution into account to analyze the acoustoelectric effect for cases where n is not constant. Figures 35 and 36 indicates that an optimization of V_{AE} can be found by varying $\bar{\alpha}$ and reflection number. In fact, the model may be used to obtain optimum conditions for the parameters of sample length, conductivity, electron distribution, and reflection number to suit a particular application.

TABLE 1 - Comparison of Pulse Echo and Tous Spectrometers

	Parameter	Pulse echo PE	Continuous wave (TOUS)
1.	Cost	$20K	$1K ($0.2K perhaps)
2.	Instantaneous relative power	1000	1
3.	Dead time	50% or higher	≈0.1% per count/min at most
4.	Sensitivity enhancement	≤ 10 in water (complicated by echo selection)	≈10 in water (simple)
5.	Marginal oscillator signal enhancement	None	$\approx 10^2$ with signal to noise improvement of ≈5 over existing CW techniques
6.	Particle resolution in water	~100 μ	≈50 μ to be improved in the future
7.	Complexity	Complex	Inherently simple
8.	Frequency uncertainty	$\approx 10^6$ Hz	≈10 Hz

TABLE 2 - Electronic Parameters for Figure 36(A) and 36(B)

VALUES FOR FIGURE 36A			VALUES FOR FIGURE 36B		
$\bar{\alpha}$	R, 10^3 ohms	n_o	$\bar{\alpha}$	R, 10^3 ohms	n_o
1	27	2.9×10^{11}	45	27	4.2×10^{12}
1	120	7.1×10^{10}	45	120	1.1×10^{12}
10	27	4.4×10^{11}	50	27	6.2×10^{12}
10	120	1.1×10^{11}	50	120	1.5×10^{12}
20	27	7.8×10^{11}	55	27	9.0×10^{12}
20	120	2.0×10^{11}	55	120	2.2×10^{12}
30	27	1.5×10^{12}	60	27	1.3×10^{12}
30	120	3.7×10^{11}	60	120	3.3×10^{12}
35	27	2.1×10^{12}	70	27	3.0×10^{13}
35	120	5.2×10^{11}	70	120	7.3×10^{12}
40	27	2.9×10^{12}	100	27	3.6×10^{14}
40	120	7.4×10^{11}	100	120	8.8×10^{13}

APPENDIX

The following program calculates the acoustoelectric voltage VAE generated across a photoconducting CdS power detector illuminated from the x = o side and having ultrasonics generated from the x = R1 side. The program takes into account the non-uniform charge distribution in the crystal and the effect this has on the ultrasonic attenuation and therefore, the acoustoelectric voltage. The variation of electron mobility with photoconductivity is included in the calculation.

The program is written for the following equipment:

1) Hewlett Packard 9820A Calculator
2) Hewlett Packard 9862A Calculator Plotter
3) User Definable Function I 11222A ROM
4) Mathematics 11221A ROM
5) Peripheral Control I 1220A ROM
6) Option 0001 (429 storage registers) on the 9820A

LIST OF VARIABLES (program only)

R1	length of sample (cm.)
R2	initial ultrasonic energy flux
R3	R1/B
R4	Sample resistance (0.49 cm^2 area × 0.1 cm long)
R5	n_o in equations III-26, electron density
R6	number of reflections, j
R7	counter for plotter control
R8,R9	storage scratch pad

A ultrasonic energy flux

B number of major divisions in the integral of equation III-15. Near the x = o surface the interval is divided into B/10 (at x = 0.2R1) and B/100 (at x = 0.01R1) to include high surface absorption.

C VAE, the acoustoelectric voltage

x distance from the light incident side (in cm.)

y $\bar{\alpha}$, exponent in equation III-26

FA function calculates mobility cm^2/volt-sec

FB function calculates conductivity $(\Omega\text{-cm})^{-1}$

FC function calculates ultrasonic absorption (cm^{-1})

FD function calculates electron density as a function of x

FE function calculates "surface" electron density

STEP #

0: TABLE 4; TABLE 5; Enter "FLUX", A → R2, B, "LENGTH", R1, "R", R4, Y; Fixed 1

1: Scale - 4, 24, - 1.3, + 1.3

2: Axes 0, 0, 2, 0.1

3: Letter - 2, 0.2, 632; Plot "V(AE)";
Letter - 3, - 0.2, 631; Plot "Reflection NO"

4: R1-R1/B→X; R1/B → R3; If R9 = 0; FE (R4, Y) →R5; 1 → R9; Letter 15, 1, 631; Plot "Yb"; Plot y

5: FD (X+R1/2B)→R30; If R6 = 20; Go to 30

6: FA (R30) → R31; If A/R2 ≤ 0.02; Go to 30

7: FB (R30, R31) → R33

```
8:  FC (R33) → R32; A exp (-(R32 + 0.01)R3) → R8; If R8/R2 ≤ 0.02;
    Go to 30
9:  (C + R3 * 1.4E13 * A * R32/R30) → C
10: Aexp(-(R32 + 0.01)R3) → A
11: If R7 = 0; Space 1; Plot R6, C
12: If  x = 0; Go to 18
13: If  x ≤ 0.01*R1; x - 1E - 3*R1 → x; 1E - 3*R1 → R3; jump 3
14: If  x ≤ 0.2 R1; x - 1E-2*R1 → x; 1E - 2*R1 → R3; jump 2
15: If  R6 ≠ 20; If  A/R2 > 0.02; x - R1/B → x; R1/B → R3
16: Go to 5
17: If  x = 0.01 R1; jump 2
18: If  x ≤ 0.01R1; x + 1E-3*R1 → x; 1E-3*R1 → R3; jump 4
19: If  x = 0.2 *R1; jump 2
20: If  x ≤ 0.2*R1; x + 1E - 2*R1 → x; 1E-2*R1 → R3; jump 2
21: x + R1/B → x; R1/B → R3
22: FD (X-R1/2B)→R30
23: FA (R30) → R31
24: FB (R30, R31) → R33
25: FC (R33) → R32
26: (C - R3 * 1.4E13*A*R32/R30) → C
27: A exp (-(R32+0.01)R3) → A
28: If  x = R1; R6+1 → R6; plot R6, C; Go to 15
29: Go to 17
30: PEN
31: Letter R6, C, 221; plot R1; 0 → C; R1 + 0.1 → R1; print "No",
    R5; R2 → A; print A; 0 → R7 → R6
32: If  R1 > 1; Go to 34
```

```
33:  Go to 4
34:  PEN
35:  END
```

USER DEFINABLE FUNCTIONS

Function FA - calculates μ, mobility

```
Step #
    0:  If  P1 ≤ E9; 97 → F; jump 3
    1:  If  P1 > E15; 295 → F; jump 2
    2:  33 LOG P1 - 200 → F
    3:  end
```

Function FB - calculates σ, conductivity

```
Step #
    0:  P1P2 * 1.6E - 19 → F
    1:  END
```

Function FC - calculates α, ultrasonic absorption at 5 MHz

```
Step #
    0:  2.8E - 5(P1/(P1P1 + 6.8E - 10)) → F
    1:  END
```

Function FD, calculates $n(x)$, charge density for $n(x) \geq 10^6$

```
Step #
    0:  If  Y + P1 > 2; jump 3
    1:  If (R5*exp (-YP1) → P2) > E6; P2 → F; jump 4
    2:  If  P2 ≤ E6; jump 2
```

3: If (R5* exp (-YP1) → P2) > E6; P2 → F, jump 2

4: If P2 ≤ E6; E6 → F

5: END

Function FE, calculates n_o in equation III-10

Step #

0: 170 → P4

1: (1/49)(1/(P1*1.6E - 19*P4P2))(exp (R1 P2) - 1) → P3

2: If Absolute value ((FA(P3) - P4)/P4 ≤ 0.05; jump 2

3: FA(P3) → P4; jump -2

4: If P3 > E6; (P3 → R5) → F; jump 2

5: (E6 → R5) → F

6: END

BIBLIOGRAPHY

1. Tim Burkholder (publisher), Industrial Research, 16, No. 10, Oct. 1974, pp. 23.

2. J. G. Miller and D. I. Bolef, J. Appl. Phys., 39, No. 10, Sept. 1968, pp. 4589.

3. Joseph S. Heyman and J. G. Miller, J. Appl. Phys., 44, No. 8, Aug. 1973, pp. 3398.

4. Joseph S. Heyman, NASA TND-7417, Dec. 1973.

5. J. G. Miller and D. I. Bolef, Rev. Sci. Instr., 40, No. 7, July 1967, pp. 915.

6. Mark S. Conradi, J. G. Miller, and Joseph S. Heyman, Rev. Sci. Instr., 45, No. 3, March 1974, pp. 358.

7. J. G. Miller and D. I. Bolef, J. Appl. Phys., 41, No. 6, May 1970, pp. 2282.

8. Joseph S. Heyman, J. G. Miller, Dennis R. Dietz, and F. D. Stone, to be published.

9. A. R. Hutson and D. L. White, J. Appl. Phys., 33, No. 1, Jan. 1962, pp. 40.

10. Joseph S. Heyman and J. G. Miller, NASA Tech Brief, B73-10420, Dec. 1973.

11. Joseph S. Heyman and J. G. Miller, NASA Invention Disclosure LAR-11435-1, submitted for U.S. patent.

12. P. D. Southgate, J. Acous. Soc. Am., 39, No. 3, 1966, pp. 480.

13. Rohn Truell, Charles Elbaum, Bruce B. Chick, Ultrasonic Methods in Solid State Physics, (New York: Academic Press, 1969).

14. J. R. Pellam and J. K. Galt, J. Chem. Phys., 14, No. 10, Oct. 1946, pp. 608.

15. F. A. Firestone, J. Acous. Soc. Am., 17, 1946, pp. 364.

16. J. R. Frederick, Ultrasonic Engineering, (New York: Wiley and Sons, 1965).

17. D. I. Bolef and J. G. Miller, Physical Acoustics, 8, W. P. Mason, ed., (New York: Academic Press, 1971).

18. H. J. McSkin, Physical Acoustics, 1A, W. P. Mason, ed., (New York: Academic Press, 1964).

19. D. I. Bolef and J. DeKlerk, IEEE Transactions, UE-10, No. 1, July 1963.

20. R. G. Leisure, Rev. Sci. Instr., 43, No. 7, July 1972.

21. R. G. Leisure and D. I. Bolef, Rev. Sci. Instr., 39, 1968, pp. 199.

22. W. E. Moerner and J. G. Miller, IEEE Ultrasonics Symposium, Cat. # 74CHO-896-ISU, 1974.

23. J. G. Miller and D. I. Bolef, Rev. Sci. Instr., 40, 1969, pp. 362.

24. J. G. Miller, J. Acous. Soc. Am., 53, No. 3, 1973, pp. 710.

25. Virgil Stubblefield, Ph.D. Dissertation, Washington University, 1975 (unpublished).

26. D. I. Bolef, Physical Acoustics, 4A, W. P. Mason ed., (New York: Academic Press, 1966).

27. W. D. Smith, J. G. Miller, D. I. Bolef, and R. K. Sundfors, J. Appl. Phys., 40, 1969, pp. 4967.

28. E. M. Purcell, H. C. Torrey, and R. V. Pound, Phys. Rev. 69, 1946, pp. 37.

29. Dennis Dietz, Joseph S. Heyman, J. G. Miller, Richard E. Clark, Proc. of Annual Conference on Engineering in Medicine and Biology,Philadelphia, Pennsylvania, Oct. 6-10, 1974.

30. Russel H. Patterson, Jr. and Jack Kessler, Surgery, Gynocology, and Obstetrics, Sept. 1969, pp. 505.

31. H. Gobrecht and A. Bartschat, Z. Physik, 153, 1959, pp. 529.

32. H. D. Nine, Phys. Rev. Letters, 4, 1960, pp. 359.

33. Tomoya Ogawa, J. Phys. Soc. Japan, 17, 1962, pp. 400.

34. A. R. Hutson, Phys. Rev. Letters, 4, 1960, pp. 505.

35. H. D. Nine and Rohn Truell, Phys. Rev., 123, 1961, pp. 799.

36. Richard H. Bube, Photoconductivity of Solids, (New York: John Wiley and Sons, Inc., 1967, pp. 171).

37. R. G. Leisure and D. I. Bolef, Rev. Sci. Instr., 39, 1968, pp. 199.

38. W. D. Smith and R. K. Sundfors, Rev. Sci. Instr., 41, 1970, pp. 288.

39. R. H. Bube and H. E. MacDonald, Phys. Rev., 121, No. 2, 1961, pp. 473.

40. R. Truell and W. Oates, J. Acous. Soc. Am., 35, 1963, pp. 1382.

41. R. H. Parmenter, Phys. Rev., 89, No. 5, 1953, pp. 990.

42. G. Weinreich and H. G. White, Phys. Rev., 106, No. 5, 1957, pp. 1104.

43. G. Weinreich, Phys. Rev., 107, No. 1, 1957, pp. 317.

44. P. D. Southgate and H. N. Spector, J. Appl. Phys., 36, No. 12, 1965, pp. 3728.

45. H. N. Spector, Solid State Physics, 19, 1966, pp. 291.

46. J. G. Miller, Joseph S.Heyman, D. E. Yuhas, A. N. Weiss, Proc. of Am. Institute of Ultrasound in Medicine, Seattle, Wash. Oct. 1974.